UNIVERSITY OF OKLAHOMA
GRADUATE COLLEGE

SPOTTING CLUSTERS, HUNTING FOR PLANETS: A COMBINED STUDY OF GALAXY CLUSTERS IN THE X-RAY AND OPTICAL REGIME

A DISSERTATION SUBMITTED TO THE GRADUATE FACULTY

in partial fulfillment of the
requirements for the degree of

Doctor of Philosophy

July 2022

By

Saloni Bhatiani

Norman, Oklahoma

SPOTTING CLUSTERS, HUNTING FOR PLANETS: A COMBINED STUDY OF GALAXY CLUSTERS IN THE X-RAY AND OPTICAL REGIME

A DISSERTATION APPROVED FOR THE
HOMER L. DODGE DEPARTMENT OF PHYSICS AND
ASTRONOMY

BY THE COMMITTEE CONSISTING OF

Dr. Xinyu Dai, Chairperson

Dr. Constance Chapple

Dr. Chung Kao

Dr. Edward Baron

In memoriam, Dr. Rathnasree Nandivada.

Acknowledgements

As a young girl aged eleven, I would often question the vast creation and my place in it. Sometimes I would ask my father, but his answers satisfied me to no avail. It was then I discovered a book, swathed in dust, in a secluded corner of my school library. This was a book on astronomy, a book that changed my life. While my friends read the mysteries of Nancy Drew and Hardy Boys, I found my happiness in the mysteries of the universe. This was when my love affair with physics began, and here I am, 19 years thence, getting my doctorate in astrophysics. Dreams do come true!

As I tie a bow around this thesis before I gift it to the archives, my heart is filled with gratitude for the very many people that have inspired and supported the fruition of this dream. I would like to begin by expressing my sincere gratitude to my advisor Dr. Xinyu Dai for his unfaltering guidance and support over the course of my doctorate. I am deeply grateful for the faith you have maintained in my work and the patience you have shown, especially during my difficult times. Thank you for always encouraging me to look at the "big picture" and not be deterred by minor setbacks in research. I would also like to thank my collaborators — Chris Kochanek, Jenna Nugent, Eduardo Guerras, Chris Morgan, Rhiannon Griffin, Tory Sanzone, and others — for their invaluable contribution to my research. I have greatly benefitted as a researcher through their discussions and advice. I would particularly like to thank Eduardo for the time and effort he spent training me on running the microlensing simulations and for his helpful insights and discussions.

I am grateful for the opportunity to observe at the Apache pointe observatory — the best part of my Ph.D. life. Thank you to Dr. Wisniewski for the obs class and for his efforts in training me as an observer. The observing specialists at APO — Russet, Candace, Jack — thank you for making each observing night a fun-filled learning experience. I would like to acknowledge the research and financial support I have received from the NSF and NASA grants awarded to my advisor, as well as the University fellowships and grants, most importantly the prestigious Bullard dissertation completion fellowship. This thesis is based on three of my first-author publications: two of which are already published in the IOP journals (ApJ and ApJS), and one will be submitted to the Astrophysical journal (ApJ) in the near future. I want to acknowledge the American Astronomical Society and Institute of Physics Publishing for granting me the permission to reproduce my work. A special thanks to my committee members for serving on my committee and providing the necessary guidance throughout all of these years. At the start of the pandemic, I struggled, just like everyone else; it was then I found the support of Dean Randall and Dr. Sherry Irwin. I am grateful to these lovely ladies for helping me stay strong during those uncertain times.

My time in Norman has been beautiful because of the wonderful people who made this a home away from home. This includes the department of physics and all its lovely people, especially the office ladies — their bright smiles made my day, every day. It was here I built some of my best friendships: Hora, Rishabh, Delaram, Soumya, Hadi, Javad, and others. Thank you for the coffee breaks, hilarious conversations, and enjoyable game nights. A special thanks to Hora for being my officemate, confidante, and great friend. It has always amazed me how we can engage in never-ending discussions on almost any topic in the world — time sure flies by for us. It was also here that I met my roommate and my dearest friend and sister, Nazanin. I never knew I could build such a deep friendship in my life until I met you. Thank you for being there for hugs, laughs, and cries during the highs and lows of this Ph.D. At this point, a funny anecdote comes to mind, so excuse me for digressing. Once when I accidentally injured my hand, I was being rushed to the ER. On my way in the ambulance, my roommate (Nazanin) told the paramedic that I was worried I might lose my hand. The paramedic gazed at us and jokingly responded, “are you sure you are getting a Ph.D.?”. Since I was in shock, I only hazily recall laughing at the time. Later, when awareness dawned, I reflected upon that instance and learned that: with a doctorate comes a great responsibility of always acting smart — even while dying.

A question asked to my father was left unanswered many years ago; that question changed my life and set me on the path to becoming an astrophysicist. I owe this thesis to my dad for having faith in me to unravel it by myself, for being the cause to this effect, thank you daddy! This thesis would go unwritten without the love and support of the most cherished person in my life, my mother. Through the rickety slopes of this Ph.D., she has been the best resting place — my constant source of encouragement and upliftment. Thank you, ma! I would also like to thank my two pillars of strength, my sister Sukriti and my brother Param, who brought happiness and excitement to my life when Ph.D. got rough and unkind. The biggest thank you goes to my eternal cheerleaders who always stand tall and proud at every little achievement of my life — my wonderful grandparents. Life (& this Ph.D.) has been beautiful because of your unconditional love and the delectable homemade treats. While I was piled higher and deeper in my research here, friends and my extended family in India and other parts of the globe kept me strong with their love and care. Thank you to all of you back home for your constant presence, endless Facetime calls, and much-needed laughs. I would particularly like to thank my friends — Geetika, Kshitij, and Akash — for being all ears to my rants (while I was dissertating) and instilling positivity and confidence in me during the final leg of this Ph.D.

Knowing that we stand on the shoulders of giants, this vote of thanks would be incomplete without the mention of all the great people who have inspired me. Thank you to all my teachers and the remarkable scientists for paving the way for my success. I want to acknowledge the astronomical contribution of Prof. Pranjal Trivedi to my life. I wouldn't be where I am today without you, sir. A special thanks to the late Dr. Rathnasree for being an excellent mentor to me and a great inspiration for the coming generations of Indian female astrophysicists.

Lastly and most importantly, I owe the worth of my knowledge to my master, my Guru, for showing me the light, the light within.

Nasadiya Sukta

(Hymn of Creation of the Universe)

"There was neither non-existence nor existence then; Neither the realm of space, nor the sky which is beyond; What stirred? Where? In whose protection?

There was neither death nor immortality then; No distinguishing sign of night nor of day; That One breathed, windless, by its own impulse; Other than that there was nothing beyond.

Darkness there was at first, by darkness hidden; Without distinctive marks, this all was water; That which, becoming, by the void was covered; That One by force of heat came into being;

Who really knows? Who will here proclaim it? Whence was it produced? Whence is this creation? Gods came afterwards, with the creation of this universe. Who then knows whence it has arisen?

Whether God's will created it, or whether He was mute; Perhaps it formed itself, or perhaps it did not; The Supreme Brahman of the world, all pervasive and all knowing He indeed knows, if not, no one knows"

—Rigveda 10.129 (Abridged, Translatation by Kramer 1986)

Abstract

Observational studies of the distribution of galaxies in the Universe reveal inhomogeneity and structure on Mpc and larger scales. Galaxy clusters are the largest gravitationally bound structures containing a virialized congregation of galaxies; therefore, studying them is essential for understanding the constitution and assembly history of these systems and probing the large-scale structure of the Universe. The Swift AGN and Cluster survey is a serendipitous X-ray survey aimed at building a large X-ray-selected cluster catalog with $\sim$ 1000 cluster detections expected by its final release. In this thesis, I perform an optical analysis of 348 (out of 442) X-ray selected cluster candidates from the Swift cluster catalog using multi-band imaging from MDM 2.4m and the Pan-STARRS survey for the northern sky, and CTIO 4m and DES for the southern sky. I report the optical confirmation of 109 clusters with $> 3\sigma$ galaxy over-density with photometric redshift estimates extending up to $z \sim 1$. The Swift survey is nearly complete for $z \leq 0.3$ and 85% complete for $z \leq 0.5$. The undetected clusters are possibly high redshift clusters with $z > 0.8$ that warrant follow-up observations in the near-infrared. Furthermore, I also study the scaling relations between the X-ray and optical cluster mass observables and the offset distribution for all the optically verified SACS clusters and find them to be in agreement with other studies in literature.

Another facet of my dissertation involves using quasar microlensing to probe the intracluster region of a galaxy cluster. I employ this novel technique to exert effective constraints on planet-mass objects in two extragalactic systems, Q J0158-4325 and SDSS J1004+4112, by studying their induced microlensing signatures. Chandra observations for these two gravitationally-lensed quasars reveal variations of the emission line peak energy, which can be explained as microlensing of the FeKα emission region surrounding the supermassive blackhole induced by planet-mass microlenses. To corroborate this, I have performed microlensing simulations and developed an edge detection algorithm to determine the probability of caustic transiting events. Comparison with the observed rates has yielded constraints on the substellar population, with masses ranging from Lunar to Jovian mass bodies within these galaxy or cluster scale structures. These results suggest that unbound planet-mass objects are common in galaxies, and these are surmised to be either free-floating planets or primordial black holes. These are the first-ever constraints on the substellar mass distribution in the intracluster light of a galaxy cluster. This analysis yields the most stringent limit for primordial black holes at the mass range.

Table of Contents

List of Tables

List of Figures

Chapter 1

Introduction

> *"If you take a galaxy and try to make it bigger, it becomes a cluster of galaxies, not a galaxy. If you try to make it smaller than that, it seems to blow itself apart."*
>
> – *Jeremiah Ostriker*

1.1 Galaxy clusters: an overview

The vast expanse of the cosmos has been a long-standing mystery for astronomers. Observations have shown that the Universe is fairly homogeneous and isotropic at scales larger than about 100 h^{-1} Mpc, where 1 Mpc $= 3 \times 10^{22}$ m and $h \approx 0.7$ is dimensionless Hubble parameter that represents the current rate of expansion of the Universe. However, this homogeneity breaks down on smaller scales revealing the seemingly fractal nature of the cosmos. Thus, over the lifespan of the Universe, it has expanded and evolved from a homogeneous slate to an intricate mosaic of structure, as seen today in the form of galaxies, stars, planets, nebulae, etc, encased within the Large scale structure of the Universe (LSS). The LSS is a gigantic web-like structure spun over billions of light years, consisting of clusters and large filaments of galaxies, separated by voids and glued together by gravity. Galaxy clusters are the most massive gravitationally bound objects in the Universe with mass ranging from $10^{13}\ M_{\odot}$ up to $10^{15}\ M_{\odot}$, and are characterized by deep gravitational potential wells containing hundreds to thousands of galaxies spread across a few Mpc. Originating from the largest peaks in the primordial density field, induced by the quantum fluctuations in the early inflation era (e.g., Bond, Kofman & Pogosyan 1996), galaxy clusters form the knots in the cosmic web and trace the large-scale structure of the Universe.

In the early 1930s, Fritz Zwicky (Zwicky 1933) found that the virial mass of the Coma cluster, estimated using the velocity measurements of the galaxies, significantly outweighed the visible stellar mass of the cluster. This anomaly led to the serendipitous discovery of dark matter, or "Dunkle Materie" (as he coined it). The cluster mass budget is dominated by the non-emitting dark matter ($\sim$ 83-89 percent; see Voit 2005; Gonzalez et al. 2013; Dai et al. 2010) that sculpts the gravitational potential well in which galaxies and luminous X-ray gas are embedded. The remaining $\sim$ 9–13% is the baryonic content, out of which only a few percent manifests into stars and galaxies (e.g., Dai et al. 2010). The largest fraction of the baryonic component of a cluster constitutes the hot ionized plasma called the Intracluster Medium (ICM; Kravtsov & Borgani 2012; Plionis et al. 2008). The leading paradigm for structure formation and evolution predicts that clusters form later in the history of the universe and are still growing through hierarchical merging. Initially local halos are formed by the gravitational collapse of overdensities of dark matter, which further mature into more massive systems by a combination of infall and merging over cosmic timescales (e.g., Muldrew et al.

2015). This aggregation process enhances the energy of the galaxies that are bound within the gravitational well of the DM halo, stripping them of gas and raising their velocities to as high as $\sim 10^3$ km s^{-1} in the cluster core. The gravitational potential energy released by the merger shocks the ICM by adiabatically compressing and heating the gas until a state of virialization is established within the system. This increases the temperature of the gas to up to 10-100 MK, almost completely ionizing it and creating a superheated plasma that emits strong X-ray radiation. Thus, clusters of galaxies have a complementary appearance when viewed in X-ray and optical. In optical, they appear as a localized assembly of galaxies, with hundreds or thousands of galaxies closely spaced on the plane of the sky. On the other hand, in X-rays, clusters appear as single extended sources with very high luminosities ranging from $10^{10} - 10^{12}\ L_{\odot}$. In both regimes, they provide a good contrast against the surrounding field and stand out as the highest density regions. Figure 1.1 shows the Hydra galaxy cluster in both optical and X-ray light.

Galaxy clusters are integral to our understanding of the universe. Since they represent the link between the cosmological and galactic scale, they act as sensitive probes of cosmology and excellent resources for astrophysical studies. They consist of a population of coeval galaxies that do not evolve independently but via mutual interactions and interactions with their local environment. Thus, galaxy clusters are an ideal laboratory for studying the galaxy-galaxy interactions, gas-galaxy interactions, star formation activity and history, and the environmental influences that govern the formation and evolution of galaxies and clusters. They also provide unique insight into a host of complex astrophysical processes such as mergers, radiative cooling, plasma heating, AGN feedback, tidal stripping, etc. From a cosmological perspective, galaxy clusters lay the testing ground for various cosmological frameworks (e.g., Press & Schechter 1974; Majumdar & Mohr 2004; Hu 2003; Lima & Hu 2004; Lima & Hu 2005). Clusters trace the largest peaks in the distribution of matter; therefore, their abundance and spatial distribution can improve our understanding of the formation and growth of structure (e.g., Evrard 1989; Oukbir & Blanchard 1992; Bahcall 1999) by providing measurements of the amplitude of density perturbations, σ_8 parameter, and strong constraints on other cosmological parameters such as the growth factor. Since clusters are a representative sample of the global matter content of the universe, their constraints on the relative abundance of dark matter and baryonic matter provide an independent measurement of the cosmic average.

Galaxy clusters can be studied across the electromagnetic spectrum with each waveband mapping different components or processes within the cluster: i) Galaxies or the stellar component is observable at Optical/NIR wavelengths ii) X-rays trace the gas component − the hot Intracluster medium iii) Microwave or sub−mm wavelengths are sensitive to Sunyaev-Zeldovich (SZ; Carlstrom et al. 2000; Mohr et al. 2002; Pierpaoli et al. 2005) signal arising from the interaction between the Cosmic microwave background (CMB) and the ICM via inverse Compton scattering iv) Radio observations enables the study of diffuse relic radiation, radio halos, active galactic nuclei (AGN) and magnetic field activity within the cluster. Historically, most effort has been devoted to optical and X-ray searches; however, recent advances in other wavelengths, especially the SZ surveys in the sub-mm range, show promise. A multiwavelength approach is vital to piece together the different components of the cluster and gain a holistic understanding of these systems. While a multiwavelength study is ideal, this thesis investigates galaxy clusters only in the X-ray and optical wavebands and opens the door for

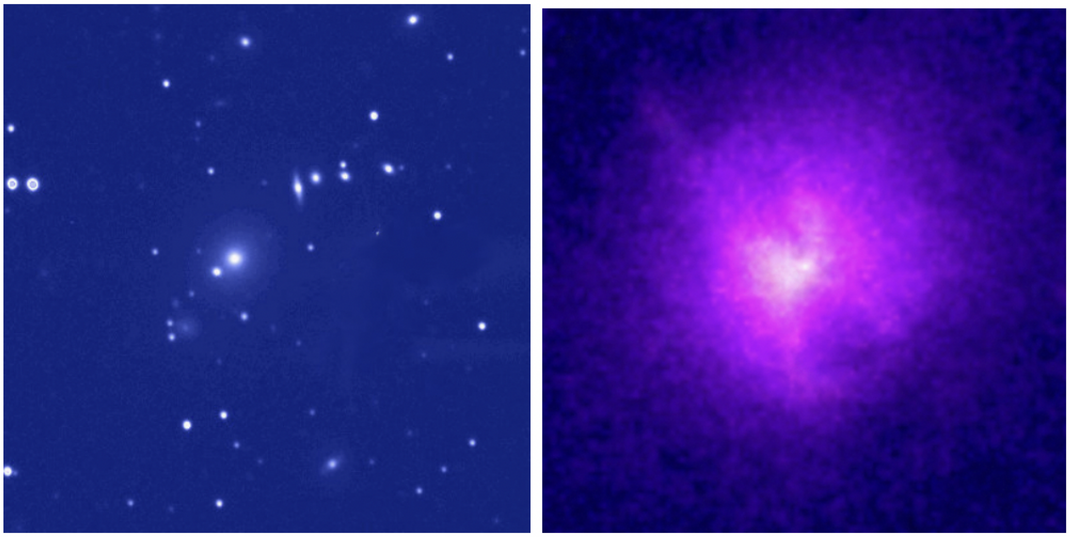

Figure 1.1 The figure shows the Hydra galaxy cluster in the visible (left) and X-ray wavelengths (right). In the left image, the cluster appears as an overdensity of galaxies with several hundred galaxies concentrated in a few Mpc at a mean redshift $z = 0.05$. The right image is a false color X-ray image for the same field obtained using the Chandra X-ray telescope. The X-ray emission from the hot intracluster medium is shown, where the color is indicative of the brightness, with white being the brightest. In the X-rays, the cluster appears as an extended object and traces the gravitational potential well within which galaxies and intracluster gas are embedded. Image courtesy of NASA/CXC/SAO.

future follow-up studies in other parts of the spectrum. In the subsequent sections, I will describe the observational methods and properties of clusters in the X-ray and optical regime.

1.2 Clusters in the optical sky

More than half a century ago, George Abell built the first catalog of galaxy clusters (Abell et al. 1958) by visually inspecting the photographic plates from the Palomar observatory sky survey (POSS). The catalogue was published as a part of his Ph.D. thesis and contained 2712 rich clusters from the Northern hemisphere. This work was later expanded to incorporate clusters from the southern hemisphere, producing an elaborate catalogue of ~ 4700 clusters (Abell, Corwin & Olowin 1989; Schuster 1980), which enabled the first statistical study of the cluster population. Abell introduced a cluster classification scheme based on the cluster richness (number of galaxies bound to the cluster), compactness (radial size $\sim 1.5\ h^{-1}\ Mpc$, called the Abell radius), distance or the redshift (estimated from the magnitude of the tenth brightest galaxy member), and the galactic latitude (to exclude the star dense regions like the galactic plane). Richness is a prime observable in the optical band that serves as a measure of the member galaxies of a cluster. The Abell classification, based on the cluster richness, ranges from Abell Class 0, which represents the poorest clusters with $30-50$ galaxies, to Abell Class 5, which comprises the most populated objects with ≥ 300 galaxy members. Abell clusters primarily belong to the local universe with nominal redshifts of $z \leq 0.2$; however, later measurements indicate that some of these clusters are even more distant, as far as $z \sim 0.4$. Thereafter, other cluster catalogues were compiled with varying selection and classification criteria (e.g., Zwicky et al. 1961; Bautz & Morgan 1970; Rood & Sastry 1971). These early cluster surveys were mostly limited to visual examination of the photographic plates to locate galaxy-overdense regions; therefore, these catalogs were prone to human bias and plagued by contamination from line-of-sight galaxies since galaxy clusters are three-dimensional objects projected onto a two-dimensional plane of the sky (e.g., Sutherland 1988; Collins et al. 1995; Biviano 2008).

With the arrival of digitized photographic plates and automated cluster identification procedures, the torch was passed from humans to machines (e.g., Dalton et al. 1992, 1994; Lumsden et al. 1992; Gal et al. 2003). While this terminates any human error, mitigation of projection contamination requires redshift information for the 3-D reconstruction of galaxies, which can be particularly expensive when obtained spectroscopically. An alternative and cheaper option involve using multi-color CCD photometry to obtain precise measurements of the galaxy color to de-project the galaxies. The prevalence of wide-field multi-band CCD imaging in recent years has prompted a surge in the volume of cluster samples and the development of new optical cluster finding algorithms. Although it is possible to estimate the photometric redshifts of galaxies using Spectral energy distribution (SED) template fitting (e.g., Casabai et al. 2003; Brammer et al. 2008) or machine learning methods (e.g., Oyaizu et al. 2007; Collister & Lahav 2004), photo-zs are susceptible to large errors and is generally unsuited for accurate de-projection of galaxies, particularly while probing fainter cluster populations. A popular cluster finding method exploits the ubiquitous red sequence feature in clusters (e.g., Bower et al. 1992; Gladders & Yee 2000), which is a tight color-magnitude relation followed by the cluster galaxies. This method forms the basis of many optical cluster finders (e.g., Goto et al. 2002; Gladders et al. 2007; Koester et al. 2007a; Hao et al. 2010; Szabo et al. 2011; Wen et al. 2012; Rykoff et al. 2014) since it largely eliminates the projection contamination and provides reliable redshift estimates. I have discussed the red sequence technique in detail in the following section. Another unique property of clusters is the presence of the brightest cluster galaxy (BCG) (e.g., Bautz & Morgan 1970; Sarazin et al. 1986), which is a massive elliptical galaxy (typically a CD galaxy) near the center of the potential well. More refined cluster finding algorithms (Koester et al. 2007a; Hao et al. 2010) are based on the identification of a red sequence feature and a central BCG, both corresponding to a local overdensity of galaxies. For example, the maxBCG algorithm (Koester et al. 2006, 2007) produced a catalog of $\sim 14,000$ optically selected clusters using the data from the Sloan Digital sky survey (SDSS;

York et al 2000). Another approach to identify clusters in large optical-IR surveys is the matched filtering technique (MF; Postman et al. 1996; Olsen et al. 1999; Lobo et al. 2000; Goto et al. 2002) that filters the survey data through a likelihood function, retrieving systems with the maximum likelihood of matching the model. These algorithms model the clusters based on the luminosity function, radial density profile, red sequence characteristics, or the presence of a central BCG. For example, assuming a model for the density profile of clusters, the algorithm identifies regions in the sky where the distribution of galaxies matches the projected cluster density profile. The algorithm also allows the use of a combination of model filters to recover the cluster signals from the various locations of these large-area galaxy surveys (e.g., Goto et al. 2002; Koester et al. 2007). Some of the widely used optical catalogs with 20000+ clusters include the GMBCG catalog (Gaussian Mixture Brightest Cluster Galaxy; Hao et al. 2010), Wen et al. 2012, SDSS redMaPPer (red-sequence matched-filter Probabilistic Percolation cluster finder; Rykoff et al. 2014) catalog.

Notwithstanding the fact that optical cluster finders suffer from projection effects and selection biases, they are well-suited for providing a large sample of clusters conducive to statistical studies. Moreover, they allow the measurements of redshifts of clusters, in addition to optical properties, such as cluster richness that shows correlation with the cluster mass. Future surveys such as the Large synoptic survey telescope (LSST; LSST Science Collaboration 2009), Euclid wide survey (Laureijs et al. 2011), Wide Field Infrared Survey Telescope (WFIRST; Spergel et al. 2015) will revolutionize our understanding of cluster evolution and cosmology with the detection of hundreds of thousands of galaxy clusters, covering a wide range of cluster masses, even down to the galaxy group scale ($\sim 10^{14} M_{\odot}$), with redshifts up to $z \sim 2$ or higher (Sartoris et al. 2016; Euclid collaboration 2019).

1.3 The red sequence method

The Red Sequence Method is based on the observational fact that the population of elliptical galaxies in a cluster follows a tight color-magnitude relation. This unique signature of the early-type galaxies in a cluster is called the Cluster Red Sequence (e.g., Bower et al. 1992; Van Dokkum et al. 1998; Gladders & Yee 2000; López-Cruz et al. 2004; Bernardi et al. 2005; DeLucia et al. 2006; Mei et al. 2008). Cessation of star formation in the cluster galaxies due to environmental stripping or other starvation processes (Balogh et al. 2000) causes the quiescent stellar population in these galaxies to develop strong metal absorption lines, which appear as a break in their spectra near 4000 Å. Since the galaxies in the cluster are coeval with a common redshift, their colors are nearly similar within the band that contains the spectral break. This characteristic color defines the distinct feature called the "red sequence" in the color-magnitude diagram. Figure 1.2 shows the red sequence feature in the color-magnitude diagram for galaxy cluster Abell 1084. Galaxies show a bimodal distribution in the color-magnitude space, such that the passively-evolving (non-star-forming) population align along the red sequence, and the star-forming field galaxies follow a rather diffuse distribution termed the Blue cloud. This bimodality has been observed in Galaxy clusters up to $z \sim 1$ (Bell et al. 2004) and can be modelled using two Gaussian Distributions (Baldry et al. 2004). The bimodality hints toward the origin of the red sequence, which can be explained by the quenching of star formation in the blue cloud followed by the merging of red gas-poor galaxies (Bell et al. 2004; Van Dokkum 2005).

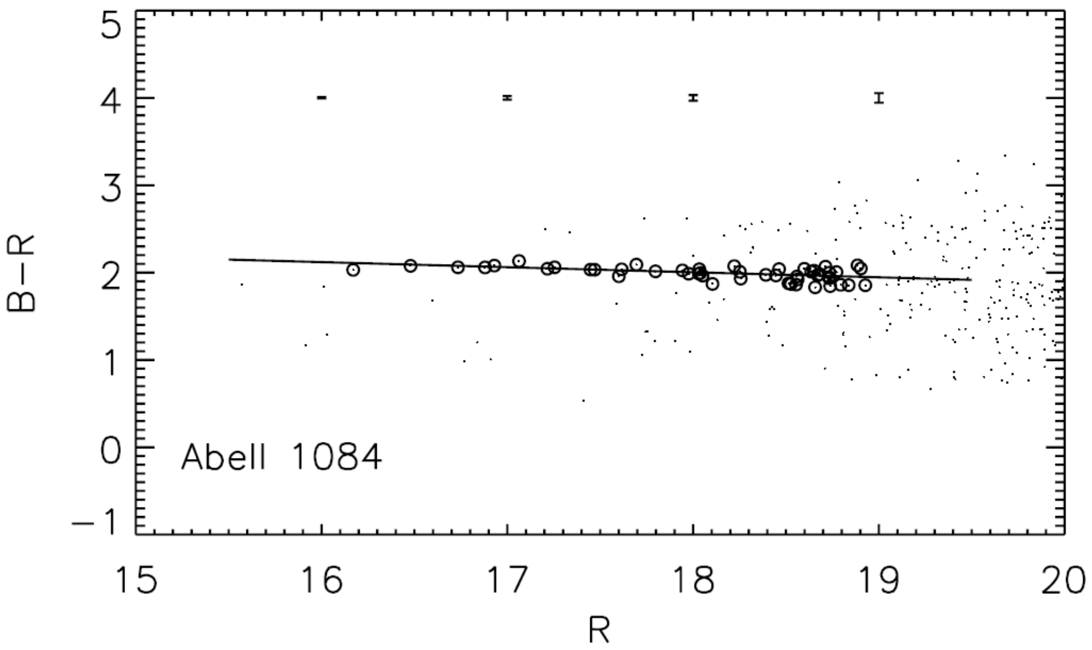

Figure 1.2 The observed color-magnitude diagram for the cluster Abell 1084 from Stott et al. (2009). The black line represents the red sequence fit for the red elliptical galaxies of the cluster. The error bars for each magnitude range are presented. The tiny black dots are the contaminating galaxies in the field that are not part of the red sequence.

There are several factors that make the red sequence method an efficient and powerful method of detection. Firstly, the red sequence galaxies contain a homogeneously old and red stellar population. This observation complies with the concordance model that assumes that structure in the present universe is formed by hierarchical clustering of the initial overdensities. Hence, the elliptical galaxies of clusters can serve as reliable markers of clustering (Gladders & Yee 2000). Secondly, the elliptical galaxies constitute the brightest galaxies in a cluster; hence they are the most easily observed galaxies in a flux-limited survey (Sandage et al. 1985; Barger et al. 1988). Moreover, the radial distribution of the early-type galaxies in a regular cluster is more compact in comparison to other morphological types (Dressler et al. 1997), thereby providing significant contrast against the background. Thirdly and most importantly, cluster elliptical galaxies constitute the oldest stellar population in the universe; thus, they appear redder than the other galaxies at the same redshift and even lower redshifts. Consequently, the red sequence method does not suffer significantly from the foreground and background contamination at higher redshifts. Another important factor in favor of this method is that the red sequence color acts as an effective redshift indicator (Smail 1998; López-Cruz et al. 2004). This 4000 Å break moves redward across filters with increasing redshifts, thus imposing limitations on the detection method at higher redshifts. In optical photometry, $g - r$ is the ideal color for detecting clusters at low redshifts, $r - i$ band is used for detecting clusters at intermediate redshifts, while $i - z$ is used at higher redshifts. For clusters at $z > 1$, the red sequence feature slides into the infrared territory and can be detected using NIR photometry. A slew of optical observations has established the existence of the red sequence out to $z \sim 1$ (Ellis et al. 1997; Kodama et al. 1998; Van Dokkum et al. 1998; Bell et al. 2004; Stanford et al. 2006; Tanaka et al. 2007; Mei et al.

2009). Infrared observational campaigns like the Spitzer Adaptation of the red sequence cluster survey (SpARCS, Wilson et al. 2009) have expanded the red sequence searches past the optical and NIR regime. Kodama et al. (2007),Zirm et al. (2008), Doherty et al. (2010), Papovich et al. (2010) have extended the CMR cluster studies up to redshifts of 3. For redshifts as high as $2 < z < 4$, the cluster red sequence represents the protoclusters which are believed to be the predecessors of galaxy clusters that eventually virialize at redshifts of 1. Thus, the detection of distant clusters is integral to our understanding of the formation and evolution of structure in the universe. In this thesis, I have extensively used the red sequence method to optically identify the red sequence feature in SACS X-ray selected clusters out to redshifts of $z \sim 0.9$.

1.4 X-ray view of Clusters

Early detection of X-rays in galaxy clusters was made in Virgo and Coma clusters using airborne telescopes (e.g., Byram et al. 1966; Meekins et al. 1971). However, a major leap in the X-ray studies of clusters occurred with the launch of the Uhuru X-ray satellite, which conducted the first large-scale X-ray survey of the sky, producing the Uhuru catalog (Giacconi et al. 1972, 1974; Forman et al. 1978a). During the first year of its operation, it performed prolonged observations of known X-ray sources such as Virgo and Coma Clusters which uncovered some salient properties of these sources. It was established that Galaxy clusters are one of the brightest extragalactic objects in the sky with luminosities $\sim 10^{43-45}$ ergs. It was also found that X-ray emission was diffuse and extended, spread over $200-3000$ kpc, and most likely not associated with an individual galaxy (Kellogg et al. 1972). Early all-sky surveys such as HEAO-I and ARIEL V (Piccinotti et al. 1982;

Kowalski et al. 1984) were restricted to the detection of mostly luminous X-ray clusters. Deeper observations with Einstein and EXOSAT (e.g., Gioia et al. 1990b; Edge et al. 1990) extended the sample of higher redshift clusters (out to $z \sim 0.6$), leading the way for studies of the cosmological evolution of clusters (Henry et al. 1992). With the development of more sensitive X-ray instruments, lower mass and lower luminosity clusters were also identified. The ROSAT All-Sky Survey (RASS, Trümper 1993) was the first X-ray survey to image the entire sky facilitated a slew of large-scale X-ray cluster surveys and the discovery of hundreds of clusters (e.g., Ebeling et al. 1997, 1998, 2000, 2001; Burns et al. 1996; Crawford et al. 1995; Ledlow et al. 1997, De Grandi et al. 1999; Böhringer et al. 2000, 2001, Cruddace et al. 2002). The ROSAT-ESO Flux Limited X-ray (REFLEX) survey (Böhringer et al. 2001) produced a large homogeneously selected sample of clusters covering a broad range of luminosities, 10^{42-45} ergs, comprising of small galaxy groups to high mass clusters out to redshift $z \sim 0.5$. Furthermore, another catalog based on RASS is the Meta-Catalog (MCXC; Piffaretti et al. 2011), which is a compilation of several RASS-based catalogues (NORAS, REFLEX, BCS, SGP, NEP, MACS, and CIZA) and serendipitous (160SD, 400SD, SHARC, WARPS, and EMSS) survey catalogues. The newer generation of X-ray satellites such as Chandra, XMM-Newton, and Suzaku have provided more accurate measurements of cluster properties for existing catalogs (mentioned above) as well as new cluster samples, spanning a wide range of masses with redshifts extending up to $z \sim 1.5$ (e.g., Kolouridis et al. 2021), therefore enabling cosmological studies (e.g., Vikhlinin et al. 2009; Mantz et al. 2010) and accurate characterization of the physical properties of clusters (Pratt et al. 2010; Arnaud et al. 2010; Pierre et al. 2007; Clerc et al. 2014).

The X-ray emission from the galaxy cluster traces the hot gas that permeates the intergalactic region of the cluster called the Intracluster medium (ICM). The energetic plasma in the ICM chiefly comprises ionized Hydrogen and Helium that originate in the early Universe during baryogenesis and some heavier elements that formed in the interior of stars at various stages of stellar evolution. The metallicity or the abundance of heavy elements (heavier than helium) in clusters is typically about one-third ($\sim 0.3\ Z_{\odot}$) of the value of the Sun. The principal emission mechanism of the ICM is thermal Bremsstrahlung or free-free emission. The ICM gas is a superheated ionized plasma with temperature $\sim 10^8$ K with typical atomic density of $n \sim 10^{-4}$ cm^{-3} (Kravstov & Borgani 2012). Taking into account the high temperature and low-density conditions of the ICM, theoretical models predict that the ICM is almost fully ionized and that the electrons and nuclei are in a state of thermal equilibrium. When an accelerated electron passes close to the potential well of ICM nuclei, the electron undergoes deceleration and loses kinetic energy, which is released in the form of X-ray radiation. The equation for Thermal Bremmstrahlung is given as follows.

$$\epsilon_{ff} \propto Z^2 n_e n_i g_{ff} {T_g}^{-1/2} e^{-h\nu/kT_g} \tag{1.1}$$

Where ϵ_{ff} is the associated emissivity or the amount of energy emitted due to thermal Bremsstrahlung per unit time, frequency, and volume, and T_g is the temperature of the gas. The emissivity is proportional to the number density of electrons n_e and the number density of ions n_i of charge Z. Here, g_{ff} is the free-free gaunt factor that corrects for quantum mechanical effects. X-ray observations allow measurements of the physical properties of the cluster, such as temperature, density, and metallicity. Under the assumption that clusters are virialized and in a state of hydrostatic equilibrium, the cluster mass distribution can be determined from the temperature and density profiles of the ICM.

There are several advantages of the X-ray detection method. Firstly, the X-ray emission is proportional to the squared density of the ICM, which provides high contrast against the background (e.g., Voit 2005); therefore, X-ray surveys are robust against projection effects in comparison to optically selected surveys. Secondly, for a flux-limited X-ray survey, the detected cluster sample can be easily modelled by a well-understood selection function. Lastly, the X-ray observables are tightly correlated to the mass of the cluster as compared to the optical properties; therefore, cluster mass can be estimated using luminosity or temperature measurements. Nonetheless, the X-ray detection method also has some shortcomings. One particular one is its predisposition to selection effects, such that it favors mostly bright and massive clusters (e.g., Ebeling et al. 1998); therefore, alternate detection methods are required to select clusters with lower mass, high redshift, or unresolved gas components. In addition, a cool-core bias in the X-ray selection process favors the detection of "cool-core" clusters over "non-cool-core" clusters (e.g., Eckert et al. 2010). Another disadvantage is that X-ray surveys do not allow the estimation of the redshifts of the clusters; therefore, X-ray surveys are often accompanied by optical or spectroscopic follow-up to determine the redshifts. Moreover, the detectability of high redshift clusters for shallower X-ray surveys gets compromised due to the $(1+z)^{-4}$ dependence of the surface brightness of X-ray emission. The one major disadvantage of X-ray detection is the expense of observations. Since X-ray observatories are space-based, X-ray surveys can be big-budget. Therefore a combination of X-ray and optical programmes is well-suited for cluster studies. In my thesis, I have performed an optical follow-up of the X-ray-selected clusters from the Swift AGN and cluster survey (discussed in detail in the following section). Because of the above advantages, the X-ray selection method was used, which was followed up with optical observations to determine the redshifts and the richness of the galaxy cluster.

1.5 Swift AGN and Cluster survey (SACS)

The Swift AGN and Cluster survey is a serendipitous survey of X-ray sources in the vicinity of Gamma-ray bursts (GRB) locations in the Swift XRT fields. It is a wide-field survey spanning an area of 125 square degrees in the sky with a medium depth corresponding to a flux limit of 4×10^{15} ergs $\mathrm{cm}^2\mathrm{s}^{-1}$. The depth and area of the survey are halfway between shallow, wide-area ROSAT surveys (RASS, Voges et al. 1999) and deep, narrow-area Chandra/XMM-Newton surveys (Brandt et al. 2001; Xue et al. 2011; Pierre et al. 2004). The Swift X-ray telescope (Burrows et al. 2000 & Hill et al. 2000) has a large field of view of 23.6×23.6 arcmin^2 and operates in the energy range of $0.2-10$ keV. The wide-field surveys like the ROSAT Brightest Cluster survey Sample (BCS, Ebeling et al. 2000) and the ROSAT-ESO Flux Limited X-ray survey (REFLEX, Böhringer et al. 2004) are sensitive to low redshift clusters, while the deep field surveys are devised to probe high redshifts where clusters are a rarity; therefore better representation at intermediate redshifts is needed to fill the gap in our understanding of the evolution of galaxy cluster over cosmic time. A similar breach is observed in the detectability of AGNs at moderate luminosities and redshifts with the existing X-ray surveys. Therefore, the medium depth of the serendipitous fields coupled with the wide coverage of the survey makes it ideally suited for probing cluster and AGN populations at intermediate redshifts. Other medium-depth wide-field serendipitous surveys include: RIXOS (Castander et al. 1995), RDCS (Rosati et

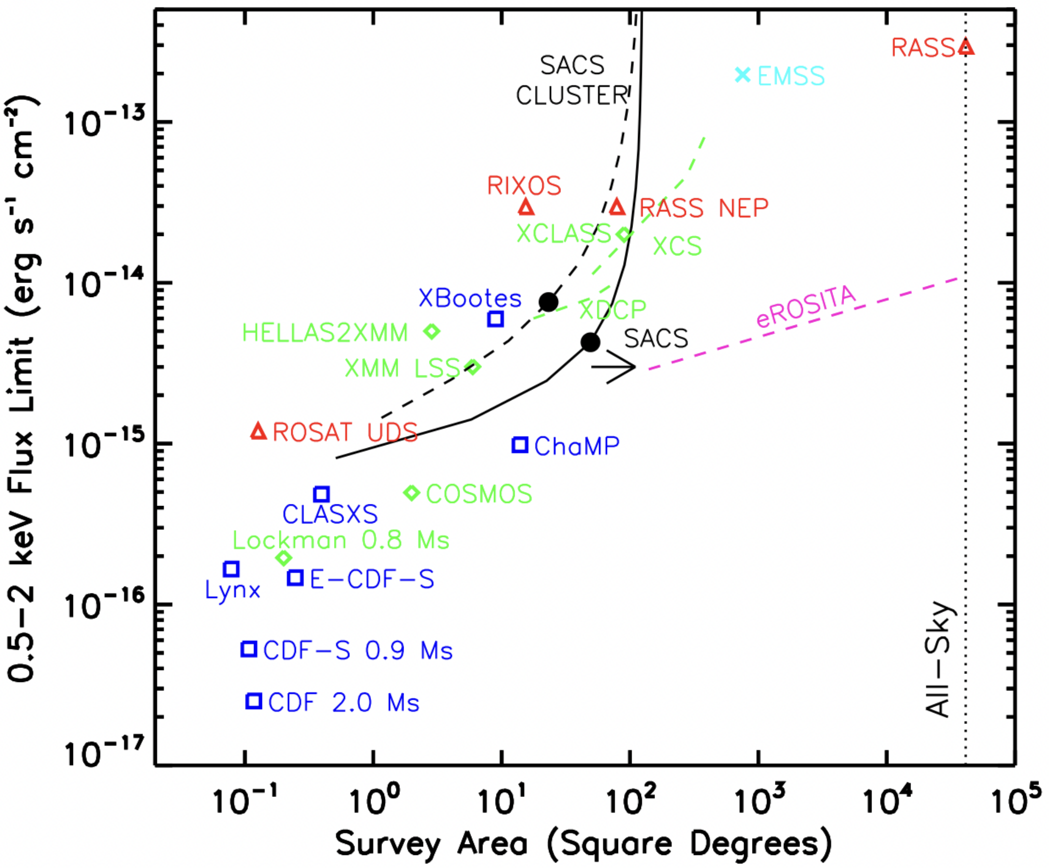

Figure 1.3 This figure from Dai et al. (2015) shows the comparison of the flux limit and survey area for various soft X-ray surveys. The Swift AGN and cluster survey (SACS) is marked in black (solid and dashed lines represent point and extended sources, respectively). It is evident that SACS has a wider coverage and deeper flux limits than other similar surveys. These soft X-ray surveys include surveys from Brandt & Hasinger (2005), medium depth XMM-Newton and Chandra surveys, and the deeper eRosita survey. The black arrow indicates that SACS will likely approach the flux limits of eRosita deep fields with the collection of more data in the future.

al. 1995; 1998), SHARC (Collins et al. 1997; Burke et al. 1997), WARPS (Scharf et al. 1997; Jones et al. 1998; Perlman et al. 2002), ROXS (Donahue et al. 2001), BMW (Campana et al. 1999), XMM-Newton and Chandra serendipitous surveys (Watson et al. 2009; Lloyd-Davies et al. 2011; Fassbender et al. 2011; Clerc et al. 2012). Since these serendipitous surveys are based on archival pointing data that was previously obtained for other purposes, a major challenge lies in modeling the selection effects without an accurate understanding of the underlying science. SACS XRT fields are centered at randomly distributed GRB locations in the sky, and since GRBs bear no semblance with other X-ray source populations, SACS acts as an excellent X-ray serendipitous survey. Figure 1.3 shows the comparison of SACS with other soft X-ray surveys.

1.6 The Gravitational lensing effect

Gravitational lensing is a phenomenon in which the light originating from a distant light source bends in the gravitational field of a massive intervening object (such as a galaxy cluster) on its way to the observer. This is one of the major predictions of Einstein's General theory of relativity. In 1915, Einstein made a calculation for the deflection of the light by the Sun's gravitational field and found it to be ~ 1.68 arcsec. He later encouraged astronomers to test the deflection observationally. In 1919, Sir Arthur Eddington led an expedition to test the general theory of relativity, where he successfully measured the deflection of the background star on the Sun's limb during a solar eclipse event and found his measurements to be consistent with Einstein's predictions (~ 1.6 arcseconds). Although Einstein had conceived the idea of the possibility of geometric gravitational lens three years before his breakthrough publication on general relativity in 1915, he deemed such a phenomenon to be unobservable from the earth. Later in 1936, upon the insistence of a colleague, he published an article in the journal Science about the formulation of a gravitational lens and the multiple images observable by starlight. This stirred curiosity in the astronomy community and was followed by a suite of articles that helped build the theory further. The complete theory of gravitational lensing of transparent lenses was developed in the 1970s (Bourassa & Kantowski 1975; Cooke & Kantowski 1975). It was only in 1979 that this effect was validated observationally with the detection of the first gravitational lens Twin Q 0957+561 (Walsh et al. 1979). At present, hundreds of such systems have been identified, and gravitational lensing has risen to the forefront of major astrophysical research in the world.

Below I briefly review the basic theoretical formalism for gravitational lensing based on the works of Schneider et al. (1992), Refsdal (1964b), Kneib & Natarajan 2011, and Narayan & Bartelmann (1996). A diagram of a typical gravitational lens system is shown in Fig 1.4. The figure shows the geometric arrangement of a lens system in which the source (S) lies at a distance D_S with respect to the observer (O), the massive lens (L) is at a distance D_L from the observer, and D_{LS} from the source. The light emanating from the source undergoes deflection by an angle α when it encounters the gravitational potential of the intervening lens before reaching the observer. β denotes the angle between the lens and the source, while θ is the angle between the lens and the image or the apparent position of the source. Here ξ is the 2D projected position of the lens in the source plane, and v is the 2D projected position of the image in the source plane. ξ signifies the perpendicular distance of the light ray in the lens place. The distances between the source and the lens are assumed to be much larger than the dimensions of the source or the lens. The thin lens approximation supposes that the deflector mass

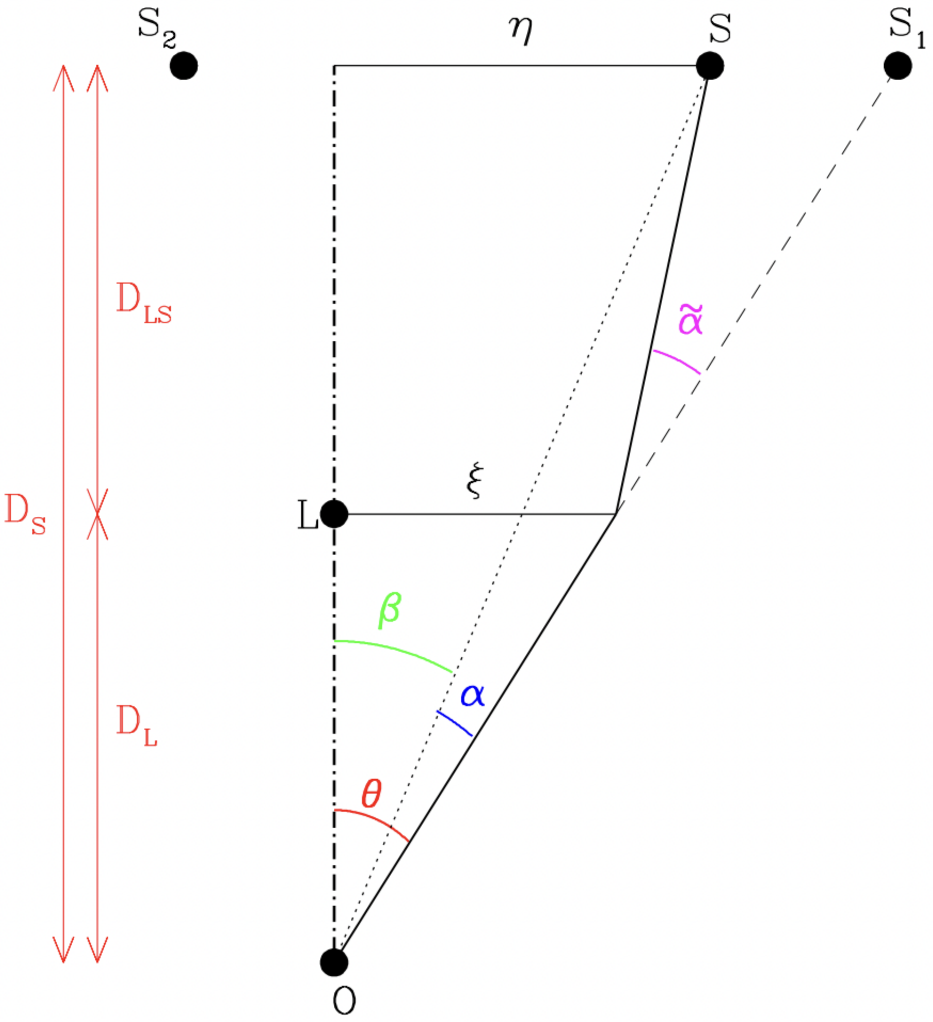

Figure 1.4 Typical geometric arrangement of a gravitational lens system is shown. The angular position of the source (S) is denoted as β, that of image (I) is θ, and the $\tilde{\alpha}$ represents the deflection angle. The quantities D_S, D_S, and D_{LS} represent the angular diameter distances between the observer and the source, the observer and the lens, the lens and the source, respectively. This diagram is borrowed from Wambsgauss (2001).

has a small expanse along the line of sight, $L << D_L$ and $L << D_{LS}$, such that the mass distribution of the lens can be assumed to be projected on a two-dimensional plane (lens plane) orthogonal to the line of sight. Because the distances involved are very large, the corresponding angles are small. Using a geometric approach under these conditions, it can be deduced:

$$\vec{\theta}\ D_S = \vec{\beta}\ D_S + \vec{\tilde{\alpha}}\ D_{LS} \tag{1.2}$$

Here, $\tilde{\alpha}$ is the total deflection angle due to all the mass elements in the lens plane and a function of the impact parameter $\vec{\xi}$. Since $\vec{\xi} = D_L\vec{\theta}$, the above expression can be written in terms of $\vec{\theta}$:

$$\vec{\beta} = \vec{\theta} - \frac{D_{LS}}{D_S}\ \vec{\tilde{\alpha}}(\theta) \tag{1.3}$$

Defining scaled deflection angle as

$$\vec{\alpha}(\theta) = \frac{D_{LS}}{D_S}\ \vec{\tilde{\alpha}}(\theta) \tag{1.4}$$

Upon inserting $\vec{\alpha}(\theta)$ in equation 1.4, a simplified equation is obtained.

$$\vec{\beta} = \vec{\theta} - \vec{\alpha}(\theta) \tag{1.5}$$

The above relation forms the basis of gravitational lensing and is called the Lens equation. It maps the observed position of the source or the image (described by $\vec{\theta}$) to its actual position (described by $\vec{\beta}$). Depending on the case, this equation can have multiple solutions, and the number of solutions determines the number of images of the background source that can be formed in the lens plane.

For a continuous mass distribution, the net deflection consists of contributions from all the mass elements of mass $dm = \Sigma(\xi) d^2\xi$ within the lens plane, where ξ is the impact vector and $\Sigma(\xi)$ is the surface mass density of the lens. Considering an integration over all individual mass components and $\xi = D_L\theta$, the scaled deflection angle can be written as:

$$\alpha(\theta) = \frac{1}{\pi} \int d^2\ \theta'\ \kappa(\theta')\ \frac{\theta - \theta'}{|\theta - \theta'|^2} \tag{1.6}$$

where

$$\kappa(\theta) = \frac{\Sigma(\theta)}{\Sigma_c} \tag{1.7}$$

$\kappa(\theta)$ is the dimensionless surface mass density, also called the convergence. For a circularly symmetric lens, the minimum surface density required to create multiple images in the lens plane is called the critical density and it is defined as:

$$\Sigma_c = \frac{c^2 D_S}{4\pi G D_L D_{LS}} \tag{1.8}$$

The lens equation (equation 1.5) allows reverse mapping of the observed image positions to the actual position of the source. For small deflections, lens mapping can be conveniently described by first-order approximation of the lens equation, mathematically expressed as a Jacobian matrix A:

$$A = \frac{\partial \vec{\beta}}{\partial \vec{\theta}} = \left(\delta_{ij} - \frac{\partial \alpha_i(\vec{\theta})}{\partial \theta_j} \right) \tag{1.9}$$

Since the deflection angle is a gradient of a bi-dimensional lensing potential, the light rays that pass the gravitational lens are deflected in a discontiguous manner, which causes the lensed image to be deformed. The Jacobian matrix, also called the magnification matrix, carries information about distortions in the shape of the image. As a consequence of Liouville's theorem, the surface brightness is conserved in the case of gravitational lensing; therefore increase in the apparent size of the background source is accompanied by an increase in the flux density of the image. The magnification of the image is the ratio of the lensed and unlensed flux density of the source. The magnification μ is defined as:

$$\mu = \frac{1}{det(A)} = \frac{1}{[\ (1-\kappa)^2 - \gamma^2\ ]} \tag{1.10}$$

Here κ refers to the physical convergence or the isotropic deformation of the source. With a non-zero convergence, a circularly symmetric source will transform into another circle with a larger radius. While γ is the Shear parameter that accounts for the anisotropic distortion in the image. For a non-zero shear, a circular source will appear stretched or squashed along a particular direction, essentially transform into an ellipse.

Critical curves are curves in the lens plane (spanned by θ) where the $detA = 0$. In the source plane (spanned by β), the analogous curves are called caustics. Since magnification μ is the inverse of the det A, we can understand them in the context of magnification. These curves represent the position(s) of the source in θ or β space for which the solution of the lens equation results in infinite magnification. In Chapter 2, I will discuss about magnification maps which comprise of networks of these caustic curves, where the magnification of the image is governed by the location of the source on the map.

1.7 Lensing Regimes

There are three categories of gravitational lensing depending on the relative position and velocity of the source, lens, and the observer. I describe each lensing regime below.

1.7.1 Strong lensing

The focusing power or the strength of the gravitational lens is determined by the convergence κ. When $\kappa \geq 1$ such that $\Sigma \geq \Sigma_c$ for a certain region of the lens, the lens comes into focus and is able to produce multiple images. Strong lensing occurs in a scenario when the background source, the lens, and the observer are nearly aligned such that the observer's line of sight is positioned within the high magnification region of the caustic envelope. Typically, strong lensing is observed when a galaxy or galaxy cluster lens is paired with a background quasar or galaxy. Due to the small relative velocities of the lens galaxies with respect to the source, strong lensing is considered a static effect in human time scales. Visually, strong lensing manifests in the form of Einstein rings, arcs, or multiple images of the background source.

While galaxy-galaxy lensing is the most commonly observed form of strong lensing, lensed quasar systems have more astrophysical applications due to the high luminosity of quasars. Strong lensing is an important tool to directly measure the total mass distribution of lensed galaxies and galaxy clusters. Strong lensing has been used to detect and derive mass measurements of galaxy clusters (e.g., Richard et al. 2010, Kawamata et al. 2016, Oguri et al. 2012, Hennawi et al. 2008). Since lensing is only sensitive to the total projected mass distribution, it is neither dependent on the dynamical state nor the baryonic properties of the cluster. Light curves analysis of lensed quasars images has been performed to measure the time-delays between the images, which is an independent method to constrain the value of Hubble parameter H_0 (e.g., Refsdal et al. 1964a, Suyu et al. 2010, 2016). The anomalies in flux ratios of quasar images are studied to probe the dark matter substructure in lensing galaxies (e.g., Dalal & Kochanek 2002). Furthermore, some studies use the angular size-redshift relation to constrain the geometric cosmological parameters Ω_m and Ω_Λ.

1.7.2 Weak Lensing

Weak lensing occurs when the observer's line of sight lies outside the caustic envelope such that $\kappa \ll 1$ or surface mass density $\Sigma \ll \Sigma_c$ at all points on the lens. In this regime, multiple images are not generated, but images of the background sources appear distorted and magnified (affected by the κ and γ produced by the lens at the image location). Weak lensing visually manifests in the form of small distortions in the shapes of images of the background galaxies. Unlike strong lensing, where images are sheared enough to form arcs, in weak lensing, the shear in the images is as low as a few percent.

To quantify the effects of weak lensing and determine the properties of the lens, it is important to have an accurate knowledge of the intrinsic shape of the background sources. Since galaxies are not circular in shape and have some inherent ellipticity, it is difficult to extract the contribution due to the gravitational lensing shear. To work around this problem, measurements of many background galaxies can be statistically averaged to estimate the shear contribution while assuming that the distribution of these galaxies is entirely random. Weak lensing has been successfully used to obtain the mass estimates of galaxy clusters (e.g., Okabe et al. 2010, Umetsu et al. 2014, Appelate et al. 2014, Kettula et al. 2015). However, lensing studies can only measure the two-dimensional projected mass that is further deprojected using an appropriate mass density model, resulting in a large intrinsic scatter in mass measurements (Becker & Kravstoc 2011; Von der Linden et al. 2014). More weak lensing studies are warranted to better constrain the intrinsic scatter in the mass reconstructions. Furthermore, weak lensing is emerging as one of the most promising probes of cosmology and the dark side of the Universe (See Bartelmann & Schneider 2001).

1.7.3 Microlensing

Strong lensing is also referred to as "macrolensing" because the separation between the images is of the order of a few arcseconds, which is resolvable by the current observational resources. However, microlensing, in principle, is a form of strong lensing where the image separation is small (milli, micro, or nano-arcseconds) and unresolvable. In the case of microlensing, the relative velocities between the source, observer, and the microlens are large, making this a dynamical effect in human timescales. Since image separation is unresolvable, this effect becomes visually apparent in the form of brightness fluctuations in the images. These microlensing-induced intensity variations are governed by the net magnification μ and the relative velocities of the source and the lens.

The lensing objects in this regime are typically compact objects such as planets or stars. One type of microlensing occurs on the galactic scale where the source and the lens both lie within the Milky Way galaxy. In this case, a foreground star becomes aligned with a background star and the observer, causing the source to appear magnified. Owing to the dynamics of the galaxy and the distances involved, the frequency of these microlensing events is of the order of hours to weeks for an observer looking towards the galactic bulge. Monitoring campaigns targeting the bulge of the Milky way, such as OGLE (Udalski et al. 2003) or MOA (Bond et al. 2001), have recorded nearly 500 such microlensing events per year. A major application of galactic microlensing is the detection of exoplanets (e.g., Gould & Leob 1992; Wambsganss 1997). When a stellar lens is accompanied by a bound planet or a companion star, microlensing due to the planet produces a distinct blip in the microlensing light curve, which can be used to constrain the mass and the separation of these systems. Moreover, surveys such as the EROS (Tisserand et al. 2007) and MACHO (Alcock et al. 2000) have transcended the Milky way and monitored the microlensing activity of stars in galaxies of the local group. These projects have provided constraints on the number and distribution of MACHOs in the Milky Way galaxy and disproven the hypothesis that MACHOs can explain Dark matter. Another form of microlensing occurs on cosmological scales, where the background source is typically a quasar, and the microlens is a cosmologically distant compact object. In my thesis, I have worked on quasar microlensing induced by stars and planet-mass objects. Please refer to Chapter 2 for a detailed discussion on this topic.

1.8 Thesis outline

This thesis is aimed at developing a multifaceted understanding of galaxy clusters. A part of this thesis involves optically confirming the detection of X-ray-selected galaxy clusters from the Swift AGN and cluster survey and studying the observable properties of the detected clusters. The other half uses a novel technique based on quasar microlensing to constrain the mass fraction of unbound planet-mass objects in a galaxy and a galaxy cluster lens. Throughout this thesis, I have adopted a standard $\Lambda-$CDM cosmology with $\Omega_m = 0.3$, $\Omega_\Lambda = 0.7$ and $h = 0.7$.

Chapter 2 describes quasar microlensing and its application in probing the granular mass distribution of the lensing galaxies and galaxy clusters. A decade-long X-ray monitoring of several lensed quasars shows microlensing signatures in the FeKα line of the X-ray spectrum of the lensed quasars. This chapter presents the microlensing analysis of two such lensed quasar systems Q J0158 $-$ 4325 and SDSS J1004 + 4112, which includes the modeling framework, microlensing simulations, and comparisons with the observations which render constraints on the mass fractions of sub-stellar objects in the foreground lens.

Chapter 3 discusses the cluster finding method used to confirm the optical detection of 55 X-ray selected Swift clusters using the data from Pan-STARRS and MDM-2.4m. It also provides the details of the data acquisition, reduction, and calibration procedures, along with the photo$-z$ estimation of the detected clusters. Additionally, it explains the measurements of the optical richness and X-ray bolometric luminosities of all the optically confirmed clusters and the comparison between the X-ray and optical observables.

Chapter 4 details the cluster identification strategy and analysis of 65 Swift clusters in the southern hemisphere using the optical data from the Dark energy survey and independent observations with CTIO/DECam. The measurements of X-ray and optical observables for all the confirmed SACS clusters and their scaling relations are also discussed.

Chapter 5 summarises the main conclusions of my thesis. It also lays out a brief road map for these projects.

References

Abell, G. O. 1958, ApJS, 3, 211

Abell, G. O., Corwin, H. G., Jr., & Olowin, R. P. 1989, ApJS, 70, 1

Alcock, C., et al. 2000, ApJ, 499, L9

Bahcall N. A., 1999, in Dekel A., Ostriker J. P., eds, Formation of Structure in the Universe. p. 135

Balogh M. L., Navarro J. F., Morris S. L., 2000, ApJ, 540, 113

Bautz L. P., Morgan W. W., 1970, ApJ, 162, L149

Baldry I. K., Balogh M. L., Bower R., Glazebrook K., Nichol R. C., 2004, in Allen R. E., Nanopoulos D. V., Pope C. N., eds, American Institute of Physics Conference Series Vol. 743, The New Cosmology: Conference on Strings and Cosmology. pp 106–119

Bartelmann, M., 2001, A&A in press; preprint astro-ph/0009394

Becker, M. R., & Kravtsov, A. V. 2011, ApJ, 740, 25

Barger A.J., Cowie L.L., Sanders D.B., Fulton E., Taniguchi Y., Sato Y., Kawara K., Okuda H., 1998, Nature, 394, 248

Biviano, A. 2008, ArXiv e-prints arXiv:0811.3535

Bell, E. F., Wolf, C., Meisenheimer, K., et al. 2004, ApJ, 608, 752

Bernardi M., Sheth R. K., Nichol R. C., Schneider D. P., Brinkmann J., 2005, AJ, 129, 61

Bond J. R., Kofman L., Pogosyan D., 1996, Nature, 380, 603

Bower R. G., Lucey J. R., Ellis R. S., 1992, MNRAS, 254, 601

Bourassa, R. R., & Kantowski, R. 1975, ApJ, 195, 13

Brammer, G. B., van Dokkum, P. G., & Coppi, P. 2008, ApJ, 686, 1503

Carlstrom, J. E., Joy, M. K., Grego, L., Holder, G. P., Holzapfel, W. L., Mohr, J. J., Patel, S., & Reese, E. D. 2000, Physica Scripta Volume T, 85, 148

Csabai I., Budavari T., Connolly A. J., Szalay A. S., Gy ´ ory Z., ˝ Ben´ıtez N., Annis J., Brinkmann, J. et al., 2003, AJ, 125, 580 Dalton G. B., Efstathiou G., Maddox S. J., Sutherland W. J., 1992, ApJ, 390, L1

Cooke J. H., Kantowski R., 1975, ApJ, 195, L11

Collins C.A. et al., 1995, in Maddox S.J., Aragon-Salamanca A., eds, Wide field spectroscopy and the distant universe: The 35th Herstmonceux Conference. World Scientific, Cambrigde, United Kingdom, p. 213

Collister A. A., Lahav O., 2004, PASP, 116, 345

Dai, X., Kochanek, C. S., Chartas, G., et al. 2010, ApJ, 709, 278

Dalton G. B., Efstathiou G., Maddox S. J., Sutherland W. J., 1992, ApJ, 390, L1

Dalton, G. B., Efstathiou, G., Maddox, S. J., & Sutherland , W. J. 1994, MNRAS, 269, 151

De Lucia, G., et al. 2007, MNRAS, 374, 809

Doherty M., Tanaka M., De Breuck C., Ly C., Kodama T., Kurk J., Seymour N., Vernet, J. et al., 2010, A&A, 509, A83+

Dressler, A. and Gunn, J. E. 1992, ApJS, 78, 1

Ellis, R. S., Smail, I., Dressler, A., Couch, W. J., Oemler, A., Jr., Butcher, H., & Sharples, R. M. 1997, ApJ, 483, 582

Evrard A. E., 1989, ApJ, 341, L71

Hao, J., McKay, T. A., Koester, B. P., et al. 2010, ApJS, 191, 254

Hu, W. 2003, PhRvD, 67, 081304

Euclid Collaboration et al., 2019, A&A, 627, A23

Gal, R. R., de Carvalho, R. R., Lopes, P. A. A., et al. 2003, AJ, 125, 2064

Gonzalez, A.H., Stanford, S.A., Brodwin, M. et al. 2012, ApJ, 753, 163

Goto T., Sekiguchi M., Nichol R. C., Bahcall N. A., Kim R. S. J., Annis J., Ivezic´ Z., Brinkmann, J. et al., 2002, AJ, 123, 1807

Gladders M. D., Yee H. K. C., 2000, AJ, 120, 2148 —, 2005, ApJS, 157, 1

Gladders, M. D., Yee, H. K. C., Majumdar, S., Barrientos, L. F., Hoekstra, H., Hall, P. B., & Infante, L. 2007, ApJ, 655, 128

Koester, B. P., McKay, T. A., Annis, J., et al. 2007, ApJ, 660, 221

Koester, B. P., et al. 2007, ApJ, 660, 239

Koester, B. P., et al. 2007a, ApJ, 660, 239

Kravtsov, A. V. & Borgani, S. 2012, ARA&A, 50, 353

Kodama, T., Arimoto, N., Barger, A. J., & Arag'on-Salamanca, A. 1998, A&A, 334, 99

Kodama T., Tanaka I., Kajisawa M., Kurk J., Venemans B., De Breuck C., Vernet J., Lidman C., 2007, MNRAS, 377, 1717

Oyaizu H. Lima M. Cunha C. E. Lin H. Frieman J. Sheldon E. S. , 2008a, ApJ, 674, 76

Oukbir, J. & Blanchard, A. 1992, A&A, 262, L21

Olsen L. F., et al., 1999, A&A, 345, 363

Papovich, C., et al., 2010, ApJ, 716, 1503

Pierpaoli E., Farrar G., 2005, preprint (astro-ph/0507679)

Piffaretti, R., Arnaud, M., Pratt, G. W., Pointecouteau, E., & Melin, J.-B. 2011, A&A, 534, A109

M. Plionis, Lect. Notes Phys. 740 (2008)

Postman, M., Lubin, L. M., Gunn, J. E., Oke, J. B., Hoessel, J. G., Schneider, D. P., & Christensen, J. A. 1996, AJ, 111, 615

Press W. H., Schechter P., 1974, ApJ, 187, 425

LSST Science Collaboration et al., 2009, arXiv e-prints

Laureijs R., et al., 2011, arXiv e-prints

Lima, M. & Hu, W. 2004, Phys. Rev. D, 70, 043504

Lima M., Hu W., 2005, Phys. Rev. D, 72, 043006

Lobo C., Iovino A., Lazzati D., Chincarini G., 2000, A&A, 360, 896

L´opez-Cruz, O., Barkhouse, W. A., & Yee, H. K. C. 2004, ApJ, 614, 679,

Lumsden, S. L., Puxley, P. J., & Hoare, M. G., 2001, MNRAS, 328, 419

Majumdar S., Mohr J. J., 2004, ApJ, 613, 41

Muldrew, S.I.; Hatch, N.A.; Cooke, E.A., 2015, MNRAS, 452, 2528

Mohr J. J., Carlstrom J. E., The Sza Collaboration 2002, in Chen L.-W., Ma C.-P., Ng K.-W., Pen U.-L., eds, ASP Conf. Ser. 257: AMiBA 2001: High-Z Clusters, Missing Baryons, and CMB Polarization The SZ-Array: Configuration and Science Prospects. pp 43

Mei, S., et al. 2009, ApJ, 690, 42

Mei, S., et al. 2009, ApJ, 690, 42

Rykoff, E. S., Rozo, E., Busha, M. T., et al. 2014, ApJ, 785, 104

Rood, H. J., & Sastry, G. N. 1971, PASP, 83, 313

Spergel D., et al., 2015, arXiv e-prints, p. arXiv:1503.03757

Sartoris, B., Biviano, A., Fedeli, C., et al. 2016, MNRAS, 459, 1764

Sandage A., Binggeli B., Tammann G. A., 1985, AJ, 90, 1759

Sarazin, C. L. 1986, Reviews of Modern Physics, 58, 1

Szabo T., Pierpaoli E.,Dong2 F.,Pipino A., Gunn J.,2011, ApJ, 736,1

Schuster H. E., 1980, The Messenger, 22, 7

Smail I., Ivison R. J., Blain A.W., Kneib, J.P., 1998, ApJL, 507, 21

Sutherland W., Saunders W., 1992, MNRAS, 259, 413

Stanford, S. A., et al. 2006, ApJ, 646, L13

Tanaka, M., Kodama, T., Kajisawa, M., Bower, R., Demarco, R., Finoguenov, A., Lidman, C., & Rosati, P. 2007, MNRAS, 377, 1206

van Dokkum, P. G., Franx, M., Kelson, D. D., & Illingworth, G. D. 1998a, ApJ, 504, L17

van Dokkum P. G., 2005, AJ, 130, 2647

Voit, G. M. 2005, RvMP, 77, 207

Wen, Z. L., Han, J. L., & Liu, F. S. 2012, ApJS, 199, 34

Von der Linden A., et al., 2014, MNRAS, 439, 2

Walsh, D., Carswell, R. F., and Weymann, R. J. 1979, Nature,

Wilson G., Muzzin A., Yee H. K. C., Lacy M., Surace J., Gilbank D., Blindert K., Hoekstra, H. et al., 2009, ApJ, 698, 1943 Yee H. K. C., Lopez-Cruz O., 1999, AJ, 117, 1985

York D. G., Adelman J., Anderson, Jr. J. E., Anderson S. F., Annis J., Bahcall N. A., Bakken J. A., Barkhouser, R. et al., 2000, AJ, 120, 1579

Zirm, A. W., et al. 2008, ApJ, 680, 224

Zwicky, F. (1933), Helv. Phys. Acta 6, 110

Zwicky F., Herzog E., Wild P., 1961, Catalogue of galaxies and of clusters of galaxies, Vol. I, Pasadena: California Institute of Technology (CIT), —c1961

Chapter 2

Probing planet-mass objects in Extragalactic systems

This chapter has been previously published in the Astrophysical journal as "Confirmation of Planet mass objects in Extragalactic systems", Bhatiani, Saloni, Dai, Xinyu, Guerras Eduardo 2019 ApJ, Volume 885, Number 1 arXiv: 190911610. It is presented here in its entirety in an updated format.

Abstract

Quasar microlensing serves as a unique probe of discrete objects within galaxies and galaxy clusters. Recent advancement of the technique shows that it can constrain planet-scale objects beyond our native galaxy by studying their induced microlensing signatures, the energy shift of emission lines originated in the vicinity of the black hole of high redshift background quasars. We employ this technique to exert effective constraints on the planet-mass object distribution within two additional lens systems, Q J0158−4325 ($z_l = 0.317$) and SDSS J1004+4112 ($z_l = 0.68$) using *Chandra* observations of the two gravitationally-lensed quasars.

The observed variations of the emission line peak energy can be explained as microlensing of the FeKα emission region induced by planet-mass microlenses. To corroborate this, we perform microlensing simulations to determine the probability of a caustic transiting the source region and compare this with the observed line shift rates. Our analysis yields constraints on the sub-stellar population, with masses ranging from Moon ($10^{-8}M_{\odot}$) to Jupiter ($10^{-3}M_{\odot}$) sized bodies, within these galaxy or cluster scale structures, with total mass fractions of $\sim 3 \times 10^{-4}$ and $\sim 1 \times 10^{-4}$ with respect to halo mass for Q J0158−4325 and SDSS J1004+4112, respectively. Our analysis suggests that unbound planet-mass objects are universal in galaxies, and we surmise the objects to be either free-floating planets or primordial black holes. In this chapter, we present the first-ever constraints on the sub-stellar mass distribution in the intra-cluster light of a galaxy cluster. Our analysis yields the most stringent limit for primordial black holes at the mass range.

2.1 Introduction

The planet to stellar scale astronomical dark matter is also known as massive compact halo objects. It was previously constrained to be less than 10% of the total mass of the Milky Way (Alcock et al. 1998). Recently, unbound planet-mass objects have been discovered by Galactic microlensing studies (Sumi et al. 2011; Mróz et al. 2017) with a mass fraction of a few of 10^{-5} halo mass at the super Earth or Jupiter ranges. In the extragalactic regime, Dai & Guerras (2018) detect planet-mass objects in the Moon to Jupiter mass range with a total mass fraction of 10^{-4} of a $z = 0.295$ lens galaxy, RX J1131−1231. Although tiny in the mass fraction, the detections of these objects open a new window to constrain the demographics of new types of astronomical objects, and the leading candidates are free-floating planets or primordial black holes. A pixel-lensing technique (Ingrosso et al. 2009; Mróz & Poleski 2018) has also been proposed to detect planet-mass objects in the nearby galaxy M31, and the technique has yielded a candidate (Niikura et al. 2019) from recent *Subaru* observations.

Free-floating planets (FFPs) are not gravitationally bound to particular stars and are thought to be ejected or scattered due to dynamical instabilities in the early history of star/planet formation (Rasio et al. 1996; Weidenschilling & Marzari 1996) or combined with other processes such as planetary stripping in stellar clusters and post-main-sequence ejection (Veras & Raymond 2012). It is also possible that a fraction of them form directly from gravitational collapse resembling star/brown dwarf formation down to planet scales (Luhman 2012). The number density of FFPs not only depends on the detailed ejection processes, but also on the planet formation models. Primordial black holes are thought to be formed during the inflation epoch from quantum fluctuations. Therefore, these planet mass objects can either serve as a probe of star/planet formation and scattering process or fundamental physics in the very early universe in the inflation era.

2.2 Quasar microlensing

Extragalactic microlensing is induced by individual stars or lower mass compact objects in the lensing galaxy, and manifests in the time variable magnification of its microimages. In case of quasar microlensing (Chang & Refsdal 1979; Wambsganss 2001; Kochanek 2004), the background quasar is first macrolensed into multiple images by a foreground lensing galaxy, and then light from the quasar is further deflected by the stars within the lens as they align with the quasar image, thus resulting in uncorrelated variability in the macroimages. Quasar microlensing serves as a special tool to study the structure of the accretion disk and spatially resolve the emission region around the supermassive black hole (e.g., Pooley et al. 2007; Anguita et al. 2008; Dai et al. 2010; Mediavilla et al. 2011b; Morgan et al. 2008, 2012; Chen et al. 2011, 2012; Sluse et al. 2012; Guerras et al. 2013; O'Dowd et al. 2015). Since quasar microlensing is produced by the granular mass distribution within the lens, it can be used to probe the stellar content of the lensing galaxy (Paczyński 1986; Morgan et al. 2008; Bate et al. 2011; Blackburne et al. 2014). Furthermore, Dai & Guerras (2018) show that the technique can constrain the rogue planetary distribution, using emission immediately around the black hole in the source quasar, because the Einstein ring of planet lenses match this emission size. The Einstein radius in the source plane is given as

$$R_E = \sqrt{\frac{4GMD_{ls}D_{os}}{c^2 D_{ol}}}, \tag{2.1}$$

where M is the deflector mass and D_{ol}, D_{os}, and D_{ls} are the angular diameter distances between the observer, lens, and source, respectively. Studies of nearby Seyferts reveal relativistically broadened Fe Kα lines, emanating from the innermost regions of the accretion disk (Fabian et al. 1995; Reynolds et al. 2000; Vaughan & Fabian 2004; Young et al. 2005), and this emission is ideal to probe the microlensing signal from planet-mass objects in the lens galaxy. Technically, the image separation induced by planet-mass lenses are of nano-arcsecs; however, since the caustic network is produced by the combination of planet and stars, we keep using the term of microlensing in the paper.

Over the last decade, *Chandra* performed X-ray monitoring observations of several gravitationally lensed quasars to constrain the extent of the emission region around the SMBH in the X-rays (Chartas et al. 2009, 2012, 2017; Dai et al. 2010, 2019; Chen et al. 2012; Guerras et al. 2017, 2018). Among these lensed quasars, some of the systems exhibit emission line peak variations and double line features, e.g., RX J1131−1231 (Chartas et al. 2012, 2017), SDSS J0924+0219 (Chen et al. 2012), Q J0158−4325, and SDSS J1004+4112 (Chartas et al. 2017). The line peak variation and splitting have not been observed in well studied Seyferts, such as MCG–6–30–15 (Kara et al. 2014), NGC 4151 (Beuchert et al. 2017), MCG–05–23–16 (Dewangen et al. 2003), NGC 3516 (Turner et al. 2002), and Mrk 766 (Pounds et al. 2003), where the Fe Kα line peak shows little variability for a single source. Relativistic Fe Kα lines have been predicted to peak within a range of energies $\sim$ 5–8 keV conditional upon the black hole spin, observing angle, and other factors (Brenneman & Reynolds 2006) for different sources; however, for a single source, such large variations in energy up to a factor of two have not been recorded. For *Chandra* observations of lensed quasars, these line variations are uncorrelated between the images and have been frequently detected during the course of the monitoring observations. Chartas et al. (2017) performed further analysis of lensed quasars with a larger set of observations and confirmed the microlensing interpretation of the observed line shifts in the X-ray spectrum of lensed quasars. Because of the microlensing effect, a strip of the Fe Kα emission region is magnified which, in general, has a different average energy compared to that from the whole Fe Kα region, and thus introduces shift or additional line peaks (e.g., Popović et al. 2006). Chartas et al. (2017) also excluded other non-microlensing interpretations, e.g., emissions arising from hot spots and patches of an inhomogeneous disk, intrinsic absorption of the continuum, occultations or radiations from the ionized accretion disk. The most well-studied source, RX J1131−1231, was observed 38 times during the period of the observations, and the team has detected Fe Kα line shifts in 78 out of 152 energy spectra at a 90% confidence level, of which

21 lines are detected at 99% confidence level. These line energy variation rates were interpreted by Dai & Guerras (2018) as caustic crossing events of planet-sized deflectors within the lensing galaxy. A stars-only model is ruled out because the predicted caustic encounter rate is too low compared to the observational evidence.

This chapter covers the analysis of microlensing caustic encounter rates in two gravitationally-lensed systems, SDSS J1004+4112 and Q J0158−4325, to constrain the mass fraction of the unbound planet-mass objects. The chapter is organized as follows. In Section 2.3, I introduce the two systems and their *Chandra* data, including our method to calculate the line shift rates. In Section 2.4, I describe the microlensing analysis that involves simulating magnification maps to substantiate the observed rates. I summarize the results and conclude with discussions under Section 2.5.

2.3 Observational Data

We focus on two gravitationally lensed systems, Q J0158−4325 and SDSS J1004+4112. Q J0158−4325 (also CTQ 414; Maza et al. 1995; Morgan et al. 1999, 2008; Faure et al. 2009; Chen et al. 2012) is a doubly lensed quasar with $z_l = 0.317$, $z_s = 1.29$, and an image separation of $1.''22$. The second object of interest, SDSS J1004+4112, is a unique quintuple and large-separation lens system (Inada et al. 2003; Oguri 2004, 2010; Sharon et al. 2005; Ota et al. 2006; Inada et al. 2008) comprising of a massive lens galaxy cluster at a redshift of $z_l = 0.68$ and a source quasar at $z_s = 1.734$ with a maximum image separation of $15''$.

These two sources have been monitored relatively frequently by *Chandra*, 12 times between November 2010 and June 2015 for Q J0158−4325 and 10 times between January 2005 and June 2014 for SDSS J1004+4112. The observations

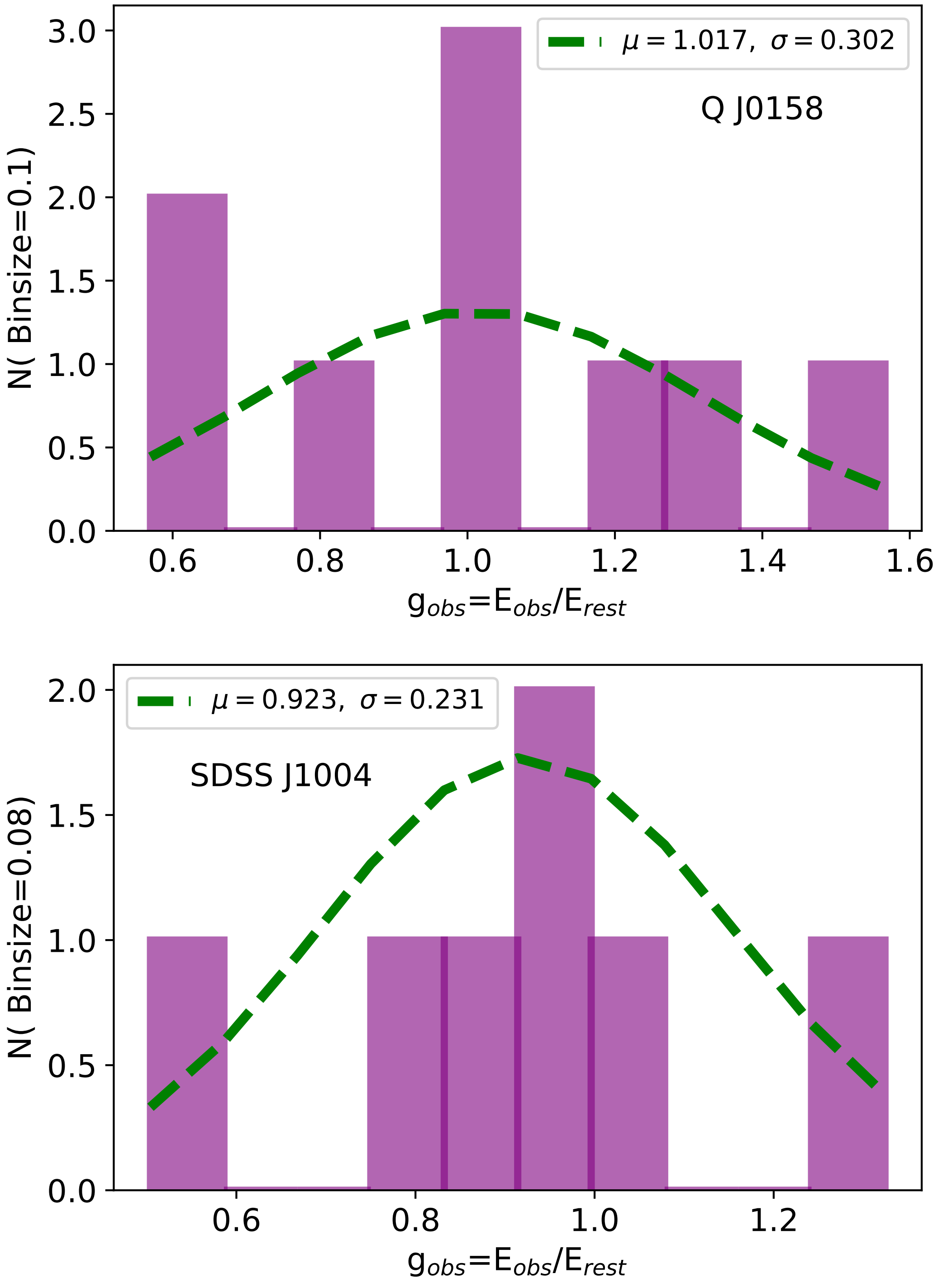

Figure 2.1 Distribution of the Fe Kα line energy shifts for both image A and image B of Q J0158−4325 (left) and all four images of SDSS J1004+4112 (right). Here we include only those lines that are detected at 90% confidence level. A Gaussian is fit to the distribution yielding the g_{peak} of the distribution. We have selected a bin size of 0.08 for Q J0158−4325 and 0.1 for SDSS J1004+4112 for illustration purposes; however the choice of bin size does not significantly change the g$_{peak}$ value.

Table 2.1. Observed Line Shift Rates for Q J0158−4325 and SDSS J1004+4112

Source	*Chandra* Pointings	Observed Line Shift Rates >90% detected $> 1\sigma$ shift	>90% detected $> 3\sigma$ shift	>99% detected $> 1\sigma$ shift	>99% detected $> 3\sigma$ shift
Q J0158−4325[a]	12	0.250	0.208	0.083	0.083
A	12	0.416	0.333	0.166	0.166
B	12	0.083	0.083	0.000	0.000
SDSS J1004+4112[b]	10	0.150	0.125	0.100	0.075
A	10	0.100	0.100	0.100	0.100
B	10	0.200	0.200	0.000	0.000
C	10	0.100	0.100	0.100	0.100
D	10	0.200	0.100	0.200	0.100

[a] Line shift rates for the total of all images(A and B) of Q J0158−4325

[b] Line shift rates for the total of all images(A, B, C and D) of SDSS J1004+4112

have shown credible evidence of large redshifted or blueshifted Fe Kα lines with respect to the rest frame peak energy, $E_{rest} = 6.4$ keV for the two systems (Chartas et al. 2017), and moreover, double Fe Kα lines have also been detected on some occasions. Hereafter, we use the generalized Doppler shift,

$$g = \frac{E_{obs}}{E_{rest}}, \tag{2.2}$$

to characterize the shifts. Figure 2.1 shows the g distribution of Fe Kα lines detected in SDSS J1004+4112 and Q J0158−4325 (Chartas et al. 2017), ranging between 0.6 to 1.5 for Q J0158−4325 and 0.5 to 1.3 for SDSS J1004+4112. For the 12 *Chandra* pointings of Q J0158−4325, ten relativistic Fe Kα lines were detected at more than 90% confidence, among which three Fe Kα lines are detected at more than 99% confidence with one double line detection. For the ten *Chandra* pointings of SDSS J1004+4112, eight relativistic Fe Kα lines are detected at more than 90% confidence, and among these six Fe Kα lines are detected at more than 99% confidence with one double line detection. Thus, SDSS J1004+4112 and Q J0158−4325 are the best targets to model the line shift rates induced by microlensing after the well-monitored lens RX J1131−1231. These line energy shifts can be ascribed to a differential magnification of a section of the emission region bearing a range of g values as a caustic transits the innermost disk, thereby resulting in the variation of observed Fe Kα line profile (Popović et al. 2003, 2006; Chartas et al. 2017; Krawczynski & Chartas 2017; Ledvina et al. 2018). To calculate the line shift rate, we first identify the peak (g_{peak}) of the g distribution by a fitting a Gaussian to the distribution, yielding $g_{peak} = 0.923$ for SDSS J1004+4112 and $g_{peak} = 1.017$ for Q J0158−4325 (Figure 2.1). For this purpose, we use the lines detected at $> 90\%$ confidence level (See Table 6 and Table 7 of Chartas et al. (2017)). The significance of the line energy shift from the peak is determined for each detected lines using their respective measured energies and uncertainties. We list the line shift rates under different selection cuts in Table 2.1. For the subsequent microlensing event rate analysis, we have conservatively considered only those lines that were detected at a confidence level of $> 99\%$ and exhibit a line shift of $> 3\sigma$ from the g peak. For both SDSS J1004+4112 and Q J0158−4325, we have conducted an independent analysis of the brightest image A together with a combined analysis of all the images. Owing to the limited S/N of our observations, we have restricted the analysis of individual images to the highest S/N image A.

Table 2.2. Macro Lens model Parameters for Q J0158−4325and SDSS J1004+4112

Object	Image	κ	γ	κ_*	κ_*/κ
Q J0158−4325	A	0.727	0.187	0.020	0.028
	B	0.994	0.285	0.070	0.070
SDSS J1004+4112	A	0.763	0.300	0.007	0.010
	B	0.696	0.204	0.006	0.010
	C	0.635	0.218	0.006	0.010
	D	0.943	0.421	0.009	0.010

2.4 Microlensing Analysis

To explain the occurrence of the energy shifts of the Fe Kα lines emitted from the accretion disk, we perform a microlensing analysis that simulates the caustic encounter rates that contribute to the aforementioned line shifts. In quasar microlensing, the gravitational field of the local distribution of the microlenses affects the amplification of the light passing through the region of the lens galaxy. These amplification variations as a function of the source position are represented by a microlensing magnification map (Kayser et al. 1986; Wambsganss et al. 1990a), comprising of a complex mesh of caustics, along which the magnification diverges, surrounded by low magnification regions. The statistical attributes of the maps, such as the density of caustics, are governed by three main model parameters namely κ (convergence), γ (shear), and κ_s or κ_* (surface mass density in smoothly distributed or discrete matter, respectively), where $\kappa = \kappa_s + \kappa_*$. We also define α as the mass fraction of different components with respect to the total surface mass density, e.g., for the stellar component $\alpha_* = \kappa_*/\kappa$.

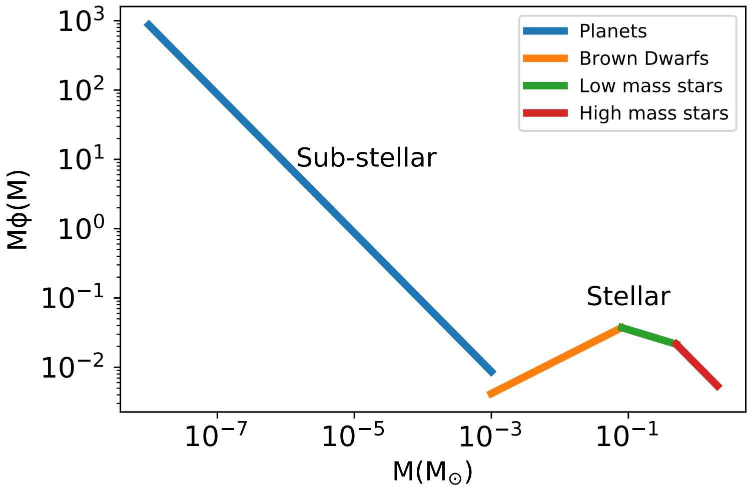
10^3
10^2
10^1
10^0
10^{-1}
10^{-2}
$M\phi(M)$
10^{-7}
10^{-5}
10^{-3}
10^{-1}
$M(M_\odot)$
Planets
Brown Dwarfs
Low mass stars
High mass stars
Sub-stellar
Stellar

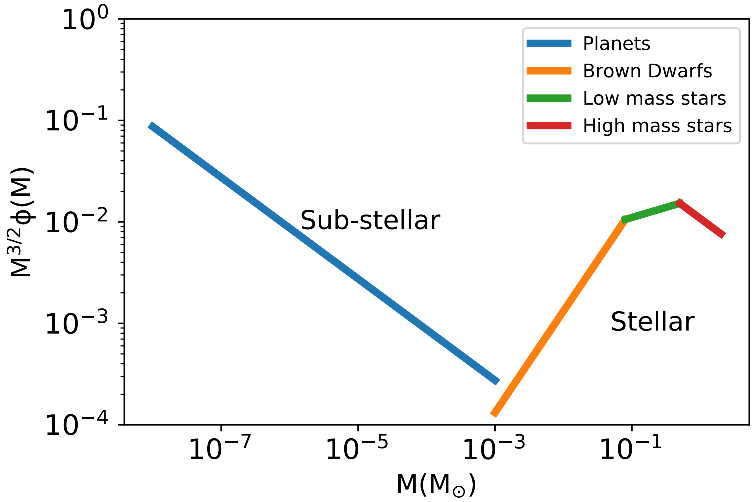
10^0
10^{-1}
10^{-2}
10^{-3}
10^{-4}
$M^{3/2}\phi(M)$
10^{-7}
10^{-5}
10^{-3}
10^{-1}
$M(M_\odot)$
Planets
Brown Dwarfs
Low mass stars
High mass stars
Sub-stellar
Stellar

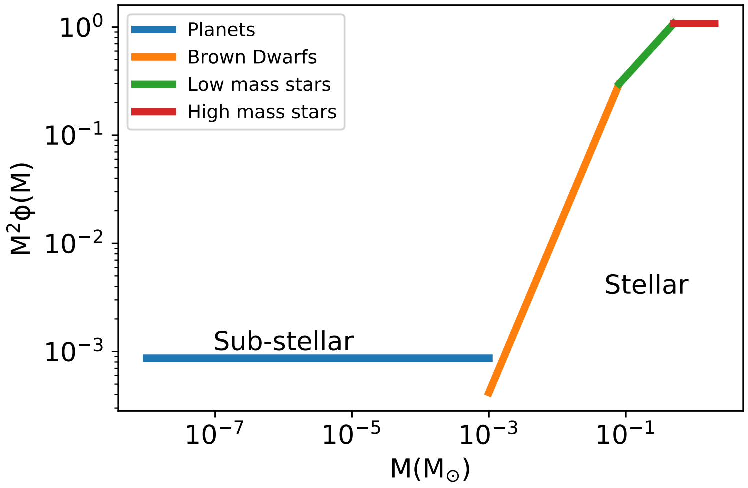
10^0
10^{-1}
10^{-2}
10^{-3}
$M^2\phi(M)$
10^{-7}
10^{-5}
10^{-3}
10^{-1}
$M(M_\odot)$
Planets
Brown Dwarfs
Low mass stars
High mass stars
Sub-stellar
Stellar

Figure 2.2 Discrete lens mass function is plotted against the lens mass on a logarithmic scale for the stellar and planet populations with the mass fractions of $\alpha_* = 0.1$ and $\alpha_p = 10^{-4}$, respectively. Integration of $M\phi(M)$(Top) and $M^2\phi(M)$(Bottom) over the logarithmic mass range represents the number of microlenses and mass within the two population regimes respectively. We see that the number of microlenses is dominated by planetary objects while the total mass is dominated by stars. The caustic density, proportional to $M^{1/2}$, is represented by the integration of $M^{3/2}\phi(M)$(Middle) over the logarithmic mass range. It is evident that the addition of planetary microlenses results in an increased contribution to the caustic density in contrast to the exclusively stellar scenario.

We produce magnification maps using the inverse polygon mapping (IPM) method developed by Mediavilla et al. (2006, 2011). The macro model parameters for Q J0158−4325 are adopted from Morgan et al. (2012), where the lens galaxy is modeled by a combination of de Vaucouleurs and NFW components with the best fit mass-to-light ratio to be 0.1. For SDSS J1004+4112, we use the microlensing parameters (κ, γ) in Guerras et al. (2017), where they employ a cluster mass model for the lens from Oguri (2010). As a cluster lens, microlensing in SDSS J1004+4112 is induced by stars and planets in the intra cluster light (ICL). We extrapolate the surface brightness of ICL to the image locations and obtain the mass fraction of $\alpha_* \sim 0.01$. Our adopted value is aligned with the estimates of α_* for another galaxy cluster, MACS J1149+2223 ($z_l = 0.54$), at similar distances to the cluster center (Venumadhav et al. 2017; Oguri et al. 2018). Table 2.2 lists the global convergence, shear, stellar surface mass density, stellar mass fractions for all images of Q J0158−4325 and SDSS J1004+4112.

The mass function for the stellar population is modeled as a three-segment power-law function, $\phi(M) \propto M^{-\eta}$, with the mass range, 0.001–0.08 $M_\odot$, corresponding to the brown dwarf population, 0.08–0.5 $M_\odot$ for the low mass range, and 0.5–2 $M_\odot$ for the high mass range (Figure 2.2). The power law indices are assumed as 0.5, 1.3, and 2, respectively, for the brown dwarfs, low mass, and high mass stars (Dai & Guerras 2018). The normalization of the stellar mass function is set such that we achieve the expected stellar surface mass fractions for each image. Subsequently, we model the sub-stellar population that includes planet-mass objects that serve as additional microlenses with a surface density of κ_p, (Figure 2.2). We particularly focus on rogue planets, or free-floating planets (Dai & Guerras 2018; Sumi et al. 2011; Strigari et al. 2012), as the planets bound to stars are positioned way inside the Einstein ring of the parent star which is unable to produce any significant effect on the magnification maps. The planetary mass distribution is drawn from a power law model, $\phi_p(M) \propto M^{-\eta_p}$ with a power index of $\eta_p = 2$ (Strigari et al. 2012; Dai & Guerras 2018). Here, the normalization, $\alpha_p = \kappa_p/\kappa$, is considered as a free parameter, and we have explored multiple variations to exert effective constraints. Hence, we generate multiple sets of magnification maps with α_p ranging from 10^{-5} to 10^{-3}, corresponding to 10^2 to 10^4 Moon ($10^{-8}M_\odot$) to Jupiter ($10^{-3}M_\odot$) mass planets per main sequence star.

Due to the high computation cost associated with generating extensive magnification maps that accommodate a large number of lenses, the size of the magnification maps is restricted to 400×400 r_g with a pixel scale of 0.375 r_g (gravitational radius units). The dimension of the discrete lens population used in IPM is much larger to accurately calculate the magnification map. For instance, the computed magnification map for SDSS J1004+4112 is of dimension 0.53 R_E (Einstein radius of 1 $M_\odot$ units), while the dimension of the deflectors used in IPM is 58.89 R_E for star-only maps, while the combined map (consisting of stars and planets both) uses a square discrete lens region of the dimension 16.83 R_E in the lens plane. For each set of parameters (κ, γ, α_*, α_p), we generate 30 random

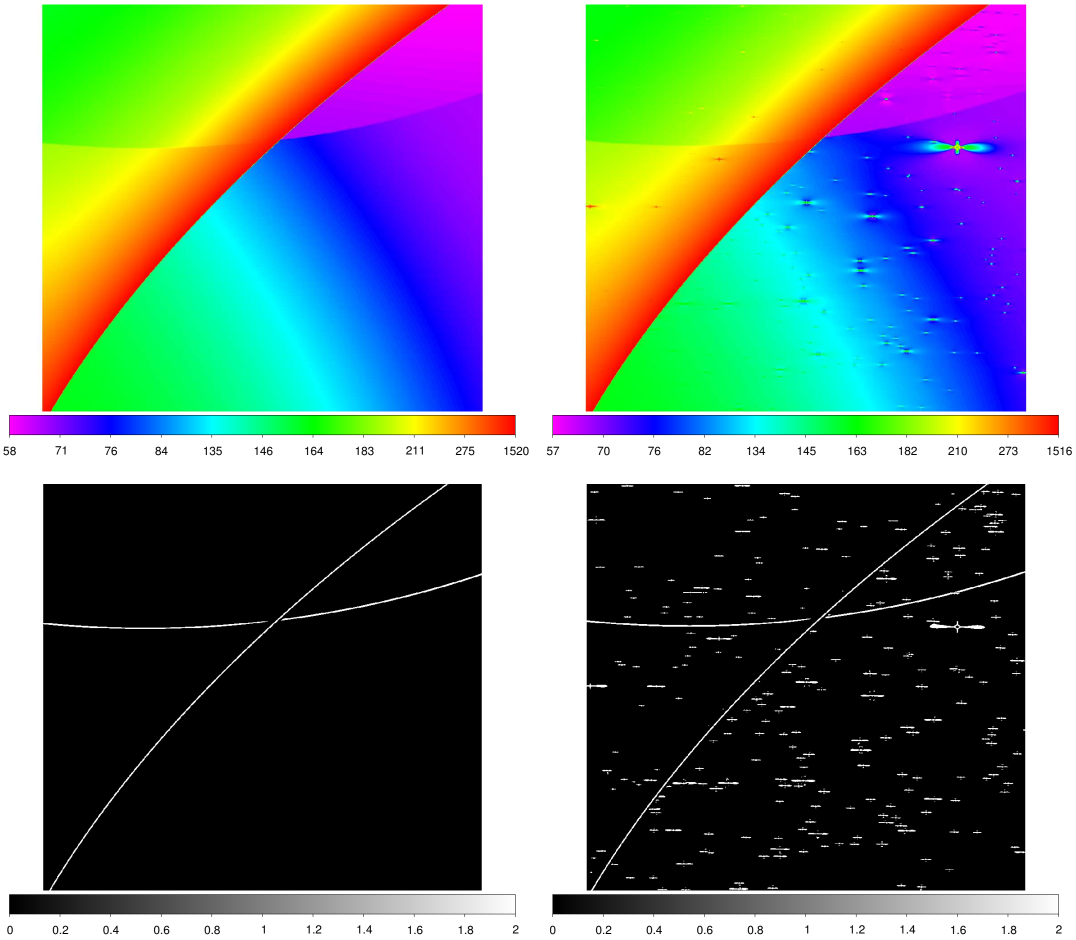

Figure 2.3 Microlensing magnification map of Q J0158−4325 with stars only (Top Left) and with a dimension of (400 r_g)^2. The color bars indicate the relative magnification value of the map. The same magnification map but with the additional planet population with a planet mass fraction of $\alpha_p = 0.003$ (Top right). The caustic density is much higher with the additional planets. The magnification maps convolved with a sharpening kernel with a source size of two pixels for stars only (Bottom left) and with planets (Bottom Right). We can see that the sharpened images have captured the caustic network of the map.

realizations of magnification maps to sample the large scale variations in the caustic density. Figure 2.3 shows some example magnification maps.

Following the computation of the magnification maps, we measure the caustic encounter rates as a function of the source size. For this, we employ an edge detection algorithm to extract the discontinuities in the maps (for an analytic approach, see also Witt 1990). First, we smooth the image with a small constant kernel of 3×3 pixels (about 1 r_g^2) to reduce the computational noise by blurring the image slightly. Next, we convolve the map with an $(n_s + 4) \times (n_s + 4)$ sharpening kernel for a source size of n_s in pixels, such that the central $n_s \times n_s$ pixels bear a positive value x while the rest of the background pixels carry a value of -1. Here x is posited as $((n_s + 4)^2 - n_s^2)/n_s^2$ such that when we apply this convolution matrix to the map, the pixels for which the ratio of summation over the source pixels to the summation over background pixels $(\Sigma_s/\Sigma_b) > 1$ result in a positive value, whereas the remaining pixels return a negative or zero value. The source size in pixels is varied on a logarithmic scale up to $\sim 10\ r_g$. Because for a source larger than a pixel, different parts of the source experience different magnification, therefore the pliable source size, n_s, incorporates the finite source size effects. The sharpened magnification maps vividly reveals its salient features, i.e., the caustic structure, by improving the contrast (Figure 2.3). We determine the probability of the caustic encountering the source region by calculating the ratio of the positive pixels over all the valid pixels. For all the 30 maps attached to a given set of model parameters, the model caustic encounter probability for a particular source size is estimated as the average over all the 30 probabilities and the uncertainty is characterized by the variance of these probabilities.

Figure 2.4 shows the model caustic encounter probability from our microlensing analysis for different planet mass fractions and Fe Kα source sizes. The model probability shows an increase with additional planetary population and the source size for both Q J0158−4325 and SDSS J1004+4112. Hereafter, we have conservatively used the largest source size to test the viability of the stars-only model and constrain the planet fraction, α_p. This source size is consistent with the recent constraints on the X-ray reflection region of between 5.9–7.4 r_g (Dai et al. 2019). We compare the model predictions with the observed line shift rates from the $> 99\%$ detected and $> 3\sigma$ shifted lines for the highest S/N image A and the combined average of all images. Based on the predictions for image A of Q J0158−4325, we find that the stars-only model can be completely ruled out by 16.6 σ, as it fails to explain the observed line shift rate. As for the image A of SDSS J1004+4112, the stars-only model can only be marginally ruled out as it is at 2.6 σ below the observed line shift rate. The analysis results from the combined images disfavor the exclusively stellar scenario at the significance levels of 13.284 σ and 4.95 σ for Q J0158−4325 and SDSS J1004+4112, respectively. For models with additional planets, the model predictions at a reference size of 6 r_g show an ascent with increasing α_p until a model is congruent with the observed event rate. In case of Q J0158−4325, we constrain the planet mass fraction with respect to total halo mass in the mass range of 10^{-8}–10^{-3} $M_\odot$ as $10^{-4} < \alpha_p < 6 \times 10^{-4}$, and for SDSS J1004+4112, the constraint is $2 \times 10^{-5} < \alpha_p < 10^{-4}$.

2.5 Chapter Summary & Discussion

We infer a population of planet-mass objects in two extragalactic systems, one lens galaxy Q J0158−4325 at $z = 0.317$ and one lens cluster SDSS J1004+4112 at $z = 0.68$, with the leading candidates being free-floating planets and/or primordial black holes. We have excluded the stars-only model for Q J0158−4325

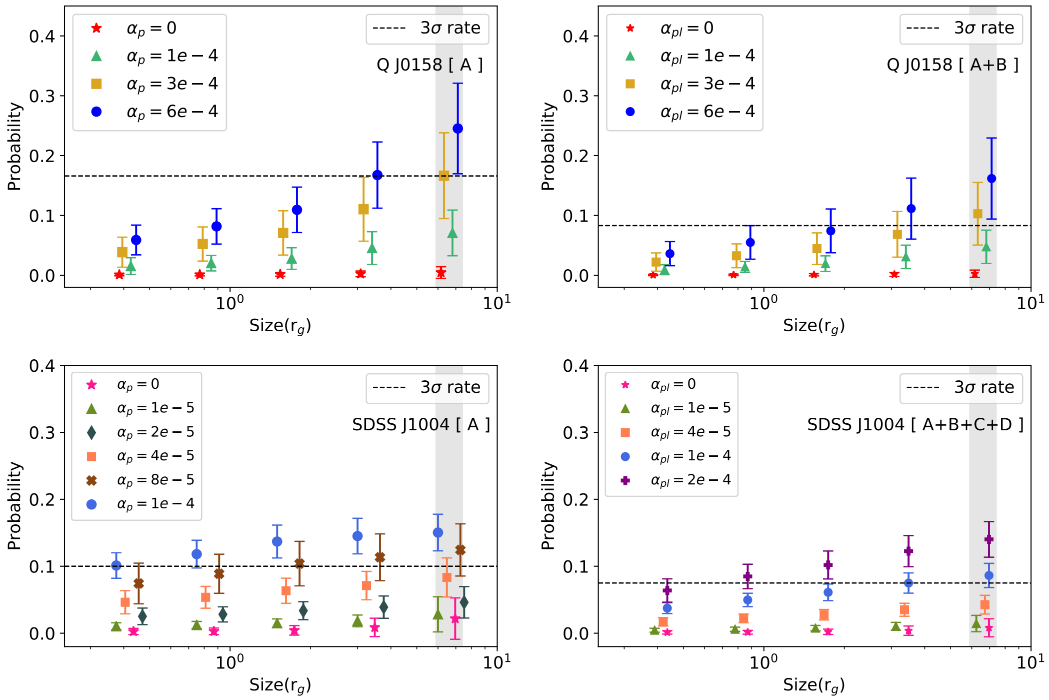

Figure 2.4 Model probabilities of observing an Fe Kα line energy shift as a function of source size for image A (Left) and combined average of all images (Right) of Q J0158−4325 and SDSS J1004+4112 respectively. Here, the different symbols represent models with the different planet mass fractions (α_p). The black dashed line mark the observed $> 99\%$ detected line shift rates at 3σ level. The gray shaded region depicts the recent constraints on the size of the X-ray reflection region by Dai et al. (2019). For image A, the stars-only model is ruled out for all source sizes of Q J0158−4325, and for SDSS J1004+4112, the stars-only model is only viable at the largest source size considered with about 2σ deviation from the observed rate. For the combined case, the stars-only model is significantly excluded for all source sizes of Q J0158−4325 and SDSS J1004+4112. We constrain the halo mass fractions of planets in the mass range of 10^{-8}–10^{-3} $M_\odot$ to be $10^{-4} < \alpha_p < 6 \times 10^{-4}$ and $4 \times 10^{-5} < \alpha_p < 2 \times 10^{-4}$ for Q J0158−4325 and SDSS J1004+4112, respectively.

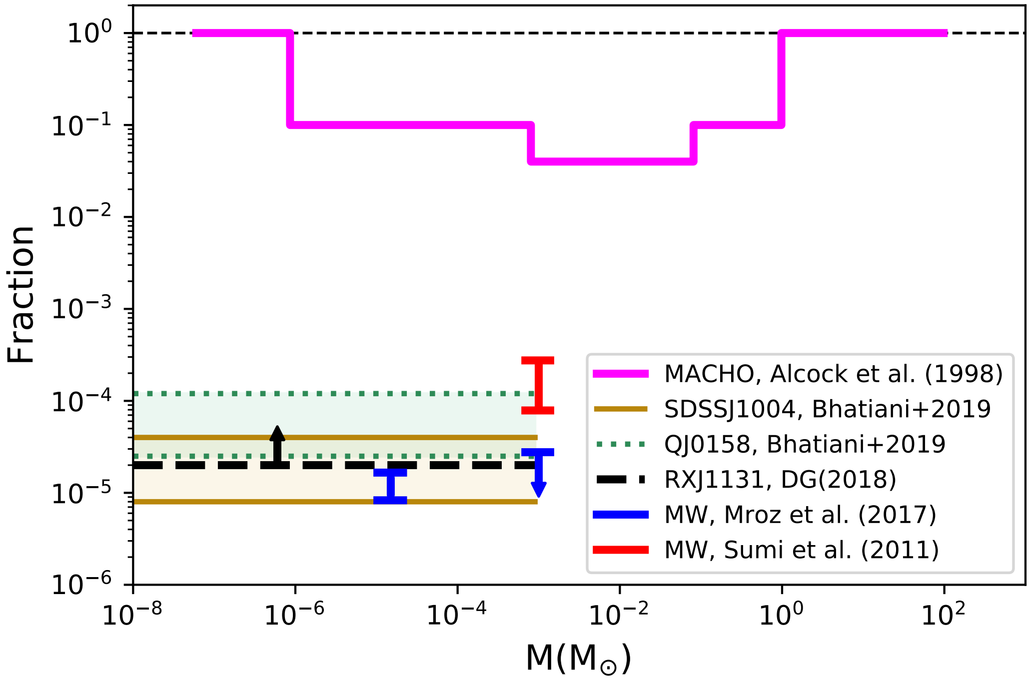

Figure 2.5 Mass fraction of unbound planets in the galactic halo is studied as a function of mass in the sub-stellar regime. The constraints presented in this work are shown in gold and green for Q J0158−4325 and SDSS J1004+4112, respectively, with a bin size of one decade in mass. Previous constraints at super earth mass and Jupiter mass for Milky Way by Mróz et al. (2017) are shown in blue. Constraints for Jovian planets in the MW by Sumi et al. (2011) are shown in red. Prior constraints on MACHOs by Alcock et al. (1998) ranging from Moon mass to $100M_\odot$ have been plotted. We also find that our results are consistent with the constraints from Dai & Guerras (2018), as shown in black, on free-floating planets from Moon to Jupiter mass range for RX J1131−1231.

and SDSS J1004+4112 and accepted the scenario that favors the combination of stellar and unbound planetary microlenses. Together with the previous detection in RX J1131−1231 (Dai & Guerras 2018) and within the Milky Way (Mróz et al. 2017), our analysis results suggest that unbound planet-mass compact objects are universal in galaxies. The bound planets do not contribute to the lensing signal, because at extragalactic lensing scales, their distance to the parent star is too small compared to the Einstein ring of the star. The cold dark matter sub-halos potentially can also extend to the planet-mass range, and assuming a halo mass function of $dn/dM \propto M^{-1.8}$ (e.g., Moore et al. 1999; Klypin et al. 1999; Helmi et al. 2002), 0.05% of the halo mass will be in the Moon to Jupiter mass range, which is consistent with our constraints. However, with an NFW density profile, they will not be efficient micro or nano-lenses to produce the observed lensing signatures.

It is important to distinguish the cross sections for microlensing high magnification events and line shift events. For high magnification events, the cross section is proportional to the area of Einstein ring, which is proportional to the mass of the microlens. For line shift events, we need a caustic on the source region, and thus the cross section is proportional to $m^{1/2}\Delta R$, where ΔR is the characteristic size of the emission region. Smooth high magnification regions bound by the caustic curves are not conducive to these line shift events. Since we constrain the mass fraction of the planet population to be several orders of magnitude smaller than the stellar population, this implies that most of the high magnification area produced by stars are in the smoothly varying regions of the magnification map, using the ultra-compact Fe Kα emission region as a size reference. This can be seen in the analytic values of lens number, total mass, and caustic density from Figure 2.2. This leads to an important, testable prediction for this model — for the Fe Kα line shifts produced by the relatively isolated microlensing caustics produced by planets, the optical or even the X-ray continuum flux will experience small to moderate microlensing flux magnification, because the optical continuum emission size is much larger and not sensitive to the magnification produced by planet-mass lenses. I.e., the Fe Kα line shifts accompanied by little to moderate flux magnification in the optical or X-ray bands will be the further confirmation for the presence of planet-mass objects. This does not mean that those line shifts occurring with large optical or X-ray continuum flux magnification are not caused by planet-mass objects, because the caustics produced by stars and planets can be clustered together. Additionally, since the *Chandra* observations are semi-randomly scheduled, it is important to compare the line shift rate with the model caustic density detailed in this paper. An alternative method counts the number of caustics encountered along a track in the magnification pattern corresponding to the monitoring length and compare with the observed number of line shifts. This method assumes that the observations occurred exactly at the caustic-crossing time, which is not representing the real situation. In essence, it is the caustic density rather than number that matters, when the observations are randomly scheduled.

Another source of uncertainty is related to the detection threshold of the shifted Fe Kα lines. Here, we include only lines that are detected at the greater than 99% confidence limit, when calculating the line shift rates. This excludes a significant fraction of the shifted lines detected at lower significance in 90–99% range. Although each of these individual lines are less reliable, collectively, the presence of these weaker lines are quite convincing. Including these weaker lines will change the line shift rates and the constraints on the planet fractions. In addition, our analysis is based on either the line shift rates in the brightest image or the average of all images. While focusing on the brightest image subjects less on the line detection bias but more on microlensing biases, because the brightest image tends to be more microlensing active, using the average rate from all images subjects more to the detection biases from those fainter images. Therefore, new and deeper observations are still needed to better characterize those weaker lines and measure the line shift rates. We summarize the current constraints on unbound planet mass object in galaxies and ICL of a cluster in Figure 2.5, including those from this paper for Q J0158−4325 and SDSS J1004+4112, RX J1131−1231 of Dai & Guerras (2018), and Milky Way measurements at super Earth and Jupiter regime (Sumi et al. 2011; Mróz et al. 2017). Here, we divide the planet mass fraction to each decade of mass interval to facilitate an easy comparison with other studies. Although these initial measurements of unbound planet mass fraction can subject to systematic uncertainties and can be improved in future analysis with better data and modeling, these measurements converge at a planet mass fraction of $\sim 10^{-5}$ with respect to the total mass of the galaxy per decade of mass interval. This should be compared with future, more precise theoretical predictions of planet formation and scattering models and determine whether FFPs are sufficient to explain the measured unbound planet mass fractions. Our measured planet mass fraction of $\sim 10^{-5}$ per decade mass can also serve as an upper limit for more exotic objects such as primordial black holes, since we expect FFPs will contribute significantly to the unbound population. This is the most stringent limit for primordial black hole demographics at the mass range of 10^{-8}–$10^{-3} M_\odot$.

Acknowledgements

We thank S. Mao and S. Dong for stimulating discussion, C. W. Morgan for providing the macro lens parameters for Q J0158−4325, and the anonymous referee for helpful comments. We acknowledge the financial support from the NASA ADAP program NNX17AF26G, NSF grant AST-1413056, and SAO grants AR7-18007X and GO7-18102B. The microlensing magnification maps were computed at the OU Supercomputing Center for Education & Research (OSCER) at the University of Oklahoma (OU).

References

Alcock, C., et al. 1998, ApJ, 499, L9

Anguita, T., Schmidt, R. W., Turner, E. L., et al. 2008, A&A, 480, 327

Bate, N. F., Floyd, D. J. E., Webster, R. L., & Wyithe, J. S. B. 2011, ApJ, 731, 71

Beuchert, T., Markowitz, A. G., Dauser, T., et al. 2017, A&A, 603, A50

Blackburne, J. A., Kochanek, C. S., Chen, B., Dai, X., & Chartas, G. 2014, ApJ, 789, 125

Brenneman, L. W., & Reynolds, C. S. 2006, ApJ, 652, 1028

Chang, K., & Refsdal, S. 1979, Nature, 282, 561

Chartas, G., Kochanek, C. S., Dai, X., Poindexter, S., & Garmire, G. 2009, ApJ, 693, 174

Chartas, G., Kochanek, C. S., Dai, X., et al. 2012, ApJ, 757, 137

Chartas, G., Krawczynski, H., Zalesky, L., et al. 2017, ApJ, 837, 26

Chen, B., Dai, X., Kochanek, C. S., et al. 2011, ApJ, 740, L34

Chen, B., Dai, X., Kochanek, C. S., et al. 2012, ApJ, 755, 24

Dai, X., Kochanek, C. S., Chartas, G., et al. 2010, ApJ, 709, 278

Dai, X. & Guerras, E. 2018, ApJ, 853, L27

Dai, X., Steele, S., Guerras, E., Morgan, C. W., & Chen, B. 2019, arXiv:1901.06007

Dewangan, G. C., Griffiths, R. E., & Schurch, N. J. 2003, ApJ, 592, 52

Fabian, A. C., Nandra, K., Reynolds, C. S., Brandt, W. N., Otani, C., Tanaka, Y., Inoue, H., & Iwasawa, K. 1995, MNRAS, 277, L11

Faure, C., Anguita, T., Eigenbrod, A., et al. 2009, A&A, 496, 361

Guerras, E., Mediavilla, E., Jimenez-Vicente, J., et al. 2013, ApJ, 764, 160

Guerras, E., Dai, X., Steele, S., et al. 2017, ApJ, 836, 206

Guerras, E., Dai, X., & Mediavilla, E. 2018, arXiv:1805.11498

Helmi, A., White, S. D., & Springel, V. 2002, Phys. Rev. D, 66, 063502

Inada, N., et al. 2003, Nature, 426, 810

Inada, N., Oguri, M., Falco, E. E., Broadhurst, T. J., Ofek, E. O., Kochanek, C. S., Sharon, K., & Smith, G. P. 2008, PASJ, 60, L

Ingrosso, G., Novati, S. C., de Paolis, F., et al. 2009, MNRAS, 399, 219

Kara, E., Fabian, A. C., Marinucci, A., et al. 2014, MNRAS, 445, 56

Kayser, R., Refsdal, S., Stabell R. 1986, A&A, 166, 36

Klypin, A., Kravtsov, A. V., Valenzuela, O., & Prada, F. 1999, ApJ, 522, 82

Kochanek, C. S. 2004, ApJ, 605, 58

Krawczynski, H., & Chartas, G. 2017, ApJ, 843, 118

Ledvina, L., Heyrovský, D., Dovčiak, M. 2018, ApJ, 863, 66

Luhman, K. L. 2012, ARA&A, 50, 65

Maza, J., Wischnjewsky, M., Antezana, R., & González, L. E. 1995, RMxAA, 31, 119

Mediavilla, E., Muñoz, J. A., Lopez, P., et al. 2006, ApJ, 653, 942

Mediavilla, E., Mediavilla, T., Muñoz, J. A., et al. 2011, ApJ, 741, 42

Mediavilla, E., Munoz, J. A., Kochanek, C. S., et al. 2011b, ApJ, 730, 16

Moore, B., Ghigna, S., Governato, F., et al. 1999, ApJ, 524, L19

Morgan, N. D., Dressler, A., Maza, J., Schechter, P. L., & Winn, J. N. 1999, AJ, 118, 1444

Morgan, C. W., Kochanek, C. S., Dai, X., Morgan, N. D., & Falco, E. E. 2008, ApJ, 689, 755-761

Morgan, C. W., Hainline, L. J., Chen, B., et al. 2012, ApJ, 756, 52

Mróz, P., Udalski, A., Skowron, J., et al. 2017, Nature, 548, 183

Mróz, P., & Poleski, R. 2018, AJ, 155, 154

Niikura, H., Takada, M., Yasuda, N., et al. 2019, Nature Astronomy

O'Dowd M. J., Bate N. F., Webster R. L., Labrie K., Rogers J., 2015, ApJ, 813, 6

Oguri, M., Inada, N., Keeton, C. R., et al. 2004, ApJ, 605, 78

Oguri, M. 2010, PASJ, 62, 1017

Oguri, M., Diego, J. M., Kaiser, N., Kelly, P. L., & Broadhurst, T. 2018, PhRvD, 97, 023518

Ota, N., et al. 2006, ApJ, 647, 215

Paczynski, B. 1986, ApJ, 301, 503

Popović, L. Č., Mediavilla, E. G., Jovanović, P., & Muñoz, J. A. 2003b, A&A, 398, 975

Popović, L. Č., Jovanović, P., Mediavilla, E., et al. 2006, ApJ, 637, 620

Pooley, D., Blackburne, J. A., Rappaport, S., & Schechter, P. L. 2007, ApJ, 661, 19

Pounds K.A., Reeves J.N., Page K.L., Wynn G.A., O'Brien P.T., 2002, MNRAS, 342, 1147

Rasio, F. A. & Ford, E. B. 1996, Science, 274, 954

Reynolds, C. S., & Wilms, J. 2000, ApJ, 533, 821

Sharon, K., et al. 2005, ApJ, 629, L73

Sluse, D., Hutsemekers, D., Courbin, F., Meylan, G., & Wambsganss, J. 2012, A&A, 544, A62

Strigari, L. E., Barnabè, M., Marshall, P. J., & Blandford, R. D. 2012, MNRAS, 423, 1856

Sumi, T., Kamiya, K., Bennett, D. P., et al. 2011, Nature, 473, 349

Turner, T. J., et al. 2002, ApJ, 574, L123

Vaughan, S., & Fabian, A. C. 2004, MNRAS, 348, 1415

Venumadhav, T., Dai, L., & Miralda-Escudé, J. 2017, ApJ, 850, 49

Veras, D., & Raymond, S. N. 2012, MNRAS, 421, L117

Wambsganss, J. 1990, in Lecture Notes in Physics, Berlin Springer Verlag, Vol. 360, Gravitational Lensing, ed. Y. Mellier, B. Fort, & G. Soucail, 186–191 Wambsganss, J., Witt, H. J., & Schneider, P. 1992, A&A, 258, 591

Wambsganss, J. 2001a, in Microlensing 2000: A new Era of Microlensing Astrophysics, ed. J.W.Menzies and P.D.Sackett ASP Conf. Series, 239, 351

Weidenschilling, S. J. & Marzari, F. 1996, Nature, 384, 619

Witt, H. J. 1990, A&A, 236, 311

Young, A. J., Lee, J. C., Fabian, A. C., Reynolds, C. S., Gibson, R. R., & Canizares, C. R. 2005, ApJ, 631, 733

begincomment Note: This chapter originally appeared as **?**, with co-authors Kevin T.C. Jim, Andrew J. Pickles, Hubert T. Yamada, J. Elon Graves, Alan Stockton, Malcolm J. Northcott, Tony Young, Lennox L. Cowie, Gerard A. Luppino, Robert J. Thornton, Renate Kupke, and Edward Sousa.

Chapter 3

Optical follow-up of X-ray selected Swift clusters using PanSTARRS & MDM data

This chapter has been previously published as "Optical Confirmation of X-ray selected Galaxy clusters from the Swift AGN and Cluster survey with MDM and Pan-STARRS Data (Paper III)", Bhatiani, S., Dai, X. , Griffin, R. , Nugent, J. , Kochanek, C.S, Bregman, J.N., 2022 ApJS, Volume 259 Number 1 arXiv: 2111.09974. It is presented here in its entirety in an updated format.

Abstract

To understand structure formation in the universe and impose stronger constraints on the cluster mass function and cosmological models, it is important to have large galaxy cluster catalogs. The Swift AGN and Cluster Survey is a serendipitous X-ray survey aimed at building a large statistically selected X-ray cluster catalog with 442 cluster candidates in its first release. Our initial SDSS follow-up study confirmed 50% of clusters in the SDSS footprint as $z < 0.5$ clusters. Here, we present further optical follow-up analysis of 248 (out of 442) cluster candidates from the Swift cluster catalog using multi-band imaging from the MDM 2.4m telescope and the Pan-STARRS survey. We report the optical confirmation of 55 clusters with $> 3\sigma$ galaxy overdensities and detectable red sequences in the color-magnitude space. The majority of these confirmed clusters have redshifts z < 0.6. The remaining candidates are potentially higher redshift clusters that are excellent targets for infrared observations. We report the X-ray luminosity and the optical richness for these confirmed clusters. We also discuss the distinction between X-ray and optical observables for the detected and non-detected cluster candidates.

3.1 Introduction

Observational studies of the distribution of galaxies in the universe reveals inhomogeneity and structure on megaparsec and larger scales. Galaxy clusters and groups contain virialized assemblys of galaxies and they are the largest gravitationally bound structures with typical masses ranging from $10^{14} - 10^{15}\ M_{\odot}$. Studying them is significant for understanding the constitution and assembly history of these systems and probing the large-scale structure of the Universe (e.g., Bahcall et al. 1983; Bahcall 1988, 1997; Carlberg et al. 1996; Postman et al. 1986, 1992; Einasto et al. 1997; Borgani et al. 2001; Zehavi et al. 2005). Statistical studies of galaxy clusters impose strong constraints on the cosmological parameters and cosmological models of the growth of structure (Voit 2005; Allen et al. 2011). For example, weak gravitational lensing and X-ray observations provide constraints on cluster masses (Blain et al. 1999; Metcalfe et al. 2003; Smith et al. 2005; Okabe et al. 2010, 2011, 2016; Applegate et al. 2014; Hoekstra 2015). The cluster mass function can then be used to constrain the dark energy equation of state (Munshi et al. 2003; Mantz et al. 2014) and neutrino masses (Carbone et al. 2012). Galaxy clusters also provide a high density environment for studying galaxy formation, evolution and dynamics (Butcher & Oemler 1978; Dressler 1980; Dressler & Gunn 1992; Garilli et al. 1999; Poggianti et al. 1999; Goto et al. 2003; Smith et al. 2005; Postman et al. 2005; Von Der Linden et al. 2007; Maughan et al. 2012; Lauer et al. 2014).

Galaxy clusters can be observed across the electromagnetic spectrum and through gravitational lensing. These emissions correspond to different physical components of the cluster and lead to a variety of cluster detection techniques. The detection of galaxy clusters using optical images was the first method used to build cluster catalogs and developed a statistical understanding of the cluster population (Abell et al. 1958; Zwicky et al. 1961; Abell, Corwin & Olowin 1989). The emergence of wide-field multi-band imaging surveys has led to the development of many cluster finding algorithms including galaxy density mapping (Mazure et al. 2007; Adami et al. 2010), friends-of-friends algorithms (Huchra & Geller 1982; Li et al. 2008; Feng et al. 2016), and Voronoi Tesselation methods (Ebeling & Weidenmann 1993; Ramella et al. 2001; Lopes et al. 2004). One common optical detection method uses the tight color-magnitude relation of the early-type galaxies in the clusters to identify clusters (Gladders & Yee 2000, 2005; Nilo Castellon et al. 2014). Several cluster finders based on the cluster red sequence method have yielded large cluster catalogs within the SDSS and Dark Energy Survey, such as maxBCG (Koester et al. 2007), GMBCG (Hao et al. 2010), AMF (Szabo et al. 2011; Banerjee et al. 2018), WHL2012 (Wen et al. 2012), and redMaPPer (Rykoff et al. 2014, 2016). However, optical cluster finding algorithms suffer from projection effects as galaxy clusters are three dimensional objects that are projected on a 2D sky, especially at higher redshifts as the contamination from the foreground galaxies increases.

The intracluster medium (ICM) of galaxy clusters is hot plasma that produces X-ray emission by the thermal bremsstrahlung process (Felten et al. 1966; Mitchell et al. 1976; Bahcall & Sarazin 1977; Kravstov & Borgani 2012). As bright extended sources, clusters are easily identified in X-ray surveys and they stand out from the background because the emission is proportional to the square of the electron number density (Voit 2005; Ebeling et al. 1998). X-ray selection also characterises the hot intracluster gas component that accounts for the majority of the baryonic mass of the cluster (Cavaliere & Fusco-Femiano 1976; Allen et al. 2002) yielding cluster samples with well-characterized cluster masses. Studies have suggested that the X-ray luminosity and mass correlation is tighter than that between optical richness and mass relation so that X-ray methods provide more accurate measurements of cluster masses (Böhringer et al. 2000; Voit 2005). A slew of X-ray cluster surveys with varying energy range, depth, and area have been conducted including the Northern ROSAT All-Sky Survey (NORAS, Böhringer et al. 2000), the ROSAT-ESO Flux Limited X-ray Cluster Survey (REFLEX, Böhringer et al. 2001), the Massive Cluster Survey (MACS, Ebeling et al. 2001), and the Highest X-ray flux Galaxy Cluster Sample (HIFLUGCS, Reiprich et al. 2002). More recent surveys are based on XMM-Newton and Chandra observations and include the XMM-Large Scale Structure survey (XLSS, Pacaud et al. 2007), the Chandra Multiwavelength Project Serendipitous Galaxy cluster survey (ChaMP, Kim et al. 2004; Green et al. 2004; Barkhouse at al. 2006), and the 3XMM/SDSS Stripe 82 galaxy cluster survey (Takey et al. 2016). These X-ray surveys have uncovered a sizable sample of galaxy clusters extending up to photometric redshifts of 1.9 (Basilakos et al. 2004; Popesso et al. 2004;

Piffaretti et al. 2011; Mehrtens et al. 2012; Clerc et al. 2012; Takey et al. 2011, 2013, 2014). With the advent of the next generation of all-sky X-ray survey, eRosita, we can expect to detect several hundred thousand clusters (Pillepich et al. 2012). The hot X-ray emitting gas also introduces Sunyaev-Zel'dovich (S-Z; Sunyaev & Zeldovich 1972, 1980; Carlstrom et al. 2002) distortions in the microwave background that can be used to identify clusters (McInnes et al. 2009; Brodwin et al. 2010; Hincks et al. 2010; Vanderlinde et al. 2010; Foley et al. 2011; Planck Collaboration 2011b; Menanteau et al. 2012; Stalder et al. 2012; Hasselfield et al. 2013). Since the S-Z effect is a scattering effect that is based on absorption of energy, it has the advantage that the signal amplitude is nearly independent of distance although the optical survey resolution does depend on redshift.

The Swift AGN and cluster survey (SACS) is a serendipitous soft X-ray survey (Dai et al. 2015). It is a wide-field survey spanning an area of 125 square degrees in the sky with a median flux limit of 10^{-15} erg cm^{-2} s^{-1}. SACS targets Gamma-ray burst (GRB) fields that are randomly distributed across the sky and have no correlation with known X-ray sources. Thus, SACS is a medium deep, broad-field, serendipitous X-ray survey that is ideally suited for detecting galaxy clusters and AGNs at intermediate redshifts. The first release of the survey yielded a total of 442 cluster candidates (Dai et al. 2015), which require a multiwavelength investigation to establish their properties. Despite the many advantages of X-ray surveys over optical surveys, the X-ray detection method pose some limitations. While X-ray probes favor massive systems with deep potential wells, the low mass and gas-poor clusters remain hidden and surface brightness dimming makes it difficult to detect high redshift clusters. The biggest limitation, however, is that optical observations are almost always required to determine the redshifts. Approximately 25 square degrees of the SACS area overlapped with the SDSS DR8 survey (Aihara et al. 2011) so the initial optical follow-up was conducted using the SDSS archival data (Griffin et al. 2016). Out of the 442 SACS cluster candidates, 209 fell in the footprint of SDSS DR8 and 103 were confirmed as galaxy overdensities with a red sequence methods that yielded a photometric redshift in the redshift range of $z < 0.8$, where the cluster sample is complete below $z < 0.3$ and 40% and 25% complete at $z = 0.5$ and $z = 0.8$. The redshift distribution of the SDSS confirmed clusters is consistent with the theoretical predictions for SACS given its X-ray flux limits and models for the cluster mass function (Tinker et al. 2008). Griffin et al. (2016) found that about 30% of the cluster candidates that fell in the SDSS regions were low redshift clusters ($z < 0.5$), 14% were recognized as $0.5 < z < 0.8$ clusters, and the remaining unconfirmed candidates likely have redshifts $z \gtrsim 0.3$ (Griffin et al. 2016).

We have now performed optical follow-up observations with the MDM 2.4m Hiltner, KPNO 4m Mayall, and CTIO 4m Blanco telescopes, and used public Pan-STARRS and DES survey data to further study the *Swift* cluster candidates. These observations are both deeper images of the SDSS regions and expansions to cover the non-SDSS regions. In this chapter, we present results from MDM/Hiltner and Pan-STARRS (north of $-30°$ targets). The layout of the chapter is as follows. Section 3.2 describes the optical follow-up data used for this work. In Section 3.3, I discuss how we verify the *Swift* cluster candidates using the optical overdensity/red sequence method. In Section 3.4, I end with the conclusions and a discussion of our results. Cosmological parameters of $\Omega_M = 0.27$, $\Omega_\Lambda = 0.73$, and $H_0 = 70$ km s^{-1} Mpc^{-1} throughout the chapter.

3.2 Optical follow-up Data

We primarily used MDM/Hiltner and Pan-STARRS data as the data obtained by the KPNO/Mayall was affected by sub-optimal observing conditions. While we observed 66 northern the *Swift* cluster candidates in 39 fields using the 4m Mayall, the observing conditions were non-photometric/partially cloudy, and we were unable to attain the expected photometric depths. Compared with the corresponding sources in Pan-STARRS 3π survey catalog, the magnitude limits of our Mayall images are 1–2 mag brighter. Therefore, we used the 3π catalog in the subsequent analysis. Pan-STARRS 1 (PS1) encompasses several surveys, two of which are of relevance here: the Pan-STARRS 3π Steridian survey (DR1, Chambers et al. (2016); DR2, Flewelling et al. (2018)), covers 30,000 square degrees of the sky north of -30 declination, and the Medium deep survey consisting of nightly observations of ten smaller fields distributed across the sky. Although, the 3π survey is a relatively shallower survey with 5σ depths of 23.3, 23.2, 23.1, 22.3, 21.3 in g, r, i, z, y, respectively, it's wide area means it includes most of the Swift clusters. We downloaded DR1 and DR2 source catalogs for 11 arcmins regions around the *Swift* cluster centers.

We also observed 53 *Swift* cluster candidates with the 2.4m Hiltner Telescope at the MDM observatory with OSMOS and either the blue or red 4K detector between 2011 to 2013. These cluster candidates are all in SDSS, but unconfirmed in the SDSS archival analysis of Griffin et al. (2016). The images have a field of view of 11.5^2 arcminutes on each side, and the seeing range between 1–2.5 arcsecs. For each target, we observe all the fields in the g, r, i filters and a fraction in z with 3–4 dithered images per filter. Calibration data, including bias, sky or dome flats, were also obtained for each night of observation. We first performed overscan, bias, cross-talk, and flat-field corrections, then created super-flat images for fringing in the longer wavelength i and z images and updated the astrometry of the images using the USNO B1.0 catalog. We used SWarp tool (Bertin et al. 2002) to median combine the dithered images in each band, and generated a panchromatic image by combining all the images for each field. Source detection and flux measurement was performed with SExtractor (Bertin & Arnouts 1996) in the dual image mode using the panchromatic image for detection and the band specific image for the fluxes. Since all these MDM fields are in SDSS, the photometry calibration is performed relative to SDSS magnitudes.

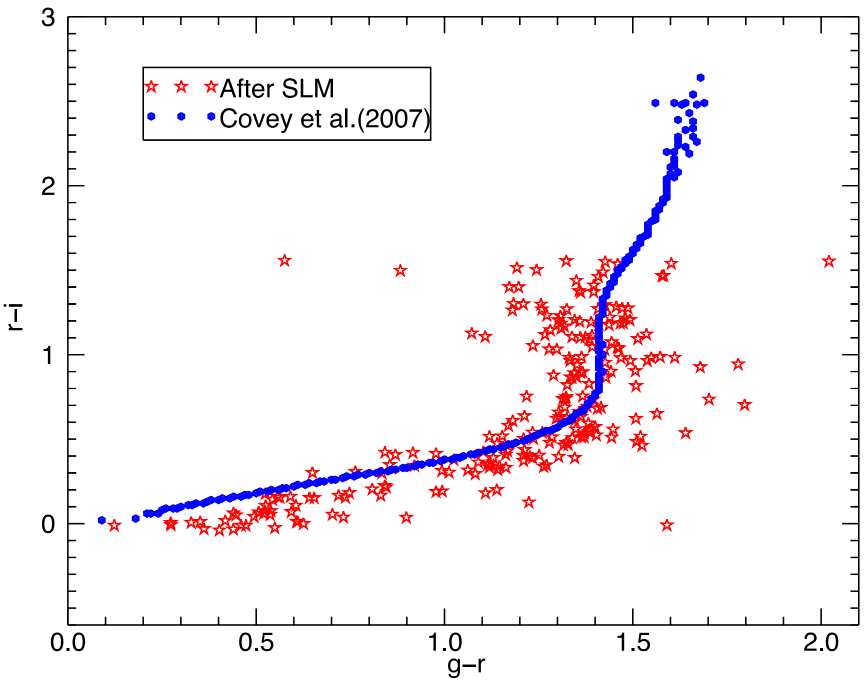

Figure 3.1 An illustration of the stellar locus matching technique employed to determine photometric color corrections for the MDM data. The standard stellar locus from Covey et al. (2007) is represented by the blue curve. The data points in red are the photometrically calibrated colors for stars in an MDM field.

3.3 Optical Cluster Overdensity Analysis

3.3.1 Stellar locus correction

Accurate measurements of photometric redshifts require robust photometric calibrations to accurately determine the photometric colors. We calibrate the colors using stellar locus regression (SLR, High et al. 2009; Ivezic et al. 2007; Desai et al. 2012; Kelly et al. 2014) for the MDM data. This technique is based on the known colors of the stellar main sequence. The Pan-STARRS colors have already been corrected based on this method (High et al. 2009), and we have verified this from our independent analysis as well. We measure the stellar locus using the standard high-quality superclean sample of ∼500,000 stellar sources from Covey et al. (2007) jointly observed by the SDSS and Two Micron All Sky Survey (2MASS) surveys. The standard stellar locus exhibits a prominent kink feature at $g - r \sim 1.4$ and $r - i \sim 0.7$ in the $(g - r,\, r - i)$ color plane, which we use as the main feature to perform calibration. The red side of the stellar locus is dominated by M dwarfs (Finlator et al. 2000; Covey et al. 2007; Juric et al. 2008; High et al. 2009), which are intrinsically dimmer compared to the more luminous stars on the blue $r - i < 0.7$ side of the stellar locus. Hence, to measure the entire locus including the kink, it was imperative to maximize the number of stars on each branch of the stellar locus. The stars used to identify the stellar locus were selected based on SExtractor's star/galaxy classifier parameter and a magnitude uncertainty of less than 2 mag to include enough faint stars on the red side of the kink for this analysis. Although the individual measurement uncertainty is large, the mean trend can be constrained much better with the large sample of stars. We bin the stars by their $r - i$ color and the median of the $g - r$ color for each bin. Next, we apply an initial sigma clip followed by a median smoothing of the two colors such that each point in the color-color space is replaced by the median in the closest windows of points. A typical field locus spans a color range of approximately 2 magnitudes and the typical color bin width considered is 0.02 magnitudes. We then fit a polynomial to the sequence of colors, identify the kink, and shift the colors to align with the calibration sequence.

3.3.2 Redshift estimation using colors

To find clusters we search for galaxy overdensities in three-dimensional space using both galaxy positions and the photometric colors or redshifts. We use a method that exploits the fact that the cluster galaxy population and the background have a bimodal color distribution (Hao et al. 2010). We select galaxies by imposing cuts on the star/galaxy classifier and magnitude uncertainties. For the MDM fields, we required SExtractor parameters of $CLASS\_STAR < 0.8$ and $MAG\_AUTO_{err} < 0.33$ ($S/N = 3$), while for Pan-STARRS fields we required $ipsf - ikron > 0.05$ and $ikron_{err} < 0.3$. For each cluster candidate, galaxies were chosen within a source region of typical cluster size ranging from 1–2 Mpc. For the photometric depths of our data, we are primarily sensitive to $z \lesssim 0.4$, so the clusters over 2–3 arcmins in size. Hence we choose a source radius of $3'$, and the background annulus from $7'$ to $10'$, both centered on the X-ray centroid position. The cluster candidates in the MDM data set are expected to be higher redshift clusters, so we used a source radius of $1.5'$, and a background annulus from $5'$ to $10'$, excluding regions within $5'$ from other cluster candidates in the field. We examine the color-distribution of these cluster candidates to identify galaxy overdensities and determine the significance of any detection. In order to perform a comparative study of the galaxy color distribution of the cluster and

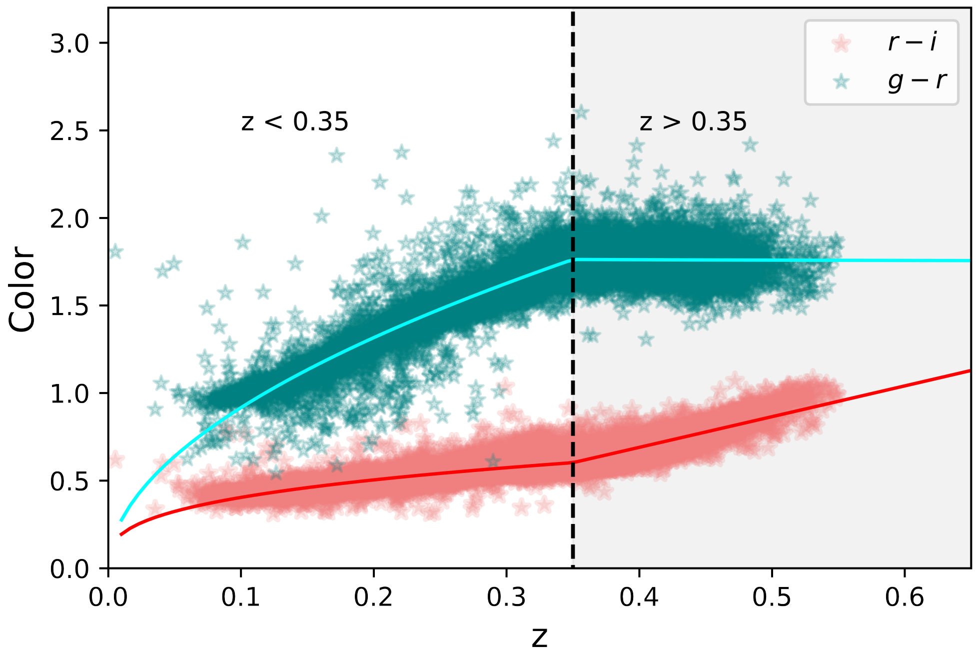

Figure 3.2 Red sequence color as a function of the spectroscopic redshift for the galaxy clusters in the SDSS from the GMBCG catalog (Hao et al. 2010). A broken power law is fitted to $g - r$ (in blue) and $r - i$ (in red) with a break at $z = 0.35$ (dashed black line).

background, the background counts per bin were normalized to the source region using the ratio of the source to the background area. The background is used to estimate the contamination from interloping galaxies within the cluster region. To determine the over-density per bin, we compare the source count per color bin with the corresponding normalized background count. Assuming a Poisson distribution, we estimate the standard deviation of the over-dense bins as :

$$\sigma = \sqrt{N_{src} + N_{bkg} * \left(\frac{A_{src}}{A_{bkg}}\right)^2} \tag{3.1}$$

where N_{src} is the source count per bin, N_{bkg} is the background count per bin and A_{src}/A_{bkg} is the ratio of the areas of the source and background regions. The significance of the overdensity is calculated per color bin and the maximally overdense bin is identified. To accurately estimate the over-density peak, we use bin sizes of 0.05, 0.1 and 0.15 for the color distribution, with and without a half shift in the bin center. Once we determine the maximally overdense bin, our algorithm incorporates other neighbouring bins with excess galaxy counts to determine the peak of the overdensity. The criterion for including the neighbouring bins is set as $N_{src}/N_{bkg} > 2$. The bins that satisfy the aformentioned criteria are combined together to determine the mean color of the red sequence and the color error is given by the standard deviation. The significance of detection is calculated using the total source and background counts for all excess bins. The color of the cluster is converted to redshift using the color-redshift relation found by fitting a broken power-law to the spectroscopic data for $55,000$ rich clusters from the GMBCG catalog (Hao et al. 2010), spanning a redshift range of $0.1 < z < 0.55$ (See Figure 3.2). The broken power laws for $g - r$ and $r - i$ display a break-point at $z = 0.35$. For photometric redshift estimation, $g - r$ colors have been used to identify clusters with $z < 0.35$ due to the flatness of the relation at higher redshifts. While r−i colors shows a relatively steeper trend in both redshift intervals, we have predominantly used the $r - i$ colors for the redshift range $0.35 < z < 0.7$. Because of the flat relation of colors as a function of redshift for $i - z$ and $z - y$, we have used the redsequence in these color bands only for detection purposes and not for redshift detemination. The uncertainities in the color are converted to redshift using the propogation of errors and combined in quadrature with the scatter in the color-redshift relation. The redshift estimates using the red sequence method are reported in Table 3.1.

3.3.3 Redshift estimation using EAZY photo-zs

Apart from looking for clustering in the color space, we have also run a similar analysis to locate overdensities in redshift space. This method requires photo-z estimation of the galaxies, which has been conducted using the photo-z estimator EAZY (Brammer et al. 2008). EAZY employs a spectral energy distribution (SED) fitting technique to compute the photometric redshifts of galaxies using broadband photometry, and provides reasonably accurate photo-z estimates without the need for spectroscopy. The accuracy of the photo-z estimates depend on a number of factors, one of them being the availability of multiband imaging data in 5 or more filters, therefore the photo-z estimates were obtained only for the Pan-STARRS data which provides imaging in g, r, i, z and y band. The photo-z redshift distribution of the source and the background galaxies yield the mean photometric redshift (See Figure 3.3) of the cluster and the detection significance. For the redshift, we have used the same algorithm as used in color space to determine the mean redshift and the significance of the detection. An

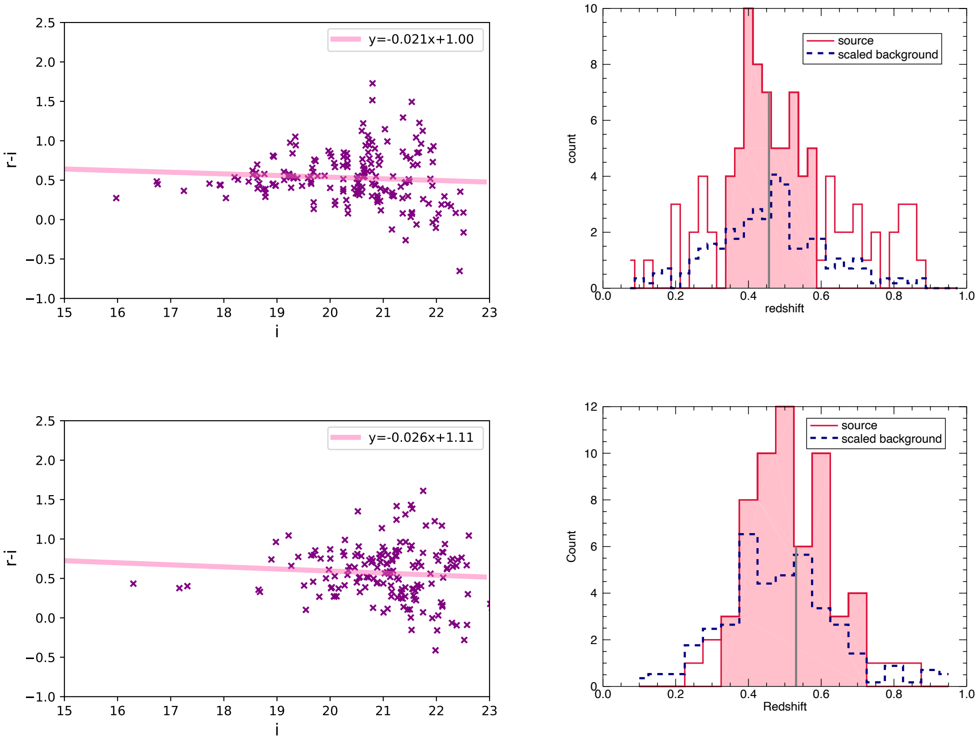

Figure 3.3 The color-magnitude diagram (Left) and the photometric redshift distribution (Right) for galaxies within 1.5' of the cluster X-ray centroid for Swift sources SWCL J002729.2$-$232626 (Top) and SWCL J021007.7$-$270414 (Bottom). The scaled background galaxy distribution is represented by the navy dashed line. SWCL J021007.7 $-$ 270414 (Top) is optically verified with a detection significance of 5.84σ (Top right) and redshift of 0.45. SWCL J002729.2 $-$ 232626 detected at a redshift of 0.54 and detection significance of 3.35σ (Bottom right). The redshift bins with significant overdensities are shaded in red and the mean redshift is shown by a gray vertical line.

average of the photo-z errors for the galaxies are combined in quadrature with the standard deviation of the mean redshift to find the uncertanities. Owing to the uncertainties in the redshift measurements, some clusters with an overdensity in color space may not present a counterpart detection in the redshift space, therefore we have reported the candidates that satisfy the detection criteria for either one of the cluster-finding methods. We require a $> 3\sigma$ overdensity for a detection, however, if both give a $> 3\sigma$ detection, the highest detection significance among the two is considered and the corresponding redshift estimates are used. In Table 3.1, we lists 55 Swift clusters that are confirmed with a detection above 3σ. We have reported the redshift estimates using the red sequence and the photo-z method. In Figure 3.3, we show the color magnitude diagram and galaxy redshift distribution for two detected SACS clusters.

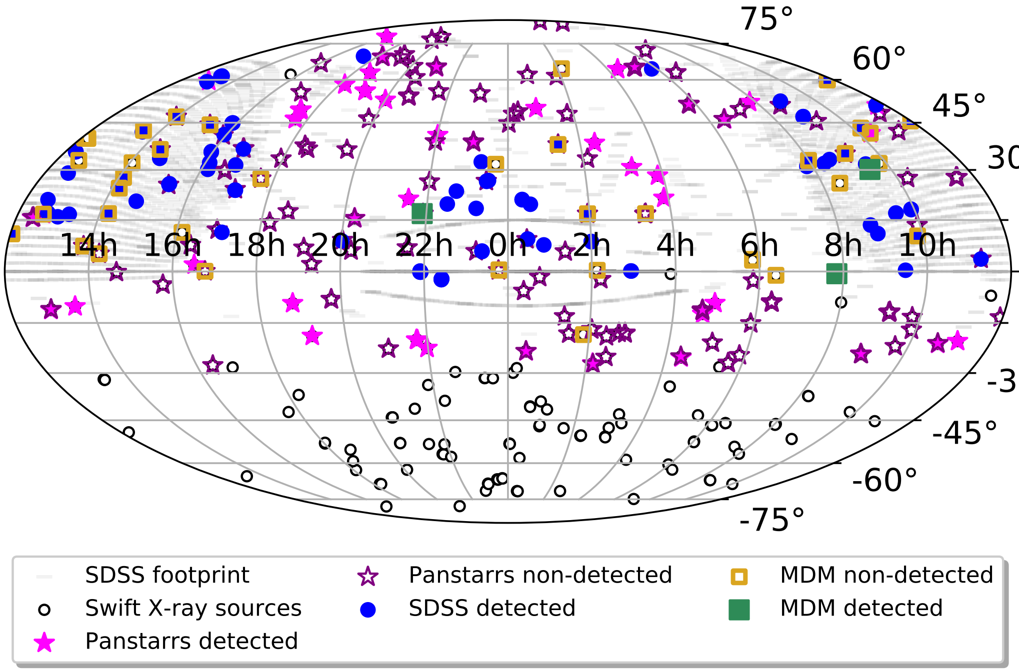

Figure 3.4 Equatorial coordinate distribution of the 442 SACS cluster candidates. The black open circles are those without follow-up data from this paper. The SDSS spectroscopic plates for the DR8 are shown in gray and the SDSS detections (Griffin et al. 2016) are displayed as blue filled circles. The Swift cluster candidates falling within the SDSS footprint and followed up with deeper optical observations with MDM are shown as squares, with the detected clusters as filled green and undetected clusters as open golden symbols. The Swift cluster candidates falling outside the SDSS footprint analyzed using Pan-STARRS data are marked by filled pink and open purple stars for detections and non-detections respectively.

Table 3.1. Swift Cluster Survey: $> 3\sigma$ optical confirmations with MDM & Pan-STARRS

Swift name	RA (deg)	Dec (deg)	Detection significance	z (Color)	σ_z	z (EAZY)	σ_z	λ	N_o	σ_λ	Lx (ergs/s)	σ_{L_X} (ergs/s)
SWCL J051046.0+644429	77.69	64.74	3.79	0.17	0.042	0.44	0.129	....	6.06	....	4.30e+42	4.02e+41
SWCL J104158.8−211124	160.49	−21.19	3.68	0.18	0.173	0.45	0.100	14.71	14.12	3.757	3.23e+43	4.05e+42
SWCL J183744.0+624135	279.43	62.69	4.74	0.20	0.037	0.44	0.112	9.58	14.41	3.796	7.25e+43	1.45e+43
SWCL J054653.1+510908	86.72	51.15	4.76	0.20	0.173	0.42	0.096	12.83	13.47	3.670	5.21e+43	9.92e+42
SWCL J133437.4−100927	203.66	−10.16	3.27	....	....	0.79	0.486	117.97	2.12	1.455	1.02e+45	8.74e+43
SWCL J062915.2+460619	97.31	46.11	5.60	0.17	0.036	0.40	0.097	15.88	25.29	5.029	2.29e+45	8.01e+43
SWCL J181053.5+581524	272.72	58.26	5.52	0.36	0.036	0.39	0.079	7.31	12.82	3.581	2.23e+44	2.32e+43
SWCL J155644.8+782352	239.19	78.40	3.56	....	....	0.40	0.121	....	6.12	....	1.19e+43	2.30e+42
SWCL J173719.2+461253	264.33	46.21	6.53	0.40	0.038	0.55	0.099	64.16	41.59	6.449	9.21e+43	6.45e+42
SWCL J173721.7+461832	264.34	46.31	6.56	0.49	0.039	0.66	0.124	123.15	17.82	4.222	3.47e+44	1.49e+43
SWCL J035130.3+281517	57.88	28.25	4.02	0.06	0.035	0.40	0.098	....	8.94	....	5.28e+41	8.58e+40
SWCL J002729.2−232626	6.87	−23.44	3.97	0.44	0.035	0.52	0.108	5.32	8.00	2.828	1.31e+44	1.10e+43
SWCL J005233.8+495407	13.14	49.90	3.51	0.48	0.035	0.40	0.104	....	2.53	....	7.14e+44	3.47e+43
SWCL J021007.7−270414	32.53	−27.07	7.13	0.42	0.037	0.52	0.106	76.62	44.35	6.660	2.96e+43	2.33e+42
SWCL J022409.4+382635	36.04	38.44	4.62	....	....	0.74	0.222	....	....	....	....	....
SWCL J031430.6+305035	48.63	30.84	3.07	0.62	0.038	....	....	96.96	3.18	1.782	6.59e+43	9.03e+42
SWCL J035312.2+213345	58.30	21.56	9.17	0.17	0.040	0.48	0.103	55.38	73.41	8.568	1.14e+44	9.08e+42
SWCL J042338.6−251617	65.91	−25.27	3.07	0.26	0.040	0.53	0.144	....	6.53	....	3.48e+42	6.47e+41
SWCL J042422.3+640633	66.09	64.11	3.30	0.55	0.041	0.53	0.073	170.64	3.94	1.985	5.66e+43	1.16e+43
SWCL J044123.7−111550	70.35	−11.26	4.05	0.55	0.036	0.51	0.100	16.35	12.59	3.548	3.17e+43	5.16e+42
SWCL J044144.6−111534	70.44	−11.26	3.05	....	....	....	....	....	....	....	....	....
SWCL J044237.2−122251	70.66	−12.38	3.74	0.11	0.173	0.44	0.106	....	12.06	....	1.39e+42	2.90e+41
SWCL J045832.6−091111	74.64	−9.19	5.83	0.49	0.037	0.28	0.132	16.81	6.53	2.555	2.75e+44	1.80e+43
SWCL J074755.5+515852	116.98	51.98	5.01	0.51	0.036	0.68	0.088	25.64	5.41	2.326	1.50e+44	2.59e+43
SWCL J085416.4−240703	133.57	−24.12	3.08	0.36	0.037	0.42	0.116	7.51	10.71	3.272	7.65e+44	1.42e+43
SWCL J102036.8+413227	155.15	41.54	3.05	0.36	0.036	0.42	0.229	....	5.18	....	1.91e+43	3.42e+42
SWCL J110932.9−202209	167.39	−20.37	3.34	0.05	0.036	0.73	0.368	10.64	6.35	2.521	1.03e+44	1.48e+43
SWCL J114332.8+504856	175.89	50.82	5.43	0.35	0.036	0.42	0.101	5.55	8.94	2.990	1.43e+43	2.66e+42
SWCL J122327.6+153927	185.86	15.66	4.75	0.29	0.173	0.45	0.123	5.27	7.53	2.744	3.26e+43	5.76e+42
SWCL J123717.7+164353	189.32	16.73	3.07	0.13	0.173	....	....	....	4.06	....	6.40e+42	2.95e+41
SWCL J125814.0−111333	194.56	−11.23	3.54	0.40	0.036	0.39	0.077	4.85	8.53	2.921	1.62e+43	3.09e+42
SWCL J130345.6+593437	195.94	59.58	4.44	0.23	0.039	0.42	0.092	5.04	7.82	2.797	1.49e+43	2.43e+42
SWCL J163054.8+015924	247.73	1.99	7.21	....	....	....	....	....	....	....	....	....
SWCL J173302.3+490920	263.26	49.16	4.58	0.43	0.036	0.45	0.120	4.12	6.35	2.521	1.63e+43	2.95e+42
SWCL J173316.3+492211	263.32	49.37	3.08	0.47	0.038	....	....	....	....	....	3.01e+43	4.53e+42
SWCL J181628.8+691131	274.12	69.19	6.63	0.14	0.038	0.45	0.116	13.79	19.76	4.446	2.77e+44	1.54e+43
SWCL J184929.4−091328	282.37	−9.22	4.68	0.23	0.037	0.40	0.131	....	22.24	....	1.07e+44	1.71e+43
SWCL J190614.5+555534	286.56	55.93	8.31	0.27	0.043	0.49	0.097	69.37	64.59	8.037	5.36e+44	2.78e+43
SWCL J190620.9+555237	286.59	55.88	4.20	0.36	0.035	0.48	0.101	24.67	14.71	3.835	1.89e+44	2.04e+43
SWCL J190633.9+560146	286.64	56.03	3.92	0.47	0.036	....	....	....	4.35	....	2.61e+43	5.50e+42
SWCL J191020.9−184932	287.59	−18.83	4.02	0.08	0.037	0.42	0.150	....	13.76	....	3.70e+42	6.51e+41
SWCL J200005.7+524438	300.02	52.74	3.32	....	....	....	....	....	....	....	....	....
SWCL J201549.0+153231	303.95	15.54	3.26	0.04	0.036	0.40	0.165	....	23.47	....	1.94e+41	2.47e+40
SWCL J210442.9+644555	316.18	64.77	3.91	0.52	0.036	0.52	0.092	68.87	6.18	2.485	3.02e+43	3.94e+42
SWCL J213130.8+211616	322.88	21.27	3.05	0.59	0.037	....	....	....	....	....	1.78e+44	1.78e+43
SWCL J214405.7−195813	326.02	−19.97	7.77	0.49	0.038	0.60	0.135	91.90	33.00	5.745	4.55e+43	6.42e+42
SWCL J214409.9−195600	326.04	−19.93	3.34	0.72	0.036	0.82	0.337	....	9.12	....	3.84e+45	8.45e+43
SWCL J214515.6−195944	326.32	−20.00	3.91	0.04	0.036	0.50	0.144	....	8.00	....	6.85e+42	1.56e+41
SWCL J215507.7+164725	328.78	16.79	3.50	0.11	0.173	0.72	0.165	....	10.88	....	5.10e+43	4.42e+42
SWCL J215831.9−222439	329.63	−22.41	6.86	0.38	0.037	0.45	0.106	15.84	22.82	4.777	1.50e+43	2.94e+42
SWCL J220026.5+405625	330.11	40.94	3.18	0.25	0.173	....	....	....	4.94	....	3.22e+43	1.73e+42
SWCL J230207.3+384751	345.53	38.80	4.94	0.59	0.037	0.37	0.129	6.48	12.47	3.531	5.81e+43	5.43e+42
SWCL J092642.2+300835	141.68	30.14	3.01	0.90	0.045	....	....	128.30	9.40	3.066	8.39e+43	1.35e+43
SWCL J075036.6−003838	117.65	−0.64	3.43	0.09	0.036	....	....	....	10.16	....	7.38e+43	5.21e+42
SWCL J215357.0+165313	328.49	16.89	4.28	0.43	0.036	....	....	....	12.76	....	2.74e+44	1.22e+43

3.3.4 X-ray luminosity and Optical richness

We also report the X-ray luminosity and the optical richness for all the detected clusters in the Table 3.1. A detailed study of the X-ray and optical properties and their correlations for the SACS clusters will be studied in the subsequent paper. For the calculation of X-ray bolometric luminosities, we have utilized an X-ray spectral fitting program XSPEC (Arnaud et al. 1996). We used the flux estimates for the SACS clusters from Dai et al. (2015) and converted the flux to luminosity by assuming a multiplicative component model, $wabs * apec$. The plasma temperature was fixed at 5 keV and the abundance is assumed to be 0.3 Solar. The Galactic column density was fixed for each cluster position using the n_H command in XSPEC. We use the photometric redshifts from our present analysis. The uncertainties in L_X only include the uncertainties in the X-ray photon counts and not the model parameters. Since X-ray luminosity serves as a mass proxy, we have used the M_{200}–L_X relation (Reiprich et al. 2002) to estimate the mass within the radius of R_{200} at which the density of the cluster is 200 times the critical density of the Universe.

The optical richness of the cluster, λ, is a measure of the number of galaxies in the system. To estimate λ, we first measure the observed galaxy counts, N_o, which is the number of galaxies above the estimated background that fall within the one standard deviation of the mean redshift of the cluster. The optical richness, λ, is the number of galaxies with luminosities larger than L_* or magnitude brighter than M_*. We assume a Schechter luminosity function,

$$\lambda = \int_{L_*}^{\infty} \phi_* \left(\frac{L}{L_*}\right)^{\alpha} e^{-\frac{L}{L_*}}\, dL \tag{3.2}$$

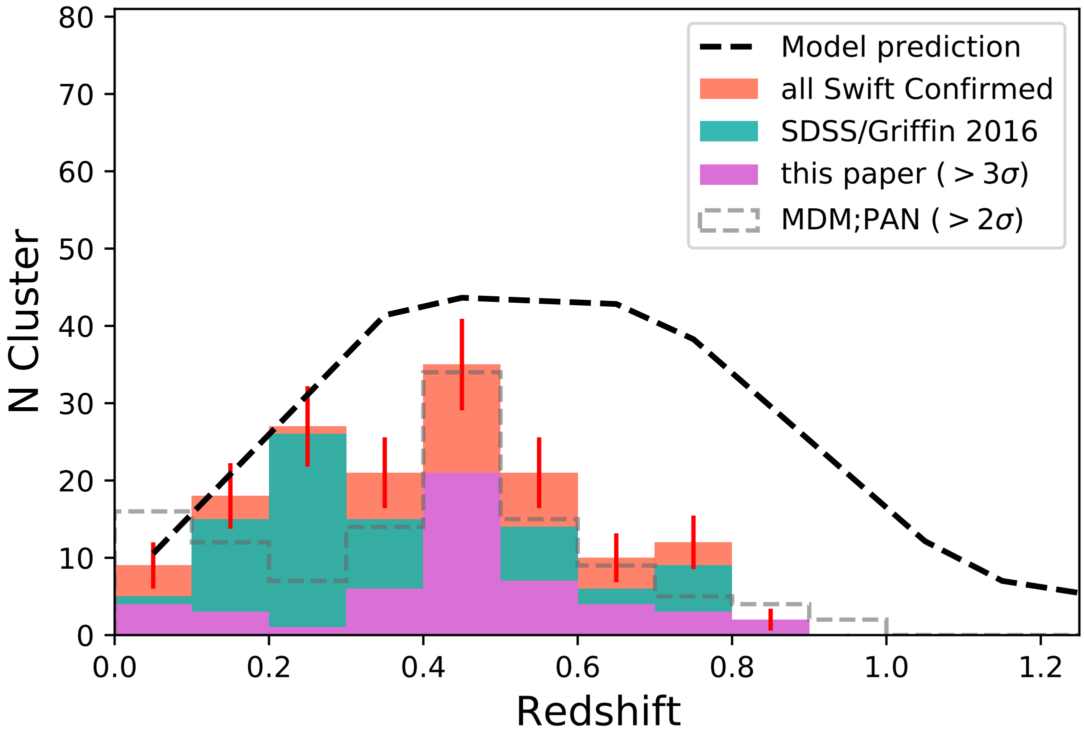

Figure 3.5 Redshift distribution of the optically confirmed SACS clusters detected at a significance $> 3\sigma$. The green histogram is the z distribution of the SDSS confirmed clusters from (Griffin et al. 2016). The pink histogram is the redshift distribution of the clusters optically detected at $> 3\sigma$ in this paper using MDM and Pan-STARRS, and the peach histogram is the distribution of all optically confirmed clusters in the survey to date. The gray dashed histogram shows the distribution of all $> 2\sigma$ SACS candidates in MDM and Pan-STARRS. The black dashed line shows the predicted distribution for the Swift AGN and cluster survey using the model of Tinker et al. (2008).

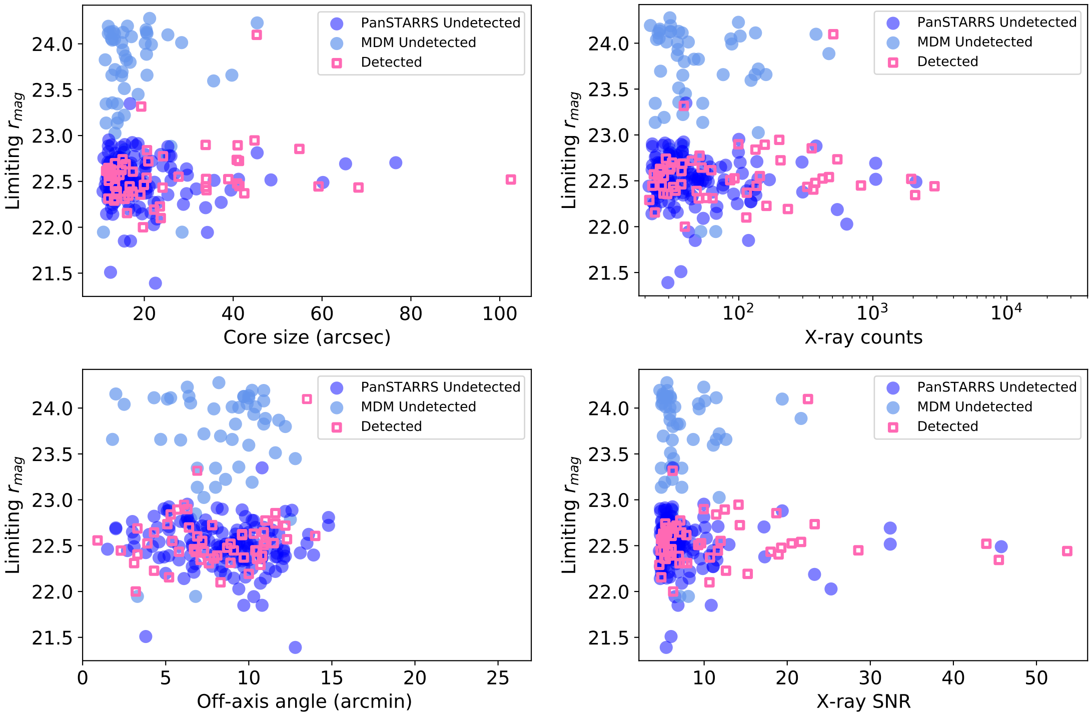

Figure 3.6 Distribution of the candidates examined here in limiting r-band magnitude on X-ray core-size (top left), X-ray counts (top right), off-axis angle (lower left) and X-ray SNR (lower right). The candidates are coded as shown in the panels.

where,

$$\frac{L}{L_*} = 10^{0.4(M_* \ - \ M)} \tag{3.3}$$

We have considered a magnitude break at $M_*(0) = -21.34$ mag and slope $\alpha = -1.07$, adopted from the results of (Bell et al. 2003) for SDSS-r band. We assume that the break luminosity evolves as

$$M_*(z) = M_*(0) - \beta z \tag{3.4}$$

Where $\beta = 1.2$ (Dai et al. 2009). In order to normalize the Schechter luminosity function, we determine the absolute magnitude limits for each cluster using the apparent r-band limiting magnitudes for each field. For the calculations of the absolute magnitude limits, we correct for galactic dust extinction for each cluster centroid position using the NED online calculator for Galactic Reddening and Extinction. We also apply the K-corrections determined using the low resolution spectral templates for elliptical galaxies from Assef et al. (2010). The normalization constant for the Schechter luminosity function, ϕ_* , is calculated using the absolute magnitude limit and the background subtracted source counts, N_o. Considering N_o is found using an apparent radius of $3'$, we make a correction for λ assuming an aperture radius of 1.0 Mpc. We adopt an NFW density profile (Navarro et al. 1995) to calculate the correction factor, which is the ratio of the density within a projected radius of 1 Mpc $\rho(r < R1)$ to the density within the observed radius $\rho(r < R_{obs})$. Here, R_{obs} is the angular diameter distance in Mpc corresponding to the $3'$ of the source region. We estimated the NFW scale radius r_s using the L_X – M_{200} and M_{200}– c_{200} relations from Reiprich et al. (2002) and Ettori et al. (2010). The uncertainty in λ heavily depends on the uncertainties in the background subtracted number counts, which is a given as the Poisson error $\sqrt{N_o}$. For several cases with redshifts < 0.1, the optical richness estimates are severely underestimated due to the missing galaxies because of the poor image quality of the observations. On the other hand, for higher redshifts $z > 0.5$, we see that optical richness is grossly overestimated, which has been corrected by setting a magnitude cut-off at $M_* - 1.5\ mag$. We have found that the changes in the magnitude limits have a systematic effect on the richness estimates as we traverse from the fainter to the brighter end of the luminosity function. The observed galaxy counts and the optical richness estimates are presented in Table 3.1, and we have not reported the values for under estimated clusters with $\lambda < 4$.

3.4 Chapter Results & Discussion

This chapter contributes to the detection of optical counterparts and estimation of redshifts for the galaxy clusters within the SACS X-ray survey. Griffin et al. (2016) identified 104 of the SACS clusters using SDSS DR8. Here we identify another 55 clusters North of declination $\delta = -30^\circ$ using MDM and PAN-STARRS data. The next chapter will cover $\delta < -30^\circ$ using CTIO and DES data. All the confirmations to date are illustrated in Figure 3.4. The confirmed clusters from this work with $> 3\sigma$ overdensities extend up to $z \sim 1$ with the majority of detections ranging within the redshift of $0.3 - 0.6$. Figure 3.5 shows the redshift distribution of all the optically confirmed SACS clusters detected at a 3σ significance threshold. We also show the theoretical expectations derived using Tinker et al. (2008) model for the mass function of dark matter halos and their redshift evolution. The model assumes flat ΛCDM cosmology with halo masses in the range $10^{14}h^{-1}M_\odot \leq M \leq 10^{15}h^{-1}M_\odot$. For this work, the model predictions are calculated assuming a slight change in cosmology with parameters: $\Omega_m = 0.25$, $\sigma_8 = 0.9$, $h = 0.72$, and $\Delta = 2000$ and masses ranging from $10^{14}h^{-1}M_\odot$ to $10^{15}h^{-1}M_\odot$. We have also taken into consideration the flux limit and the area of the Swift survey. This model provides a reasonable estimate for the expected distribution and allows us to test the completeness of the catalog. In Figure 3.5, we compare the observed distribution with the model predictions.

We find that the $> 3\sigma$ overdensity sample is consistent with the theoretical redshift distribution and the SACS survey is complete up to $z \sim 0.3$ and is nearly 80% complete upto $z \sim 0.5$. The number of detections show a slight increase up to $z \sim 0.4$, which is followed by a significant jump at $z \sim 0.45$, and then a slow decline to as far as $z \sim 0.9$. The $> 2\sigma$ overdensity sample for this work is sizable and the redshift distribution of these cluster candidates is consistent with the model prediction (See Figure 3.5). However, to test the robustness of our method and calibrate the detection significance, we ran our analysis on a sample of 100 random locations in the SDSS footprint. We ensured that these random locations were far removed from any known clusters within SDSS by comparing against the GMBCG – DR7 (Hao et al. 2010), SACS – DR8 (Griffin et al. 2016), redMaPPer – DR8 (Rykoff et al. 2014) catalogs. We found that a fair fraction of random sources displayed a $> 2\sigma$ significance and so for the sake of robustness we have used a 3σ detection threshold. Comparing the redshift distribution from this chapter with the earlier Swift paper (Griffin et al. 2016), we find that SDSS distribution peaks at $z \sim 0.3$ while the MDM/Pan-STARRS distribution shows a peak at $z \sim 0.45$, which has enhanced the overall number count in the redshift $0.4 - 0.6$ range. The SDSS distribution showed a redshift tail $0.6 < z < 0.8$, which is also observed in the MDM/Pan-STARRS distribution and extends upto $z \sim 0.9$. Despite of the deeper observations with MDM, we are unable to detect a higher number of clusters within the intermediate redshift range ($0.6 < z < 0.8$) which implies that most of the undetected clusters from Griffin et al. (2016) are possibly higher redshift clusters. Unfortunately, neither PS1 nor MDM data were markedly deeper than SDSS, so only moderate progress was made towards completeness at intermediate redshifts. The $z \gtrsim 0.8$ clusters which should be 30% of the sample requires near-IR follow-up observations, which will be published in a forthcoming paper.

We can further investigate the non-detections by comparing the properties of the optically detected and non-detected candidates to the optical limiting magnitudes and various X-ray properties, as shown in Figure 3.6, for the $> 3\sigma$ overdensity threshold sample. The quality of the optical observations can be approximately by the average limiting magnitudes for the fields in the r band. For the X-ray properties, we examine the X-ray photon counts, S/N, emission core size, and off-axis angle in the *Swift* images. We used the Kolmogorov-Smirnov (K-S) test to statistically check whether the detected and undetected distributions are different. In Figure 3.6, the distribution of the limiting r band magnitudes for the MDM clusters are distinguishably clustered around higher limiting magnitudes (in the upper left quadrant), therefore indicating that the non-detections produced from the deeper MDM observations are most likely high redshift clusters or false positives in the X-ray detection methods. However, because there are only three detections in the MDM sample, the K-S tests were applied only to the Pan-STARRS targets. The K-S test results show that the optically detected and non-detected targets are distinguished by X-ray photon counts and S/N with K-S null probability of 0.0043 for both cases. This is expected since the high X-ray count or S/N clusters are more likely to be luminous and low redshift clusters. Even though we see that the clusters with large X-ray counts and high S/N are being found by the optical detection method, we do see some exceptions that could be higher redshift candidates or probably X-ray false positives. For the core distribution, there is a definite suggestion that two samples are different (P=0.0405), which indicates that X-ray cluster candidates with larger core sizes are less likely to be false positives. The off-axis angle and limiting magnitudes distributions show no clear distinction between the two populations with null-probability of 0.581 and 0.954, respectively. This confirms that the PSF of *Swift* is approximately uniform with respect to the off-axis angles. While the limiting optical magnitude is important for optically confirming X-ray clusters, if the sample contains a large fraction of high redshift clusters where the red sequence moved to the NIR band, there will always be a large fraction of non-detections in the optical bands regardless of the limiting magnitudes, which is consistent with this result. Therefore, we expect the unconfirmed cluster candidates to be higher redshift clusters that require follow-up observations in the near infrared or low luminosity intermediate redshift clusters that require significantly deeper optical observations.

We have also estimated the cluster observables like the optical richness and the X-ray luminosity for each confirmed cluster. Although this chapter only reports the estimated values and does not present the scaling relationship between the observable properties, it can be generally stated that an increasing trend is observed in the richness of the clusters with the increase in the X-ray luminosity. We find that these clusters are predominantly located on the lower end of the richness relation with $\lambda < 25$, or they are rich clusters with $\lambda > 60$. For some cases, however, the optical richness has been severely underestimated because of the missing galaxy counts at lower redshifts, which is possibly due to the poor image quality/seeing of the observations. Some higher redshift cases show an inflated estimate for the richness, which has been corrected by imposing a luminosity cut. The high redshift clusters are more prone to projection effects, and the net number counts can majorly impact the estimates for the richness. It is also important to consider that the photometric redshift estimates are subject to systematics, which could be another factor leading to the underestimation/overestimation of the richness. A detailed analysis of the X-ray and optical observables and the scaling relations for all the confirmed SACS clusters, including those in the southern hemisphere south of declination of -30 degrees, will be studied in the next chapter.

Acknowledgements

We are grateful to the anonymous referee for the helpful comments and recommendations. We acknowledge the financial support from the NSF grant AST-1413056 and NASA ADAP program NNX17AF26G.

References

Aihara, H., Allende Prieto, C., An, D., et al. 2011, ApJS, 193, 29

Abell, G. O. 1958, ApJS, 3, 211

Abell, G. O., Corwin, H. G., Jr., & Olowin, R. P. 1989, ApJS, 70, 1

Adami C., Durret F., Benoist C. et al. 2010, A&A 509, 81 (A10)

Adami C., Altieri B., Valtchanov I., 2012, MNRAS, 423, 3561

Allen S. W., Schmidt R. W., Fabian A. C., 2002a, MNRAS, 334, L11

Allen, S. W., Evrard, A. E., & Mantz, A. B. 2011, ARA&A, 49, 409

Applegate D. E. et al., 2014, MNRAS, 439, 48

Arnaud, K. A. 1996, Astronomical Data Analysis Software and Systems V, 101, 17

Assef, R. J., Kochanek, C. S., Brodwin, M., et al. 2010, ApJ, 713, 970

Bahcall, N. A. 1988, ARA&A, 26, 631

Bahcall, N. A., Fan, X., & Cen, R. 1997, ApJ, 485, L53

Bahcall, J. N., & Sarazin, C. L. 1977, ApJ, 213, L99

Bahcall, N., & Soniera, R. M. 1983, ApJ, 270, 20

Balogh M. L., Navarro J. F., Morris S. L., 2000, ApJ, 540, 113

Banerjee, P., Szabo, T., Pierpaoli, E., et al. 2018, New A, 58, 61

Barkhouse W. A., Green P. J., Vikhlinin A., Kim D., Perley D.,Cameron R., Silverman J., Mossman A. et al., 2006, ApJ, 645, 955

Basilakos, S., Plionis, M., Georgakakis, A., et al. 2004, MNRAS, 351, 989

Bertin, E. & Arnouts, S. 1996, A&AS, 117, 393

Bertin, E., Mellier, Y., Radovich, M., et al. 2002, in Astronomical Society of the Pacific Conference Series, Vol. 281, Astronomical Data Analysis Software and Systems XI, ed. D. A. Bohlender, D. Durand, & T. H. Handley, 228

Böhringer, H., Voges, W., Huchra, J. P., et al. 2000, ApJS, 129, 435

Böhringer, H., Schuecker, P., Guzzo, L., et al. 2001, A&A, 369, 826

Borgani, S., Rosati, P., Tozzi, P., Stanford, S. A., Eisenhardt, P. E., Lidman, C., Holden, B., Della Ceca, R., Norman, C., & Squires, G. 2001

Blain, A. W., Jameson, A., Smail, I., Longair, M. S., Kneib,J.-P. & Ivison, R. J. 1999, MNRAS 309, 715 (B99b)

Brammer, G. B., van Dokkum, P. G., & Coppi, P. 2008, ApJ, 686, 1503

Brodwin, M., et al. 2010, ApJ, 721, 90

Butcher H., Oemler A.Jr., 1978, ApJ, 219, 18

Bell, E. F., McIntosh, D. H., Katz, N., & Weinberg, M. D. 2003, ApJS, 149, 289B

Bonamente, M., Joy, M., LaRoque, S. J., Carlstrom, J. E., Nagai, D., & Marrone, D. P. 2008, ApJ, 675, 106

Carlberg R. G., Yee H. K. C., Ellingson E., Abraham R., Gravel P., Morris S., Pritchet C. J., 1996, ApJ, 462, 32

Carbone C., Fedeli C., Moscardini L, Cimatti A. 2012, J. Cosmology Astropart. Phys., 3, 23

Nilo Castellón, J. L., Alonso, M. V., García Lambas, D., et al. 2014, MNRAS, 437, 2607

Cavaliere A., Fusco-Femiano R., 1976, A&A, 49, 137

Carlstrom, J. E., Holder, G. P., & Reese, E. D. 2002, ARA&A, 40, 643

Chambers, K. C., Magnier, E. A., Metcalfe, N., et al. 2016

Covey, K. R., et al. 2007, AJ, 134, 2398

Clerc N., Sadibekova T., Pierre M., Pacaud F., Le F‘evre J.-P.,

Dai, X., Assef, R. J., Kochanek, C. S., et al. 2009, ApJ, 697, 506

Dai, X., Griffin, R. D., Kochanek, C. S., Nugent, J. M., & Bregman, J. N. 2015, ApJS, 218, 8

Desai, S., Armstrong, R., Mohr, J. J., et al. 2012, ApJ, 757, 83

Dressler, A. and Gunn, J. E. 1992, ApJS, 78, 1.

Dressler A., 1980, ApJ, 236, 351

Ebeling H., Wiedenmann G., 1993, Phys. Rev. E, 47, 704

Ebeling H., Edge A. C., Bohringer H., Allen S. W., Crawford C. S., Fabian A. C., Voges W., Huchra J. P., 1998, MNRAS, 301, 881

Ebeling, H., & Wiedenmann, G. 1993, Phys. Rev. E, 47, 704

Ebeling, H., Edge, A. C., & Henry, J. P. 2001, ApJ, 553, 668

Einasto J., Einasto M., Gottlober S., Muller V., Saar V., Starobinsky A.A., Tago E., Tbcker D., Ander-nach H., & Frisch P., 1997, Nature, 385, 139

Ettori S., Gastaldello F., Leccardi A., Molendi S., Rossetti M., Buote D., Meneghetti M., 2010, A&A, 524, A68

Felten, J. E. 1996, Astronomical Society of the Pacific Conference Series, Vol. 88, Mitigating the Baryon Crisis in Clusters: Can Magnetic Pressure be Important?, ed. V. Trimble & A. Reisenegger, 271

Feng Y., Chu M.-Y., Seljak U., McDonald P., 2016, MNRAS, 463, 2273

Finlator, K., et al. 2000, AJ, 120, 2615 Hawley, S. L., et al. 2002, AJ, 123, 3409

Flewelling H., 2018, AAS, 231, 436.01

Foley, R. J., et al. 2011, ApJ, 731, 86

Garilli B., Bottini D., Maccagni D., Carrasco L., Recillas E., 1996, ApJS, 105, 191

Gladders M. D., Yee H. K. C., 2000, AJ, 120, 2148

Green P., et al., 2004, ApJS, 150, 43

Goto T., Yamauchi C., Fujita Y., Okamura S., Sekiguchi M., Smail I., Bernardi M., Gomez P. L., 2003, MNRAS, 346, 601

Goto T., Sekiguchi M., Nichol R. C., Bahcall N. A., Kim R. S. J., Annis J., Ivezic´ Z., Brinkmann, J. et al., 2002, AJ, 123, 1807

Garilli, B., Maccagni, D., & Andreon, S. 1999, A&A, 342, 408

Griffin, R. D., Dai, X., Kochanek, C. S., Bregman, J. N., 2016, ApJS, 222, 1

Gladders M. D., Yee H. K. C., 2000, AJ, 120, 2148 —, 2005, ApJS, 157, 1

Goto T., Sekiguchi M., Nichol R. C., Bahcall N. A., Kim R. S. J., Annis J., Ivezic´ Z., Brinkmann, J. et al., 2002, AJ, 123, 1807

Hao, J., McKay, T. A., Koester, B. P., et al. 2010, ApJS, 191, 254

Hoekstra, H. 2007, MNRAS, 379, 317

Hoekstra, H., Herbonnet, R., Muzzin, A., et al. 2015, MNRAS, 449, 685

Hasselfield, M., Hilton, M., Marriage, T. A., et al. 2013, Journal of Cosmology and Astro-Particle Physics, 2013, 008

Hansen, S. M., Sheldon, E. S., Wechsler, R. H., & Koester, B. P. 2009, ApJ, 699, 1333

Hincks, A. D., et al. 2010, ApJS, 191, 423

Huchra J. P. Geller M. J., 1982, ApJ, 257, 423

Gladders, M. D., & Yee, H. K. C. 2005, ApJS, 157, 1

Gladders M. D., Lopez-Cruz O., Yee H. K. C., Kodama T., 1998, ApJ, 501, 571

High, F. W., Stubbs, C. W., Rest, A., Stalder, B., & Challis, P. 2009, AJ, 138, 110

Ivezi´c, Z., et al. 2007, AJ, 134, 973

Juric, M., et al. 2008, ´ ApJ, 673, 864

Kelly P. L., et al., 2014, MNRAS, 439, 28

Kodama T., Tanaka I., Kajisawa M., Kurk J., Venemans B., DeBreuck C., Vernet J., Lidman C., 2007, MNRAS, 377, 1717

Kaiser, N., Aussel, H., Burke, B. E., et al. 2002, Proc. SPIE, 4836, 154

Kim Y.-R., Croft R. A., 2004, Astrophys. J., 607, 164

Koester, B. P., et al. 2007a, ApJ, 660, 239

Kravtsov, A. V. & Borgani, S. 2012, ARA&A, 50, 353

Lopes P. A. A., de Carvalho R. R., Gal R. R., Djorgovski S. G., Odewahn S. C., Mahabal A. A., Brunner R. J., 2004, AJ, 128, 1017

Okabe N., Zhang Y.-Y., Finoguenov A., Takada M., Smith G. P., Umetsu K., Futamase T.. , ApJ , 2010b, vol. 721 pg. 875

Okabe N., Bourdin H., Mazzotta P., Maurogordato S., 2011, ApJ, 741, 116

Okabe, N., & Smith, G. P. 2016, MNRAS, 461, 3794

Postman, M., Lubin, L. M., Gunn, J. E., Oke, J. B., Hoessel, J. G., Schneider, D. P., & Christensen, J. A. 1996, AJ, 111, 61

Lauer T. R. Postman M. Strauss M. A. Graves G. J. Chisari N. E. 2014 ApJ 797 82

Metcalfe, L., et al. 2003, A&A, 407, 791

Merloni A. et al., 2012, arXiv:1209.3114

Munshi D., Coles P., 2003, MNRAS, 338, 846

Mantz, A. B., Abdulla, Z., Carlstrom, J. E., et al. 2014, ApJ, 794, 157

Li I. H., Yee H. K. C., 2008, The Astronomical Journal, 135, 809

Mazure A., Adami C., Pierre M. et al. 2007, A&A 467, 49 (M07)

Mehrtens, N., Romer, A. K., Hilton, M., et al. 2012, MNRAS, 423, 1024

Mitchell, R. J., Ives, J. C., & Culhane, J. L. 1976, in BAAS, Vol. 8, Bulletin of the American Astronomical Society, 553

Marrone, D. P., et al. 2012, ApJ, 754, 119

Maughan B. J., Giles P. A., Randall S. W., Jones C., Forman W. R., 2012, MNRAS, 421, 1583

Menanteau, F., et al. 2012, ApJ, 748, 7

McInnes, R. N., Menanteau, F., Heavens, A. F., et al. 2009, MNRAS, 399, L84

Navarro, J. F., Frenk, C. S., & White, S. D. M. 1995, MNRAS, 275, 720

Nilo Castell´on, J. L., Alonso, M. V., Garc´ıa Lambas, D., et al. 2014, MNRAS, 437, 2607

Pacaud F., et al., 2006, MNRAS, 372, 578

Popesso, P., Bohringer, H., Romaniello, M., & Voges, W. 2005, ¨ A&A, 433, 431

Postman M, Geller M., & Huchra J. 1986, AJ, 91, 1267

Postman, M., Huchra, J. P., & Geller, M. J. 1992, ApJ, 384, 404

Postman, M., Lubin, L. M., Gunn, J. E., Oke, J. B., Hoessel, J. G., Schneider, D. P., & Christensen, J. A. 1996, AJ, 111, 615

Postman, M., Franx, M., Cross, N. J. G., et al. 2005, ApJ, 623, 721

Poggianti, B. M., Smail, I., Dressler, A., Couch, W. J., Barger, J., Butcher, H., Ellis, E. S., & Oemler, A., Jr., 1999, ApJ, 518, 576

Piffaretti, R., Arnaud, M., Pratt, G.W., et al. 2011, A&A, 534, A109

Pillepich, A., Porciani, C., & Reiprich, T. H. 2012, MNRAS, 422, 44

Pierre, M., Pacaud, F., Adami, C., et al. 2016, A&A, 592, A1

Predehl, P., Andritschke, R., B¨ohringer, H., et al. 2010, in Society of Photo-Optical Instrumentation Engineers (SPIE) Conference Series, Vol. 7732, Society of Photo-Optical Instrumentation Engineers (SPIE) Conference Series

Planck Collaboration. 2011b, A&A, 536, A26

Planck Collaboration et al. 2013, A&A, 550, A129 (PI3)

Ramella M., Boschin W., Fadda D., Nonino M., 2001, A&A, 368, 776

Ramella M., Boschin W., Fadda D., Nonino M., 2001, A&A, 368, 776

Reiprich, T. H. & B¨ohringer, H. 2002, ApJ, 567, 716

Rykoff, E. S., Rozo, E., Busha, M. T., et al. 2014, ApJ, 785, 104

Rykoff E. S., et al., 2016, ApJS , 224, 1

Reiprich, T. H. & Böhringer, H. 2002, ApJ, 567, 716

Stalder, B., et al. 2012, ApJ

Sunyaev, R. A., & Zeldovich, Y. B. 1970, Comments on Astrophysics and Space Physics, 2, 66 —. 1972, Comments on Astrophysics and Space Physics, 4, 173

Sunyaev, R., & Zeldovich, I. B. 1980, MNRAS, 190, 413

Szabo T., Pierpaoli E.,Dong2 F.,Pipino A., Gunn J.,2011, ApJ, 736,1

Smith G. P., Kneib J.-P., Smail I., Mazzotta P., Ebeling H., Czoske O.. , MNRAS , 2005, vol. 359 pg. 417

Smith, G. P., Treu, T., Ellis, R. S., Moran, S. M., & Dressler, A. 2005, ApJ, 620, 78

Sif´on, C., et al. 2012, ApJ

Takey A., Schwope A., Lamer G., 2011, A&A, 534, A120

Takey A., Schwope A., Lamer G., 2013, A&A, 558, A75

Takey A., Schwope A., Lamer G., 2014, A&A, 564, A54

Takey, A., Durret, F., Mahmoud, E., & Ali, G. B. 2016, A&A, 594, A32

Tinker, J., Kravtsov, A. V., Klypin, A., et al. 2008, ApJ, 688, 709

van Breukelen, C., & Clewley, L. 2009, Mon Not R Astron Soc, 395, 1845

Voit, G. M. 2005, RvMP, 77, 207

Von der Linden, A., Best, P. N., Kauffmann, G., & White, S. D. M. 2007, MNRAS, 379, 867

Vanderlinde, K., et al. 2010, ApJ, 722, 1180

Wen, Z. L., Han, J. L., & Liu, F. S. 2012, ApJS, 199, 34

Zwicky F., Herzog E., Wild P., 1961, Catalogue of galaxies and of clusters of galaxies, Vol. I, Pasadena: California Institute of Technology (CIT), —c1961

Zehavi, I., et al. 2005, ApJ, 630, 1

Chapter 4

Optical follow-up of SACS clusters in the Southern Hemisphere

Abstract

We present a study of the optically confirmed clusters from the Swift AGN and cluster X-ray survey that are located in the southern hemisphere, using the optical data from the Dark energy survey (DES) and independent observations using CTIO/DECam. We search for galaxy overdensities in the three-dimensional space around the Swift cluster centers using the red sequence colors and photometric redshifts. We are able to confirm 64 Swift clusters with a detection significance of $> 3\sigma$. We have also estimated cluster observables, including the redshift, optical richness, BCG magnitude, BCG-to-X-ray center offset, and X-ray luminosity. We have calibrated the scaling relations between the mass proxies using the X-ray luminosity and optical richness for the 219 confirmed Swift clusters, including detections from previous works. The X-ray luminosity and optical richness for these clusters show a positive correlation that is found to be consistent with the existing scaling relations. The distribution of the offsets between X-ray centroids and

Brightest Cluster Galaxies for the clusters is in agreement with the expectations with a median of $\sim$ 180 kpc. The observed redshift distribution for all the optically detected Swift clusters is compared with the theoretical model, which shows approximately 85% completeness up to $z \leq 0.5$.

4.1 Introduction

Galaxy clusters are an incredible resource for a gamut of cosmological and astrophysical studies. Being the largest gravitational systems in the Universe, emerging from the overdense peaks of the primordial field, they act as effective tracers of the dark energy and dark matter content of the Universe (e.g., Borgani et al. 2001; Reiprich & Böhringer 2002; Seljak 2002; Viana et al. 2002; Kravtsov & Borgani 2012; Schellenberger & Reiprich 2017). They also play an integral role in shaping our understanding of galaxy formation, evolution, dynamics, and the environmental influences that define the course of galactic evolution (Dressler 1980). The high-density environment of the cluster offers an avenue for studying the physical mechanisms that relate to different cluster components, including the gas-galaxy interactions. On the cosmological front, they render competitive constraints on the cosmological models of structure growth, commensurate with other cosmological probes such as the cosmic microwave background (CMB) observations and weak lensing measurements. The evolution of cluster abundances as a function of redshift provides constraints on the matter density of the Universe (Ω_m; Carlberg et al. 1996; Evrard 1997; Schuecker et al. 2003) and the amplitude of density fluctuations (σ_8; Frenk et al. 1990; White, Efstathiou & Frenk 1993; Fedeli, Moscardini & Matarrese 2009). Furthermore, establishing the redshift evolution of the cluster mass function is crucial for constraining the dark energy parameters and testing the modified theories of gravity (e.g., Allen et al. 2011; Cataneo et al. 2014; Mantz et al. 2015; Böhringer & Chon 2016; Bolliet et al. 2019; Hagstotz et al. 2019).

With that being said, the application of galaxy clusters as cosmological tools is contingent upon the accurate estimation of cluster masses. Since the total mass of the cluster is dominated by dark matter, it is not directly observable and is usually derived from other observable quantities that are well-correlated with the cluster mass; and to that end, it is important to obtain precise and accurate observable-mass scaling relations. Most of the baryon content within galaxy clusters is observable, either in the form of stars or the hot intracluster plasma. In the optical regime, galaxy clusters appear as a conglomeration of galaxies, mapping the stellar content of the clusters. However, the gas content of the cluster lurks in the intracluster region, which consists of hot gas plasma that can be traced both with the X-rays produced via bremsstrahlung radiation (e.g., Bohringer & Werner 2010) and through the Sunyaev-Zeldovich (SZ) effect, arising from the Compton scattering of the photons of the Cosmic Microwave Background with the electrons of the ICM (Sunyaev & Zeldovich 1980). One of the main predictions of simplified cluster formation models is that clusters display self-similar behavior (Kaiser 1986; Ascasibar et al. 2006). The self-similar models assume that clusters form in a monolithic gravitational collapse that impels the shock heating of the Intracluster medium (ICM), such that the gas properties correlate with the halo mass in the form of power-law scaling relations. Several observable properties of galaxy clusters can serve as mass proxies, such as X-ray luminosity, optical richness, temperature, and velocity dispersions (e.g., Voit 2005; Lopes et al. 2006). For example, in the self-similar framework, the X-ray luminosity (Lx) of the ICM is expected to scale as $M^{4/3}$ (Sarazin 1986) for a cluster of total mass M, under the assumption that the X-ray emission is predominantly thermal Bremsstrahlung. However, various observational studies of the Lx-M relation suggest a deviation from self-similarity, with significantly steeper slopes than the predicted value (4/3), ranging from 1.6 to 2 (e.g., Edge & Stewart 1991; Allen & Fabian 1998; Markevitch 1998; Nevalainen et al. 2000; Finoguenov et al. 2001; Ettori et al. 2004; Henry 2004; Arnaud et al. 2005; Rasia et al. 2005; Balogh et al. 2006; Stanek et al. 2006; Maughan 2007; Rykoff et al. 2008; Pratt et al. 2009; Vikhlinin et al. 2009; Mantz et al. 2010; Planck Collaboration X 2011; Wang et al. 2014). This departure of the observations from the predictions based on self-similar scaling could be an outcome of complex physical processes within the cluster such as radiative cooling, preheating, feedback, quasar outflows, tidal stripping, etc. (Metzler & Evrard 1994; Valdarnini 2003), thus indicating a gap in our understanding of the underlying physics of cluster formation and evolution. Therefore accurate calibration of the inferred halo mass scale and their scaling relations with the observable properties is necessary for measuring the cluster mass function, which will provide improved constraints on cosmology and revamp our understanding of the physics of cluster formation and evolution (e.g., Kravtsov & Borgani 2012; Lopes et al. 2006).

To exploit the scientific potential of galaxy clusters, building a large homogenous catalog of clusters, sweeping a broad range of mass and redshift, holds the key. Over the years, much effort has been made by many large-scale surveys, with optical-NIR and X-ray surveys being historically more prevalent. Previously, optical detection of clusters involved visual identification of overdensities of galaxies in the optical images (Abell 1958; Zwicky, Herzog & Wild 1961; Abell, Corwin & Olowin 1989). Advances in multiband photometric surveys have given rise to a wide range of cluster finding algorithms, e.g., the red sequence method (Goto et al. 2002; Gladders et al. 2007; Koester et al. 2007a; Hao et al. 2010;

Soares-Santos et al. 2011; Szabo et al. 2011; Wen et al. 2012) that is based on the spatial abundance of red, passively evolving elliptical galaxies that form a distinct ridgeline called the red sequence (See section 1.3) in the color-magnitude space. Other methods include overdensities of galaxies in photometric redshift space (Wen et al. 2009, 2012; Szabo et al. 2011; see Allen et al. 2011), Voronoi Tesselation methods (Ebeling & Weidenmann 1993; Ramella et al. 2001; Lopes et al. 2004, Murphy et al. 2011), galaxy density mapping (Mazure et al. 2007; Adami et al. 2010) and friends-of-friends algorithms (Huchra & Geller 1982; Li et al. 2008; Feng et al. 2016) and matched-filtering (Postman et al. 1996; Lidman & Peterson 1996). Although the optical detection techniques are useful in yielding the photometric redshifts for a large population of clusters, they are prone to projection contamination from the foreground and background galaxies (Van Haarlem, Frenk & White 1997; Hicks et al. 2008). X-ray selected surveys, on the other hand, are sensitive to hot intracluster gas component (Cavaliere & Fusco-Femiano 1976; Allen, Schmidt & Fabian 2002), therefore providing immunity from these projection effects and offering a cleaner method of detection. Also, since the Intracluster medium dominates the cluster baryonic budget, X-ray selected surveys are capable of probing large volumes and identifying brighter, massive systems with well-defined masses. In Section 1.4 and Section 1.5, I have given a detailed account of X-ray surveys and the Swift AGN and cluster survey, respectively.

The Swift AGN and cluster survey (Dai et al. 2014) is an X-ray-selected survey that is suited for detecting clusters at intermediate redshifts. The first release of SACS provided a catalog of 442 cluster candidates. Optical follow-up using the SDSS DR8, MDM-2.4m, and Pan-STARRS, has confirmed 159 SACS clusters in the sky, north of declination $\delta = -30°$. In this chapter, we have applied the cluster detection method, developed in Chapter 3, to the optical data from the Dark energy survey (DES) and our allocated observations with CTIO/DECam. We have also explored the relationship between the X-ray and optical cluster observables for all optically confirmed SACS clusters. The layout of the chapter is as follows. Section 4.2 describes the optical follow-up data used in this work. In Section 4.3, we discuss the verification of the *Swift* cluster candidates using the optical over-density/red sequence method. In Section 4.4, we explain our measurements of cluster observable properties. In Section 4.5, we end with the conclusions and a discussion of our results. We assume cosmological parameters of $\Omega_M = 0.27$, $\Omega_\Lambda = 0.73$, and $H_0 = 70$ km s^{-1} Mpc^{-1} throughout the chapter.

4.2 Data acquisition and Calibration

4.2.1 CTIO/DECam Data

The optical counterpart used in this study is data obtained from the Dark Energy Camera Imager (DECam) at the Blanco-4m telescope located at the Cerro Tololo Inter-American Observatory (CTIO). We had four nights in April 2014 (2014/04/17-20) and four nights in July 2014 (2014/07/03-06); however, given the atmospheric constraints, we could only observe for six and a half nights. We performed multiband photometric imaging in *griz* bands with each target exposed for 10-15 minutes per filter to achieve an optimal magnitude depth of 23.5 in the *g* band. We split each observation into three sub-exposures, dithered to avoid bad pixels and minimize the effect of the CCD gaps. The 2.2 degree diameter field of DECam (composed of 62 $2k \times 4k$ CCDs for imaging) is ideal for this study (Flaugher 2015). We took advantage of the large field of view of DECam, and in several cases, we observed multiple targets in one field. For each target, we observed galaxies in the source and background regions. Here, we have defined our source region to be the circle of $2'$ or $3'$ radius centered on the Swift-detected X-ray source. The background region is defined to be the annulus around each source with inner and outer radii of $3.5'$ and $8.5'$, respectively. The local background is used to account for cosmic variance. Additionally, 2-3 standard star fields were observed intermittently per night between science exposures, mainly taking advantage of the SDSS equatorial stripes (Stripe 82 and Stripe 10) and the recommended Southern $g'r'i'z'$ standards (Smith et al. 2007). When the SDSS fields were unavailable, we used Landolt star fields (Landolt, 2009) containing at least 28 measured star magnitudes.

The imaging data for our observation programme was downloaded from the NOAO Science Archive. We use the resampled images that were debiased, flat fielded, and corrected for instrumental signatures in the processing pipeline, and further remapped to a standard orientation such that each pixel is reprojected to a common WCS Tangent point. Here each image is a multi-extension fits (MEF) file, with each extension corresponding to a single CCD. Therefore we use SWarp (Bertin et al., 2002) to combine all of the CCD frames to make images that are centered on each target with a size of 3800×3800 pixels (or $17.1'$ on each side), encompassing both source and background galaxies. Furthermore, we co-add the sub-exposures of each filter using median combine to create stacked g, r, i, and z images. Finally, we co-add the stacked images of all filters to create a χ^2 detection or a panchromatic image for each target using SWarp configuration parameters: `COMBINE_TYPE = MAX` and `OVERSAMPLING =5`. We use SExtractor (Source Extractor; Bertin et al. 1996) in the dual image mode with the default settings to obtain catalogs of all sources in g, r, i, and z images with location, shape, magnitude, and stellarity index or star/galaxy classifier information. We use the panchromatic image for the detection of sources and the individual filter stacked images for extraction of magnitudes. For the standard star fields, however, we use a different approach. We start by arranging the single epoch images in chronological order, followed by the co-addition of images (of the same field and filter) that are closely separated in time. The magnitudes for these coadded frames in g, r, i, z band are obtained by running SExtractor in the single image mode.

The photometric calibration for each field was performed by calculating the calibrated magnitude offset from each observed standard star field using the mean photometric zeropoint equation:

$$m_{cal} = m_{inst} - a_n - b_n((\mathrm{stdcol}) - (\mathrm{stdcol})_0) - k_n X \tag{4.1}$$

where m_{cal} is the calibrated magnitude, b_n is the instrumental color coefficient, $\mathrm{stdcolor}_0$ is the reference color such that $g - r = 0.53$ for g and r bands and $r - i = 0.09$ for i band, k_n is the first-order extinction coefficient, and X is the mean airmass. The index n refers to the filter such as g, r, i, z. We find the stdcol by averaging the color of objects within 7 arcmin of the X-ray source center. m_{inst} is given as:

$$m_{inst} = m_{aper} + 2.5\ log_{10}(t_{\mathrm{exp}}) - ZP \tag{4.2}$$

where m_{aper} is the SExtractor magnitude, t_{exp} is the average exposure time of the sub-exposures and ZP is the instrumental zeropoint. Coefficients b_n and k_n are filter and CCD dependent, although variation from CCD to CCD is small. For calculations, we have averaged them across CCDs for each filter. The values for X and t_{exp} are the mean of the airmass and exposure times mentioned in the image headers for the sub-exposures. Thus the only unknown in Equation 4.1 is a_n, which is the photometric zeropoint. To find a_n, for each standard star field observed, we match the objects in the source catalog to the standard star catalog (using a matching radius of $1''$) and calculate the offset a_n by setting $g_{cal} = m_{std}$, where m_{std} is the magnitude obtained from the standard star catalog. We average the offsets to obtain the final photometric zeropoint to calibrate our SExtractor magnitudes. We perform this method for all four filters (g, r, i, z) utilized, where the colors used in equation 4.1 are $g - r$, $r - i$, $i - z$, $z - i$, respectively.

4.2.2 Dark Energy survey: DR1 data

The Dark energy survey is a wide-area multi-band photometric survey that maps $\sim$ 5000 square degrees of the southern sky in five filters ($grizY$). DES uses the 570-megapixel Dark Energy Camera (DECam; Honscheid et al. 2008, Flaugher et al. 2015), which is built by the DES collaboration and mounted on the CTIO-4m Blanco telescope, also used for our independent observations. In this work, we use data from DES DR1 observations that were taken between August 2013 to February 2016. DR1 consists of coadded images and source catalogs from the first three years of its operation. The DES footprint covers a larger area overlapping with the South Pole Telescope survey (Carlstrom et al. 2011) and SDSS Stripe 82 (Abazajian et al. 2009) while excluding the galactic plane. The median limiting magnitudes at a S/N threshold of 10 across the DES DR1 footprint is $g = 24.2$, $r = 23.9$, $i = 23.3$, $z = 22.6$, $Y = 21.3$. Out of the 442 clusters in SACS I, 74 cluster candidates fall in the sweep of DES DR1. We downloaded the catalogs for each target cluster using the query database DESaccess managed by National Center for Supercomputing Applications (NCSA). Object catalogs were downloaded for the

Data	**Filters**	**Catalog Parameters**	**Star-Galaxy Classifier**

CTIO/DECam	g, r, i, z	`MAG_AUTO`
		`MAGERR_AUTO`
		`CLASS_STAR`
			`CLASS_STAR` >0.8 (Stars)
			`CLASS_STAR` <0.8 (Galaxies)

DES	g, r, i, z, Y	`MAG_AUTO`
		`MAGERR_AUTO`
		`SPREAD_MODEL`
		`SPREADERR_MODEL`
			`EXT_COADD` = ((`SPREAD_MODEL_I`+ 3 `SPREADERR_MODEL_I`) >0.005)
			+ ((`SPREAD_MODEL_I` + `SPREADERR_MODEL_I`) >0.003)
			+ ((`SPREAD_MODEL_I` − `SPREADERR_MODEL_I`) >0.003)
			
			Each boolean condition in the above relation returns 1 if true and 0 otherwise, such that:
			
			`EXT_COADD` = $0-1$ (Stars)
			`EXT_COADD` = $2-3$ (Galaxies)

Table 4.1 Star/galaxy classifiers for the CTIO/DECam and DES data

sources that fall within a circumference of 10 arcmins around the X-ray centroid position of the cluster. To distinguish point sources (typically stars) from resolved sources (galaxies), we have utilized the `SPREAD_MODEL` estimator, which has been developed as a morphological classifier for the DES Data management pipeline (Desai et al. 2012; Abbott et al. 2019). The segregation between stars and extragalactic sources is defined by a parameter `EXT_COADD` (See Abbott et al. 2019), which is given as a sum of three independent boolean conditions on the `SPREAD_MODEL` (See Table 4.1), such that a value of $0-1$ indicates a stellar source and $2-3$ indicates an extragalactic source. Table 4.1 describes the star/galaxy classifiers applied to the source catalogs of the CTIO/DECam and DES.

4.3 Cluster detection strategy

4.3.1 Photometric redshift estimation

Galaxy clusters exhibit spatial clustering of galaxies in all three dimensions, which we view as a projection on a 2-D sky traced by the *RA* and *Dec.* Because of the lack of knowledge of the exact coordinates of the galaxies in the 3-D space, the line of sight galaxies can be misunderstood as cluster members and can contaminate the richness measures. This causes a large scatter in the richness–mass relations and can especially compromise the richness estimates for poorer clusters. Therefore, there is a need for cluster-finding algorithms that can accurately identify the cluster members and de-project the background contamination. Multiband imaging provides the colors for the galaxies, which has proven to mitigate the projection effects to a great degree as compared to early cluster detection methods that relied on single-band magnitudes. In this work, we have utilized two different types of approaches to identify cluster. The first method utilizes the red sequence method (Visvanathan & Sandage 1977; Bower et al. 1992; Gladders et al. 1998; Lopez-Cruz et al. 2004; De Lucia et al. 2007; Stott et al. 2009; Mei et al. 2009; Hao et al. 2009) to locate overdensity of galaxies in the color space. Because the member galaxies of a galaxy cluster exhibit a tight color-magnitude relation with a small intrinsic scatter and a relatively flatter slope, this can be used to eliminate the contamination from the field galaxies. Furthermore, we have also taken some inspiration from the GMBCG method (Hao et al. 2009), which is conditioned upon the existence of the red-sequence feature and the Brightest cluster galaxy (BCG) for successful cluster detection. We will discuss our BCG identification method in a later section.

We first study the cluster candidates using multiband color information by identifying the overdensities in three-dimensional space spanned by galaxy positions (RA, Dec) and the photometric colors. For the analysis, we select galaxies by imposing conditions on the star/galaxy separator (See Table 4.1), `CLASS_STAR` $<$ 0.8 (for CTIO/DECam) and `EXT_COADD`≥ 2 (for DES), and magnitude uncertainties `MAG_AUTOERR` < 0.33 (S/N =3). We consider a fixed radius of $3'$ around the X-ray centroid as the source region for each cluster candidate. This is a reasonable assumption considering expected redshifts of the clusters are $z < 0.8$ and typical cluster size ranges between $1 - 2$ Mpc h^{-1}. Although the search radius should be scaled according to the redshift, we use an optimum radius that can include all the galaxies at low redshifts and effectively weed out the background at high redshifts. The background here refers to the projection contamination due to the interloping galaxies, which we have approximated from an annulus region around the cluster center to account for cosmological variance. Since the DECam fields are large enough, it is possible to estimate the local background while ensuring consistency in terms of the photometric depth and seeing between the source and background regions (Valotto et al. 1997; Paolillo et al. 2001; Goto et al. 2002b; Popesso et al. 2005). The background region for the DECam fields is defined to be an annulus around each source with inner and outer radii of $4'$ and $8.5'$, respectively. The background area also includes CCD gaps, so the percentage of area affected is taken into account. The background annulus for the DES data extends from $7'$ to $10'$ around the X-ray centroid position.

In this chapter, we have followed the cluster detection algorithm introduced in Chapter 3, where the color distribution of the source galaxies is compared to the background distribution to identify galaxy overdensities. Because of the availability of multiband data, we have explored clustering in various color domains: $g-r$, $r-i$, $i-z$, and $r-Y$ (for DES). For accurate determination of the red sequence color, the data is linearly binned using different bin widths (0.05, 0.01, and 0.015), with or without half shifts in the bin center. Since the area of the background and source region are unequal, the background counts per bin are normalized with respect to the source region using the ratio of their respective areas. The galaxy excess count per bin is defined as $n_s - n_b$ for each individual bin, where n_b is the normalized background count. Once the maximum galaxy excess bin is located, we check whether the neighboring bins fulfill the overdensity condition $n_s/n_b > 2$. The bins that satisfy the overdensity condition (hereinafter referred to as overdense bins) are combined together to determine the mean color and standard deviation of the red sequence. The detection significance is calculated as $\sum n_s / \sqrt{\sum \left(n_s + \frac{A_s}{A_b} n_b \right)}$, where the summation runs over all the overdense bins and A_s and A_b is the area of the source and background region, respectively. We use the mean red sequence color to estimate the redshift of the cluster using the color–redshift power law relation derived in Chapter 3 (See Figure 3.2). As the redshift increases, the red sequence makes appearances in different colors. This is because the 4000 Å break moves across filters with the increase in redshift. Therefore, the reference color will vary for varying redshifts. For $z < 0.35$, $g - r$ is used to detect the red sequence. For $z > 0.35$, the red sequence makes its way into the SDSS r band, and the $r - i$ color serves as a reference color for redshifts up to $z \sim 0.7$. For $0.7 < z < 1.0$, the ridgeline enters the $i - z$ color, and as $z > 1.0$, it progresses into the infrared territory. For the purpose of detection of red sequence, we have used $g - r$, $r - i$, $i - z$, and $r - Y$ colors; however, we have only used $g - r$ and $r - i$ colors for estimating the redshifts. The redshift error is derived from the color uncertainty using error propagation, which is then quadrature combined with the Root mean square error (RMSE) of the color$-$redshift relation.

The second method of deprojecting the galaxies uses the photo-z estimates obtained from the multiband imaging data. There are various photo-z estimators that exist and can be broadly divided into two main types: the spectral energy distribution (SED) template fitting (Beńıtez 2000; Arnouts et al. 2002; Coe et al. 2006; Ilbert et al. 2006; Brammer, van Dokkum & Coppi 2008; Beck et al. 2017a), and machine learning (Wadadekar 2005; Collister et al. 2007; Gerdes et al. 2010; Brescia et al. 2014; Cavuoti et al. 2015; Beck et al. 2016; Salvato et al. 2019). In this work, we have used an SED template fitting photo-z estimator called EAZY

(Brammer et al. 2008). EAZY fits a linear combination of galaxy templates to the observed galaxy spectral energy distribution to estimate photometric redshifts. Because some galaxies have colors that are degenerate at different redshifts, the resultant probability distribution function has peaks at multiple redshifts. To help with this, we have utilized the redshift-magnitude prior, discussed in Brammer et al. (2008). This prior assigns a lower probability for a high-z galaxy to have a large apparent magnitude. We compared the EAZY-determined redshifts with known spectroscopic redshifts for the SDSS galaxies using the standard star calibration data. We found a good agreement between EAZY photo-zs and SDSS photometric redshifts within the redshift range $[0.3-0.8]$. The efficacy of template fitting photo-z estimators is limited by the accuracy of the SED template and the range as well as the quality of the photometric data. $u-g$ color information is required for tight detection of the Balmer break at low redshifts and the Lyman break at $z > 2$. Because of the lack of u band imaging data in our case, we see a large spread in EAZY photo-zs for redshifts $z \leq 0.3$. Once the photo-zs are obtained, we compare the source distribution with the background distribution to identify overdensities in the redshift space using the procedure described in Chapter 3. The mean redshift (z_o) and the standard deviation (σ_o) of the overdense bins is calculated, along with the significance of detection for all the cluster candidates. The standard error is $(\sigma_o/\sqrt(n)$, where n is the count of galaxies in the overdense bins. The redshift uncertainty is the quadrature sum of the standard error and mean EAZY photo-z uncertainty for all the selected galaxies. Due to the unreliability of EAZY photo-zs at the low redshift end and, in general, the limitations of the photometric redshifts, we do not observe agreement between the EAZY redshift and the red sequence redshift of the cluster. Therefore, we have used the cluster redshift with the highest detection significance in subsequent analyses.

4.3.2 BCG center identification

The Brightest Cluster Galaxy (BCG) is the most luminous and massive galaxy in the cluster (e.g., Sandage & Hardy 1973; Schombert 1986; Brown 1997). They are typically elliptical galaxies that reside near the geometrical and kinematical center of the parent cluster. The central galaxies of the cluster lie at the base of the potential well and are usually quenched of any start formation activities, which suggests a strong link between the origin of BCG and the formation of the cluster. This distinct feature is unique to clusters and forms the basis of many optical cluster finding algorithms (Koester et al. 2007; Hao et al. 2010; Oguri et al. 2018). Locating a tight clustering of galaxies in redshift/color space in tandem with the identification of a BCG acts as an effective strategy for the detection of galaxy clusters (Hao et al. 2010). Thus, for each Swift cluster candidate with a $> 3\sigma$ overdensity, we have also identified the central BCG. First, we select the galaxies within a search radius of 1 arcmin around the X-ray centroid with redshifts falling within 1σ of the peak redshift of the cluster. If the number of galaxies within the circle is < 4, then we increase the size of the circle to $2'$ to include more galaxies for comparison. If the number of galaxies still falls short of 4, the search radius is extended to a final source radius of $3'$. Among the selected galaxies, BCG is recognized as the galaxy with the brightest r band magnitude. We have carried out the search in expanding circles to reduce the effects of contaminating galaxies while ensuring focus on the high-density region of the cluster. We were able to identify BCGs for all the confirmed clusters, and also measure their absolute r magnitudes and physical offset from the X-ray centers (in Mpc). The physical separation between the X-ray centroid and member galaxies is determined using the photometric redshift estimates derived above.

While it is commonly assumed that both the BCG and the X-ray centroid mark the center of the potential well of the cluster, and their positions should coincide, studies reveal a disparity between the X-ray center and the optical center of the cluster. There are various explanations for the observed miscentering. The evolution of massive halos through mergers can explain the misalignment of the central galaxy from the local minimum of the gravitational potential (e.g., Martel et al. 2014). Another plausible explanation is that the brightest halo galaxy could be a satellite galaxy instead of a central galaxy (e.g., Weinmann et al. 2006; Pasquali et al. 2009; Skibba et al. 2011), which will affect the selection of the optical center by most cluster finding algorithms. Color-based algorithms may misidentify the cluster center in scenarios where the central galaxy experiences a recent uptick in star formation (e.g., Donahue et al. 2015) or when two progenitor halos with almost identical central galaxies are in the process of merging (e.g., Vikhilin et al. 2001). Moreover, a line-of-sight galaxy that lies outside the main halo is at the risk of being wrongfully identified as a central galaxy due to the inevitable projection effects. In Figure 4.4, we show the distribution of the offsets between the BCG and the X-ray center for all the Swift optically confirmed clusters. Here we model the offset distribution as a combination of well-centered and off-centered components, defined as:

$$P(x) = \frac{\rho}{\sigma_1}\, e^{-x/\sigma_1} + \frac{(1-\rho)\, x}{{\sigma_2}^2}\, e^{-x/\sigma_2} \tag{4.3}$$

where $x = r_{off}/(1\ \mathrm{Mpc})$ and r_{off} is the the X-ray-to-BCG offset in Mpc. The concentrated component of the distribution represents the well-centered cluster population with small BCG-to-X-ray offsets, and is described by an exponential distribution, characterized by the parameter σ_1. The elongated component models the broad tail of the distribution that represents the mis-centered population with

Table 4.2. BCG offset model parameters constraints for the SACS sample

Catalog	σ_1	σ_2	ρ
SACS	0.085 ± 0.013	0.266 ± 0.031	0.373 ± 0.053

large offsets, and is described by a Gamma function with a scale parameter σ_2. In the above model, ρ and $1 - \rho$ denotes the fraction of the well-centered and mis-centered clusters, respectively. On applying this offset model to the sample of SACS clusters, we obtain constraints on the model parameters (σ_1, σ_2, ρ). Table 4.2 lists the best fitting parameters for the offset distribution.

4.4 Cluster observables

4.4.1 X-ray Bolometric Luminosity

We use an X-ray spectral fitting package XSPEC (Arnaud et al. 1996) to calculate the X-ray bolometric luminosities (L_X) for the SACS clusters from their X-ray flux estimates in the [0.5–2 keV] band from Dai et al. 2015. The cluster emission is described using a multiplicative component model, which includes a partially absorbed APEC (Brickhouse et al. 2000; Smith et al. 2001) spectral emission model and a Galactic absorption model wabs (Morrison & McCammon 1983). The Galactic column density of hydrogen is derived from the HI4PI maps (HI4PI collaboration 2016) for the specified cluster location using the nH command in XSPEC. The plasma temperature is assumed to be 5 keV (Griffin et al. 2016), and metallicity is fixed at 0.3 solar (Anders & Grevesse 1989). We assume a β model (Cavaliere & Fusco-Femiano 1978) with $\beta = 2/3$ to correct the X-ray luminosity for

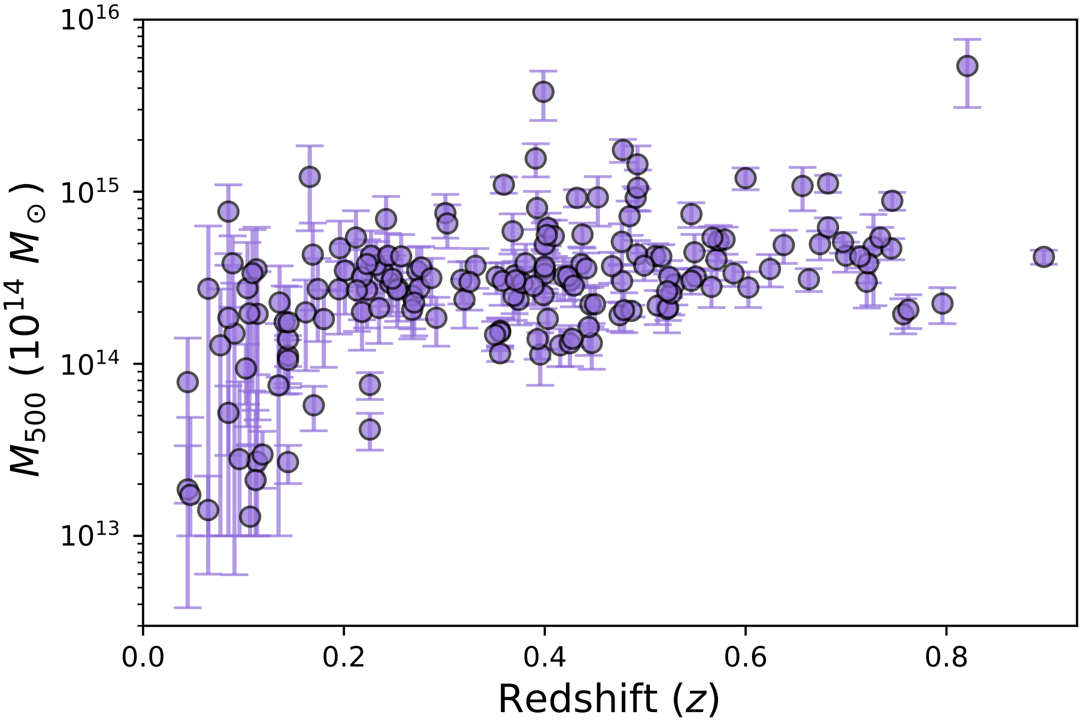

Figure 4.1 Cluster mass M_{500} (in $M_\odot$) as a function of redshift. All optically confirmed SACS clusters are shown in purple circles. An increasing trend is observed with increasing redshift, which is in line with the expectations. At low redshifts (in the bottom left quadrant), we see a handful of galaxy groups with $M_{500} < 10^{14}$ $M_\odot$.

an aperture of size 1 Mpc. This corrected aperture is consistent with the aperture used for optical richness estimates (discussed in the next section). We have used our photometric redshift measurements in this analysis. For the calculation of error in L_X, we only take into account the statistical uncertainties associated with the X-ray photon counts. Since X-ray luminosity acts as a mass proxy, L_X can be used to estimate cluster masses. We measure the M_{500}, mass within a radius of R_{500} where the density of the cluster is 500 times the critical density of the Universe, using an evolving $L_X - M$ relation (Vikhlin et al. 2009), given below.

$$\begin{aligned}\ln\ L_X = (47.392 \pm 0.085) + (1.61 \pm 0.14) \ln\ M_{500} + (1.850 \pm 0.42) \ln(E(z)) \\ -0.39 \ln(h/0.72) \pm (0.396 \pm 0.039)\end{aligned} \tag{4.4}$$

where E(z)=H(z)/H_0. We have estimated the mass of the cluster within R_{500} because it represents the radius within which the clusters are reasonably relaxed (Evrard et al. 1996) and luminosity measurements are relatively robust. In Figure 4.1, we show the redshift evolution of cluster mass M_{500} for all the optically confirmed Swift clusters.

4.4.2 Optical richness

The richness of a cluster, denoted as λ, is a measure of the member galaxies of the cluster and serves as an optical mass proxy (Popesso et al. 2005). To estimate λ for the SACS clusters, we start with measuring the observed galaxy count, N_{obs}, which is the excess galaxy count over the estimated background within the projected source region and colors ranging within one standard deviation of the red-sequence color. Alternatively, for the clusters with a non-detected red sequence

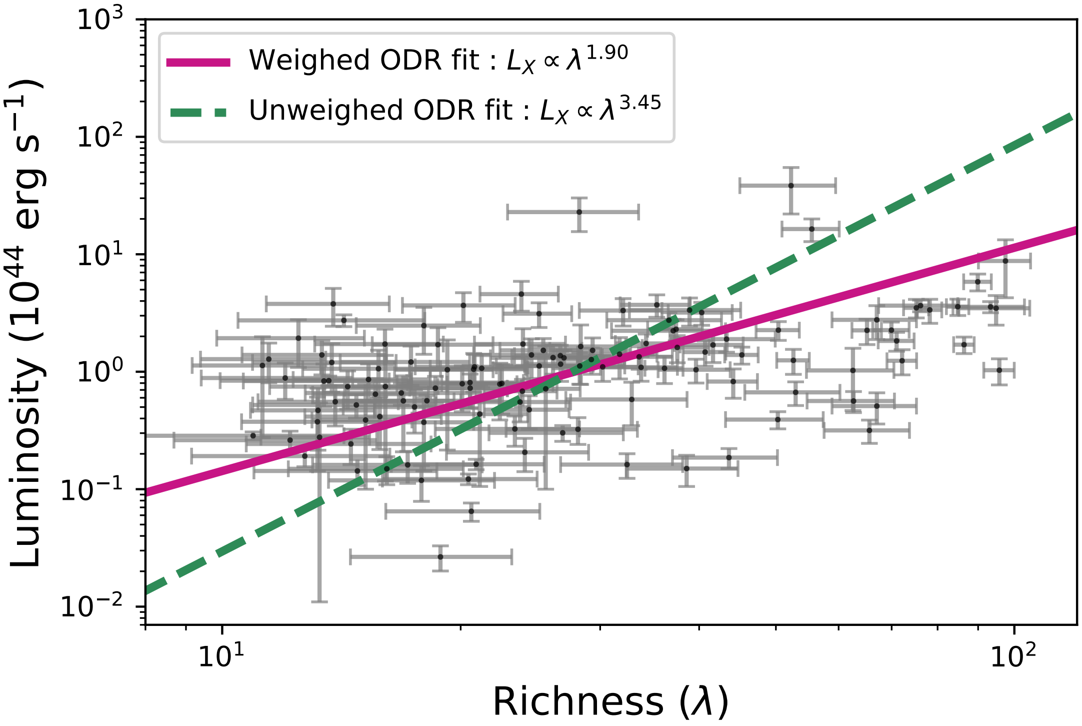

Figure 4.2 X-ray Bolometric as a function of optical richness is shown. All optically confirmed SACS clusters are shown in gray. The errors in L_X and λ are represented by the vertical and horizontal error bars, respectively. The magenta and green line depicts the weighed ODR fit and unweighed ODR fit for the relation.

but a significant detection in redshift space, galaxy counts are considered within 1-sigma interval for the inferred redshift. The optical richness λ is calculated as the number of galaxies with magnitude brighter than M_* or luminosities greater than L_*. Here, we assume a Schechter Luminosity function:

$$\begin{aligned} \phi(M)\ dM = (0.4 \ln 10)\ \phi_*\ \left(10^{0.4(M_*-M)}\right)^{1+\alpha} \\ \times \exp\left(-10^{0.4(M_*-M)}\right)\ dM \end{aligned} \tag{4.5}$$

such that M_* is the characteristic break magnitude where the power-law form of the function lays off and α is the faint end slope. We use $\alpha = -1.07$, adopted from Bell et al. 2003 for the r band. We assume that the break magnitude evolves as:

$$M_*(z) = M_*(z = 0) - \beta z \tag{4.6}$$

where $\beta = 1.2$ and $M_*(z = 0) = -21.34$ (Dai et al. 2009). To calculate the normalisation ϕ_*, the apparent r-band limiting magnitude of the field is converted to an absolute magnitude limit for each confirmed SACS cluster. For determining absolute magnitude limit M_{lim}, we account for the galactic dust extinction at each cluster location using the NED Galactic extinction calculator. We also apply the K-corrections (Oke & Sandage 1968; Hogg et al. 2002) derived from the low resolution SED templates (LRT; Assef et al. 2010) for elliptical galaxies. On integrating the Schechter luminosity function over magnitudes brighter than M_{lim}, we can determine ϕ_* using the observed galaxy count (N_{obs}) and the absolute magnitude limit. Since N_{obs} is determined for a projected radius of $3'$, we scale λ to an aperture size of 1 Mpc, assuming an NFW density profile (Navarro et al. 1995). The richness error is dominated by the uncertainties associated with the observed galaxy counts ($\sqrt{N_{obs}}$).

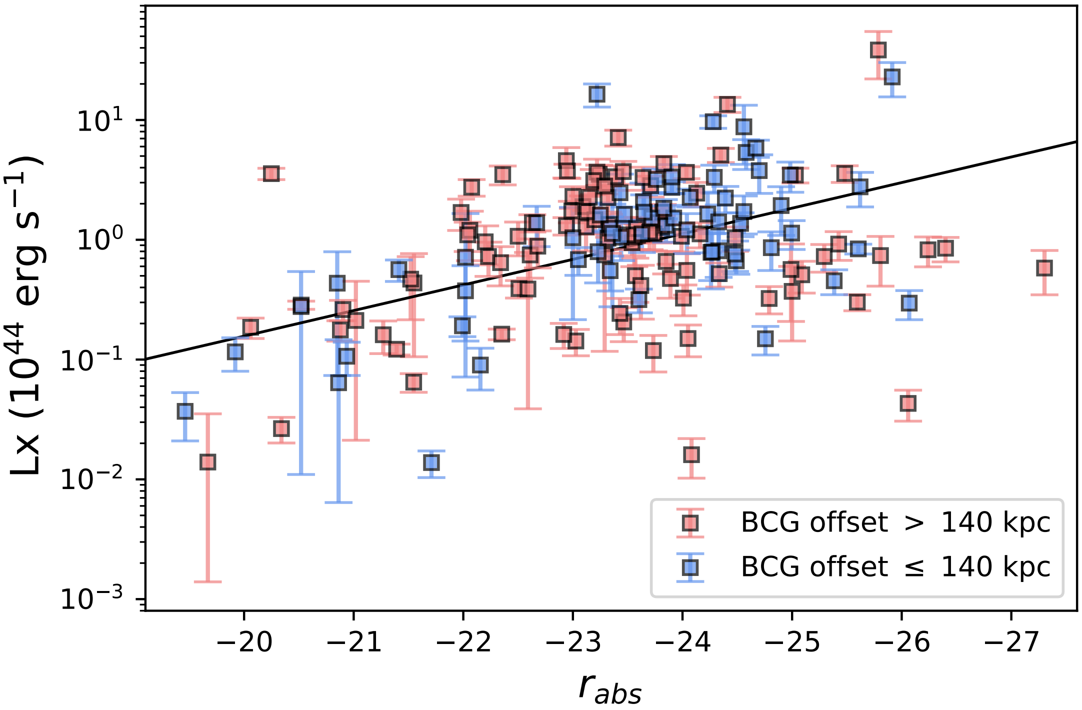

Figure 4.3 X-ray Bolometric Luminosity vs BCG Absolute r Magnitude. The data points are all optically confirmed SACS clusters segregated by their BCG-to-Xray offsets. Pink points indicate BCG offsets $\leq$ 140 kpc and blue ones indicate BCG offsets $>$ 140 kpc. The black line is the corresponding least squared regression fit. We observe a mild positive correlation between L_X (proxy for gas mass) and r_{abs} (proxy for BCG luminosity), with Spearman correlation coefficient of $\rho = 0.33$ and p value of < 0.001. The clusters with small BCG offsets (in pink) show a stronger correlation than the clusters with larger offsets (in blue), with correlation coefficients of 0.53 and 0.19 and probabilities of < 0.001 and 0.09, respectively.

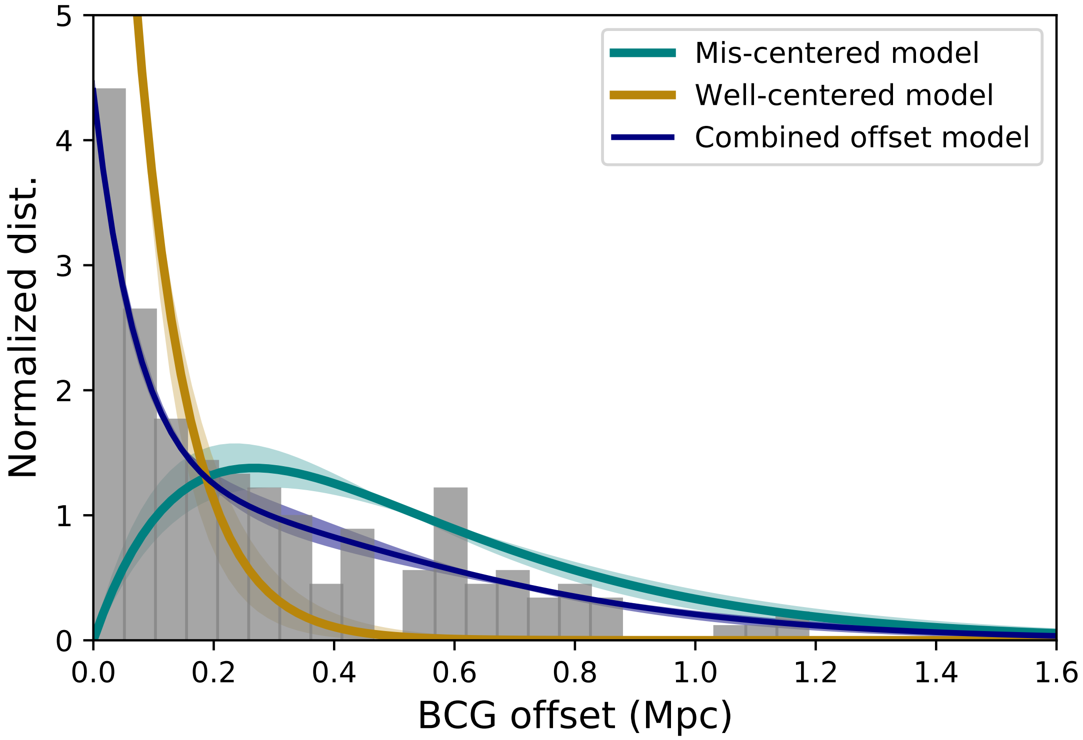

Figure 4.4 Distribution of the offsets between the BCGs and the X-ray centroid position for the 222 optically confirmed SACS clusters. The distribution is fitted with a two component model (navy) that includes a concentrated component (teal) and an elongated component (yellow), representing the well-centered and off-centered population of SACS clusters, respectively. The shaded curves represent the 68% confidence intervals for the best fit.

4.5 Results and discussion

In this Chapter, we have optically identified 64 SACS clusters from the Southern Hemisphere using the data from our independent observations with CTIO/DECam and the Dark energy survey DR1. All the confirmed clusters show a $> 3\sigma$ overdensities with redshifts extending up to $z \sim 1$. The redshift distribution of the detected SACS clusters is shown in Figure 4.5, where the cluster distribution for this paper and all the confirmed SACS clusters are shown in navy and pink, respectively. We also compare the observed distribution with the theoretical predictions obtained using a cluster mass function model from Tinker et al. (2008). We assume a cosmology with $\Omega_m = 0.25$, $\sigma_8 = 0.9$, $h = 0.72$, and $\Delta = 2000$, and dark matter halos with masses ranging from $10^{14}h^{-1}M_{\odot}$ to $10^{15}h^{-1}M_{\odot}$. The model also takes into account the flux limit and the area of the survey. We find that the redshift distribution of the optically confirmed sample is in line with the expected distribution such that the SACS catalog is complete up to $z \sim 0.2$ and is about 84% complete for $z \lesssim 0.5$. Beyond $z > 0.5$, we observe a decline in the number of detections. SACS clusters with $0.5 < z < 0.8$ are intermediate redshift clusters that possibly require deeper optical observations. Since we have used data from various resources with varying photometric depths, the non-detections in the intermediate redshift range can be attributed to the observational limitations in particular. Please note that a small percentage of detections have unreported redshifts which have been unaccounted for in the overall distribution. Clusters with $z \gtrsim 0.8$ form approximately 30% of the total SACS sample and need near-IR follow-up observations to confirm clustering and measure their redshifts.

Additionally, we have also estimated the optical and X-ray properties for the confirmed SACS clusters and studied the scaling relations between these cluster observables. Figure 4.3 shows the bolometric X-ray luminosity as a function of the optical richness for all the confirmed SACS clusters. L_X and λ are cluster observables that correlate well with the cluster mass and are often used as 'mass proxies'. L_X traces the gas mass, and measurements of the luminosity-mass relations imply that the more luminous cluster will have a correspondingly higher mass (Reiprech & Böhringer et al. 2002, Stanek et al. 2006). While the optical richness accounts for the galaxies physically bound to the cluster, and under the assumption that the number of bound galaxies is proportional to the cluster potential, the clusters with more members galaxies should have larger overall mass, which is evident in the measured optical richness–mass relations (e.g., Rozo & Rykoff 2014, Chiu et al. 2019). We use an error dependent weighted orthogonal regression fit to obtain the scaling relation $L_X/10^{44} = 10^{-2.75}\lambda^{1.90}$ in log space. The fitted relation is shown by a solid magenta line in Figure 4.2. In the absence of error dependent weights, we obtain a scaling relation of $L_X/10^{44} = 10^{-4.98}\lambda^{3.45}$, which is represented by the green dashed line in the Figure 4.2. The orthogonal regression method minimizes the sum of squared perpendicular distance between the data points and the fitted line, and is a comparatively robust model since it takes into account the errors in both luminosity and richness measurements (Isobe et al. 1990). Our slope of 1.90 agrees better with the slopes reported in Dai et al. (2009), Kochanek et al. (2003), and Griffin et al. (2016). The $L_X - \lambda$ relation from other studies in the literature (e.g., Lopes et al. 2006; Donahue et al. 2001; Yee and Ellingson 2003) generally favor steeper slopes with measurements ranging from 1.84 to 5.86. Our slope from the weighed ODR fit is on the shallower end of these studies and agrees with self-similarity (Kaiser et al. 1991; $L_X \propto \lambda^{1.3}$). However, the error-independent slope complies with some existing measurements with steeper slopes. Nevertheless, comparison between different measurements is difficult as the results vary based on the fitting algorithms and individual methods of estimation of L_X and λ, with each measurement subject to its own systematic uncertainties.

Furthermore, we have also studied the optical–X-ray center offset distribution for all the SACS clusters and found that the distribution displays a broad tail that extends up to 1.4 Mpc from the compact core. The median miscentering distance is found to be ~ 188 kpc. These results show agreement with the BCG offset distributions from several other studies (e.g., Lin & Mohr et al. 2007; Dai et al. 2007; Von der Linden 2007; Zhang et al. 2019). We also model the SACS offset distribution as a mixture of exponential and gamma functions, representing the well-centered and mis-centered cluster populations, respectively (Zhang et al. 2019). The fraction of correctly-centered clusters with a characteristic offset of $\sigma_1 = 85 \pm 13$ kpc is $\sim 40\%$. The off-centered model is constrained to a characteristic offset of $\sigma_2 = 266 \pm 31$ kpc and a large miscentering fraction of 60%. A visual check is needed at this stage to test the accuracy of our algorithm in correctly identifying the BCG, especially to test cases with close cluster pairs or slightly bluer central galaxy. A larger sample of clusters is required to disentangle the miscentering due to the systematics affecting the correct identification of BCG with our algorithm from the actual off-centered population of disturbed clusters. We also study the relationship of luminosity as a function of the absolute r band magnitude of the BCG (r_{abs}). We use an orthogonal regression method to fit the data and observe a positive correlation between the X-ray bolometric luminosity or mass of the ICM with the luminosity or the mass of the BCG. These two observables show a moderate positive correlation, with a Spearman's correlation coefficient $\rho = 0.33$ and a p value of < 0.001. These results are consistent with the expectations and also previous measurements for SACS clusters with SDSS confirmations (Griffin et al. 2016).

Acknowledgements

We acknowledge the financial support from the NSF grant AST-1413056, NASA ADAP program NNX17AF26G, and University of Oklahoma's Bullard dissertation completetion fellowship. This project uses archival data from the Dark Energy Survey (DES). Funding for the DES Data release 1 has been provided by the U.S. Department of Energy, the U.S. National Science Foundation, the Ministry of Science and Education of Spain, the Science and Technology Facilities Council of the United Kingdom, the Higher Education Funding Council for England, and the participating Institutions in the DES.

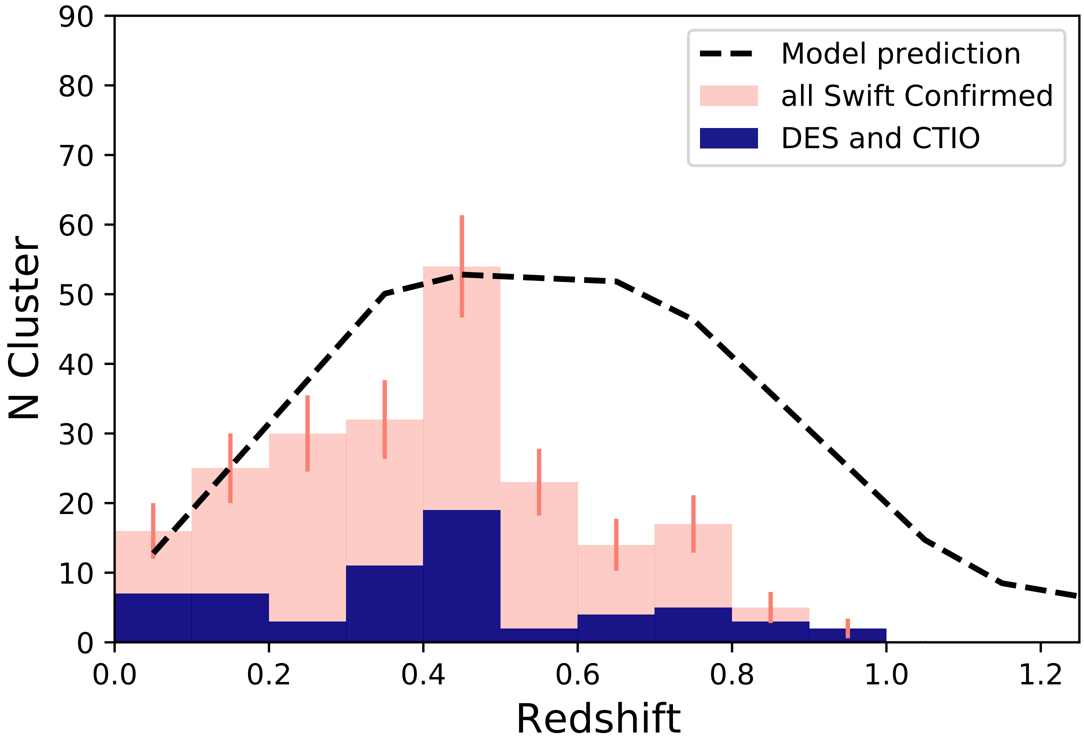

Figure 4.5 Observed redshift distribution (navy) of the confirmed SACS clusters using DES and CTIO/DECam photometric data as compared to the the theoretical prediction (black) derived from the cluster mass function model by Tinker et al. 2008. The redshift distribution of the 219 optically verified SACS clusters is shown in pink. The errors are calculated assuming a poisson distribution.

References

Aihara, H., Allende Prieto, C., An, D., et al. 2011, ApJS, 193, 29

Abell, G. O. 1958, ApJS, 3, 211

Abell, G. O., Corwin, H. G., Jr., & Olowin, R. P. 1989, ApJS, 70, 1

Adami C., Durret F., Benoist C. et al. 2010, A&A 509, 81 (A10)

Adami C., Altieri B., Valtchanov I., 2012, MNRAS, 423, 3561

Allen S. W., Schmidt R. W., Fabian A. C., 2002a, MNRAS, 334, L11

Allen, S. W., Evrard, A. E., & Mantz, A. B. 2011, ARA&A, 49, 409

Applegate D. E. et al., 2014, MNRAS, 439, 48

Arnaud, K. A. 1996, Astronomical Data Analysis Software and Systems V, 101, 17

Assef, R. J., Kochanek, C. S., Brodwin, M., et al. 2010, ApJ, 713, 970

Bahcall, N. A. 1988, ARA&A, 26, 631

Bahcall, N. A., Fan, X., & Cen, R. 1997, ApJ, 485, L53

Bahcall, J. N., & Sarazin, C. L. 1977, ApJ, 213, L99

Bahcall, N., & Soniera, R. M. 1983, ApJ, 270, 20

Balogh M. L., Navarro J. F., Morris S. L., 2000, ApJ, 540, 113

Banerjee, P., Szabo, T., Pierpaoli, E., et al. 2018, New A, 58, 61

Barkhouse W. A., Green P. J., Vikhlinin A., Kim D., Perley D.,Cameron R., Silverman J., Mossman A. et al., 2006, ApJ, 645, 955

Basilakos, S., Plionis, M., Georgakakis, A., et al. 2004, MNRAS, 351, 989

Bertin, E. & Arnouts, S. 1996, A&AS, 117, 393

Bertin, E., Mellier, Y., Radovich, M., et al. 2002, in Astronomical Society of the Pacific Conference Series, Vol. 281, Astronomical Data Analysis Software and Systems XI, ed. D. A. Bohlender, D. Durand, & T. H. Handley, 228

Böhringer, H., Voges, W., Huchra, J. P., et al. 2000, ApJS, 129, 435

Böhringer, H., Schuecker, P., Guzzo, L., et al. 2001, A&A, 369, 826

Borgani, S., Rosati, P., Tozzi, P., Stanford, S. A., Eisenhardt, P. E., Lidman, C., Holden, B., Della Ceca, R., Norman, C., & Squires, G. 2001

Blain, A. W., Jameson, A., Smail, I., Longair, M. S., Kneib,J.-P. & Ivison, R. J. 1999, MNRAS 309, 715 (B99b)

Brammer, G. B., van Dokkum, P. G., & Coppi, P. 2008, ApJ, 686, 1503

Brodwin, M., et al. 2010, ApJ, 721, 90

Butcher H., Oemler A.Jr., 1978, ApJ, 219, 18

Bell, E. F., McIntosh, D. H., Katz, N., & Weinberg, M. D. 2003, ApJS, 149, 289B

Bonamente, M., Joy, M., LaRoque, S. J., Carlstrom, J. E., Nagai, D., & Marrone, D. P. 2008, ApJ, 675, 106

Carlberg R. G., Yee H. K. C., Ellingson E., Abraham R., Gravel P., Morris S., Pritchet C. J., 1996, ApJ, 462, 32

Carbone C., Fedeli C., Moscardini L, Cimatti A. 2012, J. Cosmology Astropart. Phys., 3, 23

Nilo Castellón, J. L., Alonso, M. V., García Lambas, D., et al. 2014, MNRAS, 437, 2607

Cavaliere A., Fusco-Femiano R., 1976, A&A, 49, 137

Carlstrom, J. E., Holder, G. P., & Reese, E. D. 2002, ARA&A, 40, 643

Chambers, K. C., Magnier, E. A., Metcalfe, N., et al. 2016

Covey, K. R., et al. 2007, AJ, 134, 2398

Clerc N., Sadibekova T., Pierre M., Pacaud F., Le F‘evre J.-P.,

Dai, X., Assef, R. J., Kochanek, C. S., et al. 2009, ApJ, 697, 506

Dai, X., Griffin, R. D., Kochanek, C. S., Nugent, J. M., & Bregman, J. N. 2015, ApJS, 218, 8

Desai, S., Armstrong, R., Mohr, J. J., et al. 2012, ApJ, 757, 83

Dressler, A. and Gunn, J. E. 1992, ApJS, 78, 1.

Dressler A., 1980, ApJ, 236, 351

Ebeling H., Wiedenmann G., 1993, Phys. Rev. E, 47, 704

Ebeling H., Edge A. C., Bohringer H., Allen S. W., Crawford C. S., Fabian A. C., Voges W., Huchra J. P., 1998, MNRAS, 301, 881

Ebeling, H., & Wiedenmann, G. 1993, Phys. Rev. E, 47, 704

Ebeling, H., Edge, A. C., & Henry, J. P. 2001, ApJ, 553, 668

Einasto J., Einasto M., Gottlober S., Muller V., Saar V., Starobinsky A.A., Tago E., Tbcker D., Ander-nach H., & Frisch P., 1997, Nature, 385, 139

Ettori S., Gastaldello F., Leccardi A., Molendi S., Rossetti M., Buote D., Meneghetti M., 2010, A&A, 524, A68

Felten, J. E. 1996, Astronomical Society of the Pacific Conference Series, Vol. 88, Mitigating the Baryon Crisis in Clusters: Can Magnetic Pressure be Important?, ed. V. Trimble & A. Reisenegger, 271

Feng Y., Chu M.-Y., Seljak U., McDonald P., 2016, MNRAS, 463, 2273

Finlator, K., et al. 2000, AJ, 120, 2615 Hawley, S. L., et al. 2002, AJ, 123, 3409

Flewelling H., 2018, AAS, 231, 436.01

Foley, R. J., et al. 2011, ApJ, 731, 86

Garilli B., Bottini D., Maccagni D., Carrasco L., Recillas E., 1996, ApJS, 105, 191

Gladders M. D., Yee H. K. C., 2000, AJ, 120, 2148

Green P., et al., 2004, ApJS, 150, 43

Goto T., Yamauchi C., Fujita Y., Okamura S., Sekiguchi M., Smail I., Bernardi M., Gomez P. L., 2003, MNRAS, 346, 601

Goto T., Sekiguchi M., Nichol R. C., Bahcall N. A., Kim R. S. J., Annis J., Ivezic´ Z., Brinkmann, J. et al., 2002, AJ, 123, 1807

Garilli, B., Maccagni, D., & Andreon, S. 1999, A&A, 342, 408

Griffin, R. D., Dai, X., Kochanek, C. S., Bregman, J. N., 2016, ApJS, 222, 1

Gladders M. D., Yee H. K. C., 2000, AJ, 120, 2148 —, 2005, ApJS, 157, 1

Goto T., Sekiguchi M., Nichol R. C., Bahcall N. A., Kim R. S. J., Annis J., Ivezic´ Z., Brinkmann, J. et al., 2002, AJ, 123, 1807

Hao, J., McKay, T. A., Koester, B. P., et al. 2010, ApJS, 191, 254

Hoekstra, H. 2007, MNRAS, 379, 317

Hoekstra, H., Herbonnet, R., Muzzin, A., et al. 2015, MNRAS, 449, 685

Hasselfield, M., Hilton, M., Marriage, T. A., et al. 2013, Journal of Cosmology and Astro-Particle Physics, 2013, 008

Hansen, S. M., Sheldon, E. S., Wechsler, R. H., & Koester, B. P. 2009, ApJ, 699, 1333

Hincks, A. D., et al. 2010, ApJS, 191, 423

Huchra J. P. Geller M. J., 1982, ApJ, 257, 423

Gladders, M. D., & Yee, H. K. C. 2005, ApJS, 157, 1

Gladders M. D., Lopez-Cruz O., Yee H. K. C., Kodama T., 1998, ApJ, 501, 571

High, F. W., Stubbs, C. W., Rest, A., Stalder, B., & Challis, P. 2009, AJ, 138, 110

Ivezi´c, Z., et al. 2007, AJ, 134, 973

Juric, M., et al. 2008, ´ ApJ, 673, 864

Kelly P. L., et al., 2014, MNRAS, 439, 28

Kodama T., Tanaka I., Kajisawa M., Kurk J., Venemans B., DeBreuck C., Vernet J., Lidman C., 2007, MNRAS, 377, 1717

Kaiser, N., Aussel, H., Burke, B. E., et al. 2002, Proc. SPIE, 4836, 154

Kim Y.-R., Croft R. A., 2004, Astrophys. J., 607, 164

Koester, B. P., et al. 2007a, ApJ, 660, 239

Kravtsov, A. V. & Borgani, S. 2012, ARA&A, 50, 353

Lopes P. A. A., de Carvalho R. R., Gal R. R., Djorgovski S. G., Odewahn S. C., Mahabal A. A., Brunner R. J., 2004, AJ, 128, 1017

Okabe N., Zhang Y.-Y., Finoguenov A., Takada M., Smith G. P., Umetsu K., Futamase T.. , ApJ , 2010b, vol. 721 pg. 875

Okabe N., Bourdin H., Mazzotta P., Maurogordato S., 2011, ApJ, 741, 116

Okabe, N., & Smith, G. P. 2016, MNRAS, 461, 3794

Postman, M., Lubin, L. M., Gunn, J. E., Oke, J. B., Hoessel, J. G., Schneider, D. P., & Christensen, J. A. 1996, AJ, 111, 61

Lauer T. R. Postman M. Strauss M. A. Graves G. J. Chisari N. E. 2014 ApJ 797 82

Metcalfe, L., et al. 2003, A&A, 407, 791

Merloni A. et al., 2012, arXiv:1209.3114

Munshi D., Coles P., 2003, MNRAS, 338, 846

Mantz, A. B., Abdulla, Z., Carlstrom, J. E., et al. 2014, ApJ, 794, 157

Li I. H., Yee H. K. C., 2008, The Astronomical Journal, 135, 809

Mazure A., Adami C., Pierre M. et al. 2007, A&A 467, 49 (M07)

Mehrtens, N., Romer, A. K., Hilton, M., et al. 2012, MNRAS, 423, 1024

Mitchell, R. J., Ives, J. C., & Culhane, J. L. 1976, in BAAS, Vol. 8, Bulletin of the American Astronomical Society, 553

Marrone, D. P., et al. 2012, ApJ, 754, 119

Maughan B. J., Giles P. A., Randall S. W., Jones C., Forman W. R., 2012, MNRAS, 421, 1583

Menanteau, F., et al. 2012, ApJ, 748, 7

McInnes, R. N., Menanteau, F., Heavens, A. F., et al. 2009, MNRAS, 399, L84

Navarro, J. F., Frenk, C. S., & White, S. D. M. 1995, MNRAS, 275, 720

Nilo Castell´on, J. L., Alonso, M. V., Garc´ıa Lambas, D., et al. 2014, MNRAS, 437, 2607

Pacaud F., et al., 2006, MNRAS, 372, 578

Popesso, P., Bohringer, H., Romaniello, M., & Voges, W. 2005, ¨ A&A, 433, 431

Postman M, Geller M., & Huchra J. 1986, AJ, 91, 1267

Postman, M., Huchra, J. P., & Geller, M. J. 1992, ApJ, 384, 404

Postman, M., Lubin, L. M., Gunn, J. E., Oke, J. B., Hoessel, J. G., Schneider, D. P., & Christensen, J. A. 1996, AJ, 111, 615

Postman, M., Franx, M., Cross, N. J. G., et al. 2005, ApJ, 623, 721

Poggianti, B. M., Smail, I., Dressler, A., Couch, W. J., Barger, J., Butcher, H., Ellis, E. S., & Oemler, A., Jr., 1999, ApJ, 518, 576

Piffaretti, R., Arnaud, M., Pratt, G.W., et al. 2011, A&A, 534, A109

Pillepich, A., Porciani, C., & Reiprich, T. H. 2012, MNRAS, 422, 44

Pierre, M., Pacaud, F., Adami, C., et al. 2016, A&A, 592, A1

Predehl, P., Andritschke, R., B¨ohringer, H., et al. 2010, in Society of Photo-Optical Instrumentation Engineers (SPIE) Conference Series, Vol. 7732, Society of Photo-Optical Instrumentation Engineers (SPIE) Conference Series

Planck Collaboration. 2011b, A&A, 536, A26

Planck Collaboration et al. 2013, A&A, 550, A129 (PI3)

Ramella M., Boschin W., Fadda D., Nonino M., 2001, A&A, 368, 776

Ramella M., Boschin W., Fadda D., Nonino M., 2001, A&A, 368, 776

Reiprich, T. H. & B¨ohringer, H. 2002, ApJ, 567, 716

Rykoff, E. S., Rozo, E., Busha, M. T., et al. 2014, ApJ, 785, 104

Rykoff E. S., et al., 2016, ApJS , 224, 1

Reiprich, T. H. & Böhringer, H. 2002, ApJ, 567, 716

Stalder, B., et al. 2012, ApJ

Sunyaev, R., & Zeldovich, I. B. 1980, MNRAS, 190, 413

Szabo T., Pierpaoli E.,Dong2 F.,Pipino A., Gunn J.,2011, ApJ, 736,1

Smith G. P., Kneib J.-P., Smail I., Mazzotta P., Ebeling H., Czoske O.. , MNRAS , 2005, vol. 359 pg. 417

Smith, G. P., Treu, T., Ellis, R. S., Moran, S. M., & Dressler, A. 2005, ApJ, 620, 78

Sif´on, C., et al. 2012, ApJ

Takey A., Schwope A., Lamer G., 2011, A&A, 534, A120

Takey A., Schwope A., Lamer G., 2013, A&A, 558, A75

Takey A., Schwope A., Lamer G., 2014, A&A, 564, A54

Takey, A., Durret, F., Mahmoud, E., & Ali, G. B. 2016, A&A, 594, A32

Tinker, J., Kravtsov, A. V., Klypin, A., et al. 2008, ApJ, 688, 709

van Breukelen, C., & Clewley, L. 2009, Mon Not R Astron Soc, 395, 1845

Voit, G. M. 2005, RvMP, 77, 207

Von der Linden, A., Best, P. N., Kauffmann, G., & White, S. D. M. 2007, MNRAS, 379, 867

Vanderlinde, K., et al. 2010, ApJ, 722, 1180

Wen, Z. L., Han, J. L., & Liu, F. S. 2012, ApJS, 199, 34

Zwicky F., Herzog E., Wild P., 1961, Catalogue of galaxies and of clusters of galaxies, Vol. I, Pasadena: California Institute of Technology (CIT), —c1961

Zehavi, I., et al. 2005, ApJ, 630, 1

Chapter 5

Final remarks

"Something somewhere incredible is waiting to be known"

Taking inspiration from the powerful words of Carl Sagan, below I summarize the main conclusions of my thesis chapters and paint a picture for the future of the research projects discussed therein.

5.0.1 Quasar microlensing

Constraining the discrete lens population in extragalactic systems

Through exoplanetary explorations over the past few decades, it has been well established that planets are ubiquitious in our galaxy (e.g., Mayor & Queloz 1995; Winn & Fabrycky 2015). It is customary to assume that planetary species can be found in remote galaxies as well since other galaxies present similar conditions under which planets form, however, so far, we have no evidence to prove that planets exist beyond the Milky Way. With the existing observational resources, it is impossible to resolve a planet in the extragalactic domain owing to the large distances and the small area subtended by these galaxies in the sky. Nonetheless, we have identified a novel technique that uses quasar microlensing to probe the unbound sub-stellar population within distant extragalactic systems (Dai & Guerras 2018; Bhatiani et al. 2019). Quasar microlensing is induced by individual stars or lower mass compact objects in the lensing galaxy, and manifests in the time variable magnification of its macroimages. In a scenario when there is a planet in the massive galaxy, fluctuations are observed in the X-ray spectrum of the quasar images (Dai & Guerras 2018). In the Chapter 2, I described our application of this technique to extract planetary signatures in two lensed systems, Q J0158-4325 consisting of a lens galaxy ($z_l \sim 0.31$), and SDSS J1004+4112 consisting of a galaxy cluster lens ($z_l \sim 0.68$).

Decade long X-ray monitoring campaign using the Chandra X-ray telescope has revealed that several gravitationally lensed quasars exhibit emission line peak variations and double line features in the FeKα emission originating in the inner region of the accretion disk (e.g., Chartas et al. 2017). These observed variations of the emission line peak energy can be explained as microlensing of the FeKα emission region induced by planet-mass microlenses. To explain the observations, we computed microlensing simulations using the Inverse polygon mapping (IPM; Mediavilla et al. 2011) method and implemented an edge detection algorithm to determine the probability of a caustic transiting the source region. Comparison with the observed line shift rates, yielded constraints on the sub-stellar population, with masses ranging from Lunar ($10^{-8}M_\odot$) to Jovian ($10^{-3}M_\odot$) mass bodies, within these galaxy or cluster scale structures, which seems to be consistent with the current constraints for the free-floating planets in the Milky Way (Mróz et al. 2017). These results suggest that unbound planet-mass objects are common in galaxies, and the leading candidates are free-floating planets and primordial black holes. Without the dissecting the demographics, our constraints fall two orders of magnitude below the MACHO upper limit, thus yielding the most stringent constraints for primordial black holes at the mass range. This study has produced the first-ever constraints on the sub-stellar mass distribution in the intracluster light (ICL) of a galaxy cluster.

5.0.2 Future prospects

The measurements of the unbound planet mass fraction that constitutes the main results of Chapter 2 are subject to systematic uncertainties; therefore, newer and deeper observations with Chandra/XMM-newton and improved modeling are warranted to further tighten the constraints. Future work involves doubling the sample size with the inclusion of two other lensed quasars using Chandra archival data to establish the validity of our method and compare the sub-stellar mass density of the lens galaxies. The prospective research includes: i) measuring the frequency of line shifts in two new lensed systems, Q2237+0305 and HE0435−1223, which have not been previously reported in literature ii) confirming the frequency of line energy shift for QJ0158−4325 and SDSS1004+4112 reported in Chartas et al. (2017) iii) performing microlensing analysis to constrain the population of unbound sub-Jupiter objects in all four lens galaxies.

One of the most important results of the aforementioned work indicates that major contribution to the microlensing signal comes from planet mass objects. Using contemporaneous observations by the SMARTS-1.3m for one of the most well-studied microlensed quasars, RXJ1131−1231, preliminary studies of the optical light curves for the quasar images indicate that some X-ray microlensing/line shift events exhibit no optical microlensing peaks, which are predominantly sensitive to stellar microlenses owing to the relatively larger emission size. Although premature, this suggests that stellar contribution in the microlensing of the FeKα emission region is not significant and is mostly dominated by unbound planetary microlenses. A future project could involve simulating light curves for X-ray and optical source regions to substantiate these observations. With additional monitoring data available in the near future, an even clearer picture will be established. Furthermore, I also plan to use an analytical approach to test a major assumption in our work that hinges upon the fact that a line shift occurs as a consequence of a caustic crossing event. This would demand modeling a microlensing caustic within the source region to simulate a caustic crossing event and determine the probability of line shifts for planet and star mass microlenses. In addition, it would be interesting to investigate the effects of accretion disk models, various lens model parameters, and spatial resolution on the line shift rate.

5.0.3 LSST era: cosmology, ISM studies, and more

With the advent of the Large synoptic survey telescope (LSST) and Euclid survey, we can expect to discover thousands of quadruply lensed quasars including rare large separation lenses (image separation > 10"). Time delay measurements of these quads can be used to constrain cosmology including the Hubble parameter. These lensed quasars can be followed-up with sensitive X-ray observations so as to resolve the spatial structure of the quasar accretion disk, measure the spin of blackholes at high redshifts, and determine the stellar M/L ratio. Moreover, these X-ray observations can allow us to constrain the granular distribution within the lensing galaxy which can be studied as a function of redshift, and statistically map the sub-stellar population within the galaxy. Furthermore, the discovery of quasar-galaxy strong lens systems will allow us to probe the ISM of the intermediate redshift galaxies (e.g., Prochaska & Herbert-Fort 2004; Dai et al. 2006). The lensed quasar spectrum, in certain cases, can carry signatures of the cold ISM in the form of reddening due to dust, absorption features in the X-ray spectrum, and absorption lines in the optical/UV spectrum. Studies of these lensed systems can allow us to explore the ISM of high density regions within the lens galaxies and help us identify ghostly damped Lyman alpha systems (Dai et al. 2020).

Swift AGN and Cluster survey (SACS)

5.0.4 Optical confirmation of X-ray selected clusters

The Swift AGN and cluster survey (SACS; Dai et al. 2015) is a serendipitous X-ray survey aimed at building a large uniformly selected X-ray cluster catalog with 442 cluster candidates in it's first release. Initial follow-up study has confirmed 50% percent of clusters in the SDSS footprint as $z < 0.5$ clusters (Griffin et al. 2016). In Chapter 3, I have described the optical follow-up analysis of 247 (out of 442) X-ray selected cluster candidates from the Swift cluster catalog using multi-band imaging from MDM-2.4m and the Pan-STARRS survey for the sky north of -30 degrees. Here we utilized the Cluster Red Sequence (CRS) method to locate galaxy overdensities in the three-dimensional color space to confirm these cluster candidates and also estimate their photometric redshifts. This involved implementing a red sequence algorithm of simultaneous fitting of the source and background color distribution of galaxies around the cluster X-ray centroid. Our analysis provides optical confirmation of 55 clusters with significant galaxy over-densities with photometric redshift estimates extending up to $z \sim 0.8$ (See Fig.

3.5). The remaining unidentified cluster candidates are deemed as high redshift clusters with $z > 0.8$ and serve as excellent targets for Near Infrared (NIR) and spectroscopic observations. In Chapter 4, the cluster identification method, developed in Chapter 3, is extended to the southern sky using the data from the Dark energy survey and our dedicated observations with CTIO-4m/DECam. The analysis has confirmed $> 3\sigma$ overdensities for 64 SACS X-ray cluster candidates. In addition, the scaling relations between the cluster mass proxies, the bolometric X-ray luminosity and optical richness, are determined, and found to be in agreement with other studies in the literature. The distribution of the offsets between the X-ray and optical centers for all the optically confirmed SACS clusters showed consistency with previous studies and the median offset for the SACS sample is found to be ~ 180 kpc.

5.0.5 Future scope : Multiwavelength studies of Galaxy clusters

The results from Chapter 4 show that we are able to detect and measure the photometric redshifts of 51% of the X-ray cluster candidates (See Fig. 4.5) from SACS I. The remaining 49% of the cluster candidates could possibly be high redshift clusters, where the 4000 Å break, that appears as the red sequence, transcends the visible wavebands and moves into the IR. Upon comparison with the theoretical redshift distribution based on the flux limit and area of the Swift AGN and cluster survey, we predict that 30% of the cluster candidates in our sample to fall in the $z > 0.8$ range. Nearly 19% of these non-detections could be attributed to the sub-optimal imaging conditions in certain cases or could be false positives from the X-ray survey. Since the survey is nearly complete for redshifts $z \leq 0.5$, we expect the false positive rate to be low. Therefore deeper observations maybe needed to cover the intermediate redshift range. I have completed NIR imaging for most of the undetected clusters in the SACS sample that lie in the northern hemisphere using APO-3.5m/NICFPS. Future work involves applying my cluster detection method to these potential high-z candidates using NIR photometry.

The next release of the Swift AGN and cluster survey is expected to yield the largest uniformly selected X-ray cluster catalog with ~ 1000 cluster candidates (Mishra et al. 2022, in prep). A successful optical/NIR follow-up analysis of the cluster catalog will provide a uniformly selected high-z cluster sample, thus allowing a systematic study of the evolution of galaxy clusters. We have proposed NIR imaging of the high-z cluster candidates in the Southern sky with SOAR-4m/Spartan. An extensive and complete sample of SACS clusters will enable us to study the evolution of cluster luminosity functions, constrain the cluster mass function, and measure the scaling relations for galaxy clusters. For example, studying the L_X-T relationship as a function of redshift serves as an important test for the self-similar model and the presence of any additional baryonic processes. Existing studies show incompatible predictions for the manner of evolution of clusters (See Mantz et al. 2010), particularly due to the limited sample of medium to high-z X-ray clusters.

Moreover, as opposed to rich clusters, low-z lower mass clusters incur significant loss of baryons (e.g., Dai et al. 2010), possibly prompted by preheating and feedback processes. Measurement of baryon loss for high-z poor clusters will help determine when these processes occurred and allow us to constrain the underlying mechanism that drives the baryonic loss. Owing to the high flux limit, SACS contains more lower mass clusters that are suitable for deep follow-up studies. A multiwavelength study of the Swift clusters in X-rays, S-Z, optical and NIR will allow us to investigate the evolution of various cluster properties down to the galaxy group regime, and test whether clusters and groups evolve self-similarly with redshift, where $z > 0.8$ sample will have the most constraining effect. With several hundred thousand clusters expected to be discovered by eROSITA, combined with the SACS clusters, will provide a large sample of X-ray selected clusters, which when cross-correlated with LSST, Euclid, and WFIRST, can allow us to calibrate the observable-mass relations, constrain cosmological parameters, and also measure the BCG offset distribution and miscentering fraction, which can be utilized for the weak lensing studies. Furthermore, observing time with the Chandra X-ray telescope can be proposed for mass measurements of SACS clusters with insufficient X-ray counts in prior Swift observations. A large sample of cluster masses allows for accurate determination of the cluster mass function, which is crucial for testing the existing cosmological models. The Swift sample is expected to reduce the uncertainties in the measurement of the cluster mass function by a factor of 2.5 and promises stronger constraints on cosmology.

References

Bhatiani, S., Dai, X., & Guerras, E. 2019, Astrophys. J., 885, 77

Chartas, G., Krawczynski, H., Zalesky, L., et al. 2017, ApJ, 837, 26

Dai, X., & Kochanek, C. S. 2005, ApJ, 625, 633

Dai, X., Bregman, J. N., Kochanek, C. S., Rasia, E. 2010, ApJ, 719, 119

Dai, X., Griffin, R. D., Kochanek, C. S., Nugent, J. M., & Bregman, J. N. 2015, ApJS, 218, 8

Dai, X. & Guerras, E. 2018, ApJ, 853, L27

Dai X., Bhatiani S., Chen B., 2020, MNRAS, 495, 460

Griffin, R. D., Dai, X., Kochanek, C. S., Bregman, J. N., 2016, ApJS, 222, 1

Mayor, M., & Queloz, D. 1995, Nature, 378, 355

Mantz et al. 2010, MNRAS, 406, 1173

Mroz, P., Udalski, A., Skowron, J., et al. 2017, Nature, 548, 183

Mediavilla, E., Mediavilla, T., Munoz, J. A., et al. 2011, ApJ, 741, 42

Prochaska, J. X., & Herbert-Fort, S. 2004, PASP, 116, 622

Winn, J. N., & Fabrycky, D. C. 2015, ARA&A, 53, 409